JET–R(00)03

Many Authors

Descriptive Analysis of the 1999 Task Force C Data

JET–R(00)03

Descriptive Analysis of the 1999 Task Force C Data

Many Authors.

EURATOM/UKAEA Fusion Association, Culham Science Centre,
Abingdon, Oxfordshire, OX14 3EA, UK.

July 2000

PREFACE

As part of the winding-up of the JET Joint Undertaking, an agreement was established with UKAEA to validate the 1999 Gas Box data and make a descriptive analysis of the data. This report constitutes one of the deliverables specified under the agreement and describes the descriptive data analysis work undertaken examining results from the Task Force B and C campaigns in 1999. Two main areas are covered in this report - studies of plasma shaping effects for ITER and studies of various issues for Optimised Shear plasmas. The ITER shaping studies concentrated on the effects on energy confinement but also included a study of shaping effects on neo-classical tearing mode stability. The Optimised Shear studies covered a wide range of issues, including:- diagnostic studies of MSE, and ion temperature measurements in the presence of argon; studies of triggering mechanisms for Internal Transport Barriers (ITBs), the threshold power to make ITBs and the effect of LHCD modifications to the q-profile on this threshold; and studies of high β_n and high β_p Optimised Shear plasmas.

CONTENTS

1. ITER SHAPE AND ELONGATION STUDIES

D. C. McDonald[1], P.J Lomas[1], J G. Cordey[1]

JET Joint Undertaking, Abingdon, Oxon, OX14 3EA, UK.
[1] EUARTOM/UKAEA Fusion Association, Culham Science Centre, Culham, Abingdon, Oxon. OX14 3EA

1.1 Overview

The studies were carried out, at the request of the ITER team, to determine the separate effects of shaping and elongation on confinement in conditions as close to those of the next step ITER-FEAT device as possible. 3 configurations were produced: at low elongation ($\kappa \approx 1.55$) and low triangularity ($\delta \approx 0.2$), LL; at high elongation ($\kappa \approx 1.85$) and low triangularity ($\delta \approx 0.2$), HL; and at high elongation ($\kappa \approx 1.9$) and high triangularity ($\delta \approx 0.35$), HH; all at constant minor radius ($a_{\min} \approx 84cm$). In each configuration, a $I_p \approx 1.8MA/q_{95} \approx 3.3$ scenario was developed and a gas scan of NBI heated ELMy H-modes was made. Two further scenarios were also developed, in the HH configuration, to study the independent effects of current and field scalings, as well as another scenario in the LL configuration to study the effect of current and constant field.

The effect of elongation was seen clearly, in agreement with the scaling law ($\kappa^{0.8\pm0.3}$) and in keeping with the wider JET database. The effect of triangularity did not show up outside the error bars ($\delta^{0.0\pm0.1}$), although there were signs that densities closer to Greenwald could be reached at higher triangularity. In all scenarios, increased density resulted in a fall in confinement and, in particular, the maintenance of good confinement at densities close to Greenwald for high triangularity [1.1] was not seen. Current and field scalings were in line with the scaling laws. A fall in confinement with NTM activity was also observed on some pulses.

1.2 Results

The IPB98(y,2) scaling law [1.2], based on results from 10 ITER similar machines, expresses the confinement time of a tokamak in terms of eight engineering parameters,

$$\tau_{conf} = 0.0562 \times P^{-0.69} B^{0.15} I^{0.93} \kappa_a{}^{0.78} n^{0.41} a^{0.58} R^{1.39} M^{0.19} \tag{1.1}$$

where τ_{conf} is in seconds, P is in MW, B is in Tesla, I is in MA, n is in $10^{19}\ m^{-3}$, a and R are in m and M is in the mean atomic mass. $\kappa_a = \Delta / \pi a^2$, where Δ is the poloidal cross-section, is the preferred elongation measure. Triangularity is not included. To study the effects of shaping, elongation and confinement loss at large density, we normalise the confinement times of the pulses in the experiment as,

$$\tau_{conf}^{norm} = \tau_{conf} \left(\frac{P_{NBI}}{15MW} \right)^{0.69} \left(\frac{B}{2.1T} \right)^{-0.15} \left(\frac{I}{1.8MA} \right)^{-0.93-0.41} \left(\frac{R}{3m} \right)^{-1.39}, \tag{1.2}$$

where $a = 84cm$ and $M = 2$ are constants across all scans and the extra power in the current term compensates for the change in Greenwald limit between the scenarios.

The confinement time, plotted against density, and the normalised confinement time of equation 1.2, plotted against density, are shown in Fig.1.1. One notices immediately the outlying HH 1.8 MA / 2.1 T point at low density with poor confinement. This is due to a strong NTM, causing a confinement drop of 22%, and is ignored in the following analysis. In the second graph we notice a reduction in spread in a given scan, as result of the power scaling, and the coming together of the two LL scans, as a result of the current scaling. This reflects good agreement with IPB98(y,2) in terms of current and power.

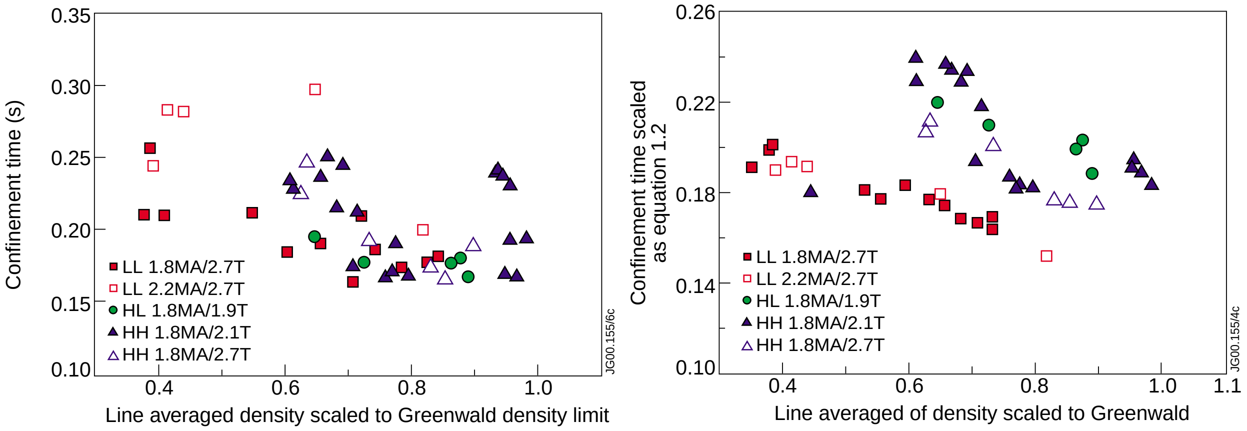

Fig.1.1: Effect on confinement of shaping, elongation and density

Comparing LL with HL, in the normalised plot, we see a marked improvement in confinement consistent with the 18% increase in elongation. Comparing HL with HH, we see little sign of confinement improvement, suggesting the effect of triangularity is small. A straight fit gives

$$\tau_{conf} \propto \kappa_a^{0.8\pm0.3}\delta^{0.0\pm0.1} \qquad (1.3)$$

in accordance with the larger JET database. These dependencies are consistent with those seen in the edge pedestal measurements [1.3], where the HL have a marked improvement in the edge pressure limit over the LL, suggesting an increase in the ballooning stability limit.

In all scenarios, we notice a fall in confinement as we increase the density towards the Greenwald limit. This is believed to be due to pedestal degradation and is seen more strongly in fig.1.2, where the full scaling law is shown, with its positive density scaling.

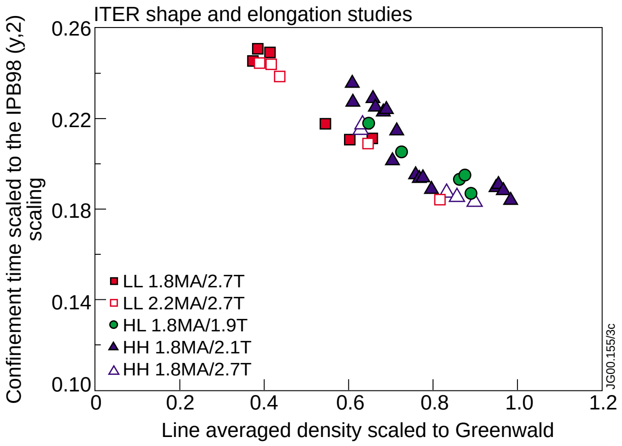

Fig.1.2: Comparison of data with the full IPB98(y,2) scaling law

Although confinement holds up to $n/n_{GW} = 0.65$ in the high triangularity HH discharges, the fall off at higher densities is strong. On this evidence, it would not be advisable to trust the scaling laws at higher densities. However, we note here that earlier experiments on JET [1.1], with the Mk IIA divertor, and on ASDEX Upgrade [1.5] have suggested a marked improvement in confinement with triangularity, so it would be wrong to conclude that triangularity had no effect solely on the basis of these results.

It has been suggested [1.1] that the fall in confinement with increasing density can be modelled by a two term scaling law, with terms reflecting the core and pedestal confinement. The core is taken as gyro-bohm ,with positive density scaling, and the pedestal scaling is based on fitting to the pedestal measurements. Taking the pedestal elongation dependence calculated from edge LIDAR measurements [1.3], together with the scaling for current, mass and temperature based on a fit to a wider JET database [1.1], we arrive at the two term scaling law.

$$\tau_{conf} = 0.0148\frac{I^{0.8}n^{0.6}R^{2.2}}{P^{0.6}M^{0.2}} + 0.29\frac{I^{2}R\kappa^{2}M}{nP}\,. \qquad (1.4)$$

The reciprocal dependency of the pedestal term on density reflects the degradation of the pedestal at higher densities. The elongation dependency appears only in the pedestal confinement.

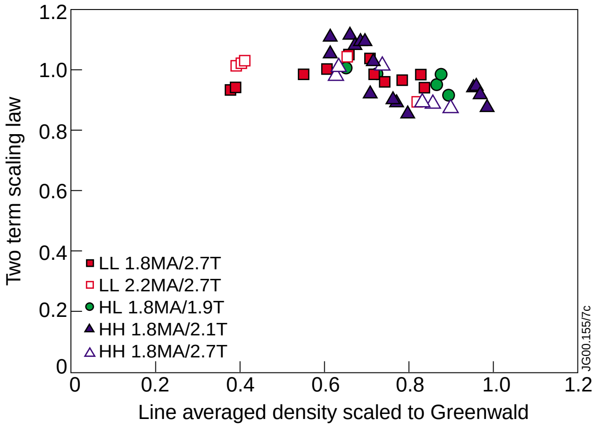

Fig.1.3: Comparison of data normalised by the two term scaling law of equation 1.4

We see in Fig.1.3 that equation [1.4] gives a good fit at high density and the effects of elongation and triangularity are well described. It should be stressed that equation 1.4 is based only on a fit to a relatively small database of JET pulses (209), for which pedestal and core data is available, but it does illustrate how a separate treatment of core and pedestal scaling results in a greatly improved description of experiment, particularly regarding the density dependence. At present a larger multi-machine pedestal database is being developed which should produce accurate two term scaling law.

ELM behaviour was also seen to vary between the discharges, with type I ELMs at lower densities and type III at higher. This seemed to be in accordance with taking the threshold as

$$P_{I-III} = 0.25n^{0.75}BR^{2}, \qquad (1.5)$$

[1.4]. A significant fall in confinement in the HH 1.8 MA / 2.1 T scenario at $n/n_{GW} = 0.7$ was accompanied by a sudden threefold increase in Type I ELM frequency.

1.3 Summary and future directions

With regard to the strong elongation dependence and the ignoring of triangularity, the experiment confirms the current scaling law IPB98(y,2). However, the holding up of confinement, at densities close to Greenwald, with increased triangularity was not observed. Several reasons for this have been suggested, including the nature of the gas fuelling in the divertor and the relative effect of varying upper and lower triangularity, both of which will be investigated on JET in 2000. The observation of a loss of confinement at high densities was shown to be in accordance with a two term scaling law. The importance of avoiding NTM modes was illustrated by a dramatic loss of confinement in pulses where they occurred.

One outstanding issue is the high current, elongation and field scenario (HH at 2.5 MA / 2.7 T), for which there was a beam failure resulting in only 3 pulses being available at significantly different powers. As comparison of this scenario with the HL scenario would demonstrate whether increased shaping gives the combined confinement increases from elongation scaling and increased volume together, further exploration would provide important information on ITER scaling.

1.4 Shot List

Pulse numbers	Type	κ	δ	I_{pla} [MA]	B [T]	q_{95}
49164, 49165, 49166, 49167, 49168, 49169, 49170, 49172, 49173, 49581, 49582, 49583	LL	1.55	0.2	1.8	2.7	3.2
49180, 49181, 49182, 49185, 49186	**LL**	**1.55**	**0.2**	**2.2**	**2.7**	**2.7**
49146, 49147, 49149, 49151, 49573	HL	1.8	0.2	1.8	1.9	3.3
49126, 49128, 49129, 49130, 49131, 49133, 49134, 49136, 49137, 49138, 49139, 49160, 49161, 49591, 49592, 49596	**HH**	**1.9**	**0.35**	**1.8**	**2.1**	**3.3**
49152, 49153, 49154, 49156, 49157, 49159	HH	1.9	0.35	1.8	2.7	4.5
49140, 49144, 49145	**HH**	**1.9**	**0.35**	**2.5**	**2.7**	**3.3**

Acknowledgements

The authors wish to thank all those who were involved in the experiment itself and in the validation of data for this report, particularly M. Charlet and C. Giroud.

References

[1.1] G. Saibene; Nuclear Fusion **39** (1999) 1133

[1.2] O. Kardaun; Plasma Phys. Control. Fusion **41** (1999) 429

[1.3] M. Beurskens; Abstract accepted for EPS 2000

[1.4] R. Sartori; Task Force AP report 2000

[1.5] J. Stober; Proceedings of 26th EPS conference on Contr. Fus. and Plasma Physics, Maastricht, ECA Vol.23J (1999) 1401

2. NTMS AND SAWTEETH IN ITER SHAPING STUDIES

R.J Buttery[1], T.C Hender[1], D. Howell[1].

JET Joint Undertaking, Abingdon, Oxon, OX14 3EA, UK
[1] EURATOM/UKAEA Fusion Association, Culham Science Centre, Abingdon, Oxon, OX14 3DB, UK.

2.1 Overview

Neoclassical tearing modes (NTMs) are a crucial issue for tokamak performance in baseline regimes for next step devices, such as the ELMy H-mode, limiting attainable normalised plasma pressure (β). Present databases are largely based on plasmas with intermediate levels of shaping (triangularity ~0.3, elongation ~1.7). However the optimisation of the tokamak concept for future devices, such as ITER-FEAT [2.1], has pushed to higher elongations and triangularity (triangularity ~0.5, elongation~1.85) in order to improve performance. So, it is important to understand how this impacts on NTM thresholds, from the perspective of refining estimates for the threshold and attainable normalised β's (β_N), but also as a way of testing/examining the many physical mechanisms that go into models used to extrapolate to next step devices. Also increased shaping may change the sawtooth features, such as inversion radius, and it is important to quantify this. Accordingly a series of shape scan experiments were performed on JET in 1999.

For sawteeth these shape scans show that as the shaping increases the sawtooth period, the relative amplitude of the sawtooth crash and the inversion radius, all decrease. These shaping experiments also show there is no significant difference in NTM β_N–thresholds between high and low shaping pulses. However, when parameters more closely associated with the physics mechanisms underlying NTM behaviour are examined, a clear difference is observed, with thresholds higher for high shaping configurations.

Much of the effect of a lower NTM threshold, at lower shaping, can be explained in terms of the seeding of the NTM, with sawteeth events larger at lower shaping, and differential rotation (between q=1 and q=1.5) lower (which implies weaker dynamic shielding) - both of which contribute to the observed lower NTM threshold. Geometric coupling factors are thought to be less significant, with little variation in the ratio of sizes of the q=1 to q=1.5 surfaces. The role of the seed is confirmed by the strong correlation between sawteeth and NTM onset.

2.2 Results

Dependence on shape of threshold for destabilising NTMs

Three categories of pulse were considered in these ITER shaping studies of: those with high elongation and high triangularity ('HH', δ~0.35 κ~1.9), high elongation and low triangularity ('HL', δ~0.19 κ~1.83) and low elongation and low triangularity ('LL', δ~0.22 κ~1.55).

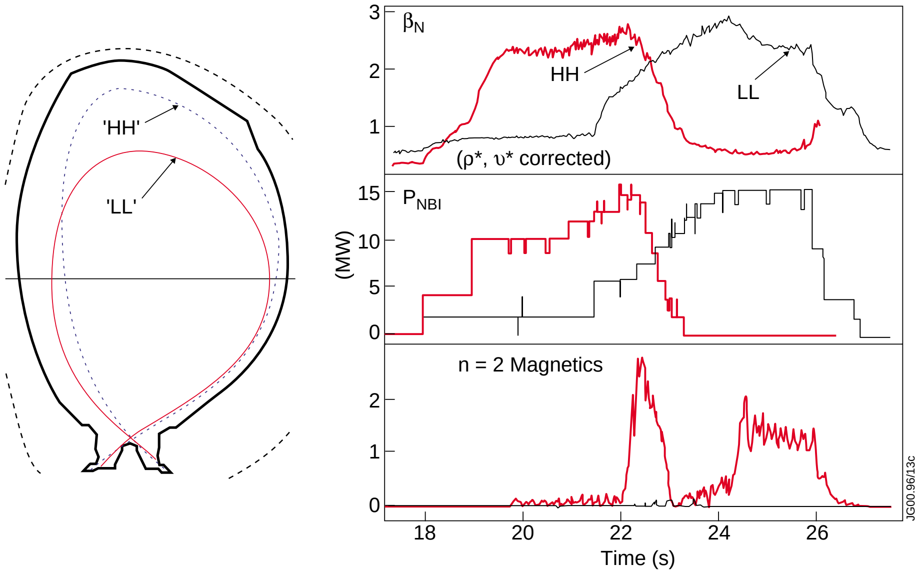

Fig.2.1: NTM onset dependence on β_N for an HH and LL pulse. Note the small change in β_N-threshold despite the large change in shape.

A study of the onset of m=3, n=2 NTMs shows that the value of β_N at which the NTM is triggered has little dependence on the plasma shape in this range, as shown in Fig.2.1, which is typical, and borne out by wider comparisons of shape scan pulses with standard shape fits (Fig.2.2).

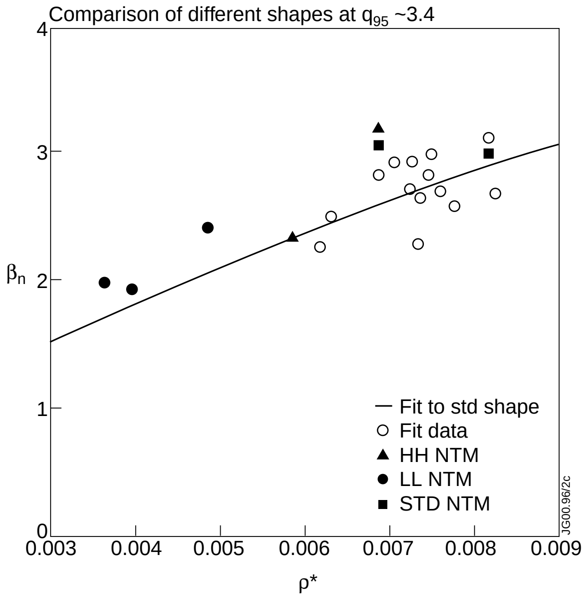

Fig.2.2: Variation of threshold for m=3, n=2 NTM with ρ (defined with respect to toroidal field). All data is corrected to $\nu_i/\varepsilon\omega^*=0.058$ using the scaling $\beta n\alpha(\nu_i/\varepsilon\omega^*)^{-0.081}$. Within the scatter there is no variation in threshold for the different shapes.*

This is useful information in terms of effects on operational limits in global parameters. However β_N does not accurately relate to the physics of NTM destabilisation, which depends on local parameters and profiles at the q=1.5 surface. Indeed, fits to standard shape data based on global parameters give rise to large, and sometimes systematic, discrepancies between pulses (Fig.2.3a). Understanding which local parameters to use depends on the detailed physics of the NTM onset. The threshold for NTM growth is governed by modified Rutherford equation for the growth rate of an island of size, w:

$$\frac{\tau_r}{r^2}\frac{dw}{dt} = \Delta' + \varepsilon^{1/2}\left(L_q / L_p\right)\frac{\beta_P}{w}\left(\frac{1}{1+w_d^2/w^2} - \frac{w_{pol}^2}{w^2}\right) \qquad (1)$$

This is expressed in terms of the tearing stability parameter (Δ'), bootstrap current (β_N/w term which represent the effect of flattening of bootstrap within the island region), ion polarisation effect (w_{pol} term) and additional transport effects in the island (w_d term, which is small for present devices). L_q and L_p are the scale lengths for safety factor and pressure gradients, ε measures the radius of the resonant surface normalised to major radius and τ_r is the resistive time scale. These last two effects act to oppose the drive for the mode at small island sizes (from the bootstrap effect), leading to the requirement of a seed perturbation. Neglecting w_d, the onset requires $w=Aw_{pol}$ with A>1 and w_{pol} given by,

$$w_{pol} \approx [g(\nu,\varepsilon)\ (Lq/Lp)\ \varepsilon]^{0.5}\ \rho_{\theta i}$$

where g is a function dependent on collisionality, ν. The seed must originate from other forms of MHD, most commonly sawteeth, and so depends on further physical mechanisms governing size of that MHD, coupling to the NTM resonant surface and shielding effects. The seed size will also affect the NTM threshold in β_N (although a ‘large’ seed will always lead to an NTM above a given critical β_N, while if seeds are too small NTM onset will be impossible). The marginal onset criterion for NTMs arising from Eq (1) is:

$$(L_q / L_p)^{0.5}\beta_p = r_s \Delta'\, \rho_\theta^* \frac{A}{(1-A^2)} g(\nu,\varepsilon) \tag{2}$$

Thus it can be seen that the appropriate local variables to use are $(L_q/L_p)^{0.5}\beta_N$ and ρ_θ*. When the NTM onset is parameterised in terms of these local variables, with profile parameters correctly incorporated, correlation and scatter are substantially improved (Fig.2.3b).

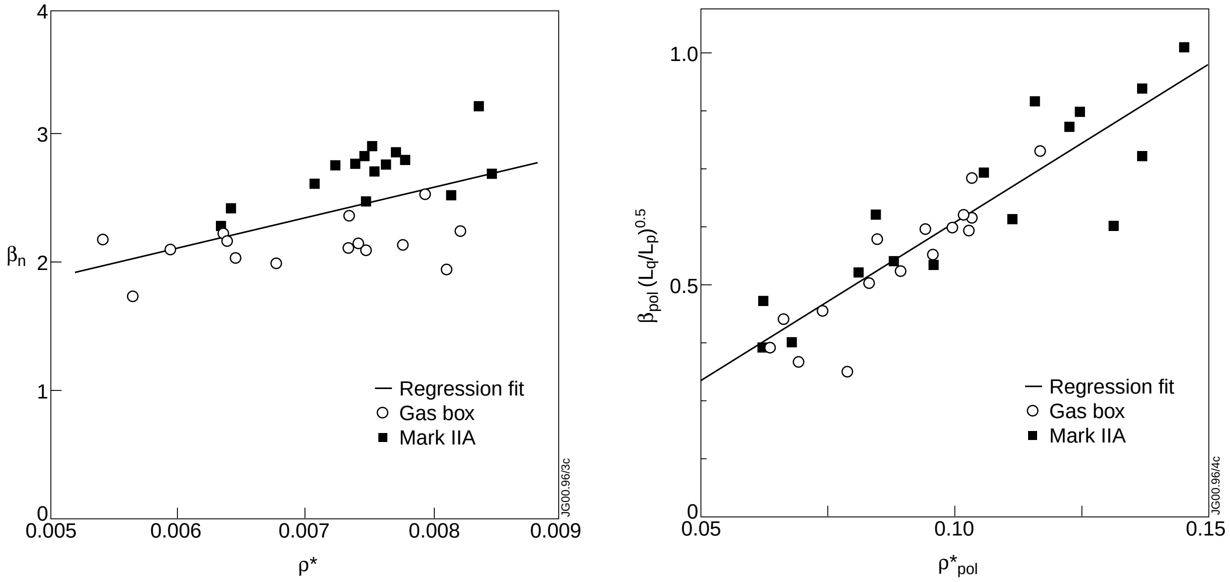

Fig.2.3(a) β_N threshold for standard shape pulses versus ρ (defined with respect to toroidal field) (b) Same data fitted using local variables. Note the systematic offset between the MKIIA and Gas Box data is removed when local parameters are used.*

Using local parameters to examine thresholds for the shape scan pulses, a clear offset between the HH and LL pulses is observed (see Fig.2.4), with the LL pulses having a lower threshold than the HH pulses. The average discrepancy between the two shape configurations is 33%, compared to a scatter in standard shape data of 12% about the fit. This indicates that either the drive and/or the seeding terms are stronger for LL plasmas.

We investigate how this result arises from the underlying physics, commencing with brief discussion of pedestal variation, then examining sawtooth behaviour, before going on to draw out effects on NTM thresholds and variation in other terms in the evolution equation.

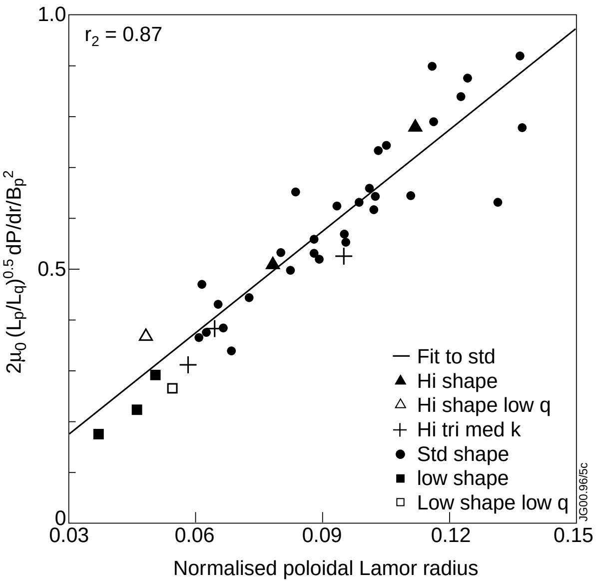

Fig.2.4: NTM onset dependence on local variables. Note the systematic difference between the high shape points (HH) and low shape points (LL)

Pedestal variations with shape

The height of the pedestal of these ELMy H-mode plasmas varies somewhat with plasma shape. This is shown in Fig.2.5, where we see the product 'n_eT_e' is larger for HH plasmas. This will lead to larger thermal energies across the plasma, and thus raise NTM thresholds in terms of β_N. In terms of local parameters, thresholds are quoted in terms of (pressure/$L_p^{0.5}$), where the square root comes from including profile effects in the ion polarisation term. Therefore we expect the improved pedestal in higher shaping to raise thresholds slightly (~$P^{0.5}$), due to the fact that the NTMs are driven by the local pressure gradient.

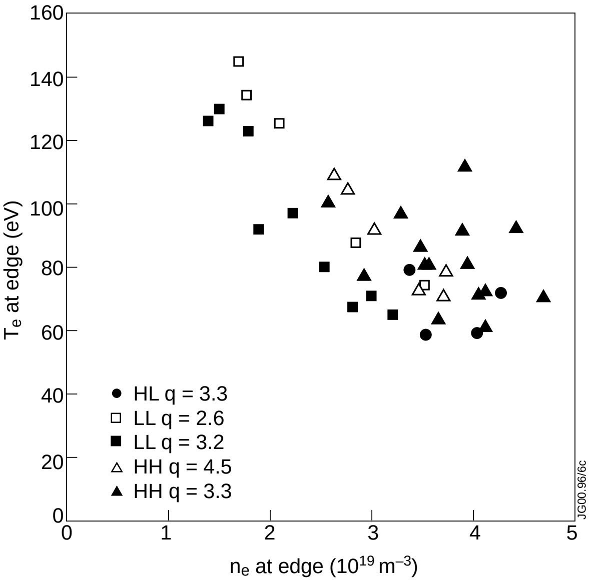

Fig.2.5: Variation of Te and ne at the pedestal

The effect of plasma shape on sawteeth

Figure 2.6 shows sawtooth period plotted against β_N. A clear dependence on shape is seen for a given q_{95}, and a dependence on q_{95} for a given shape. For q_{95}=3.3 the LL pulses have a much higher sawtooth period than the HH and HL pulses at a given β_N, which are very similar. We can conclude that elongation has a stronger effect than triangularity over the range studied. For a given shape we can also see that pulses with a higher value of q_{95} have a higher sawtooth period at a given β_N. This effect is most pronounced for the HH pulses, but is also observed to a lesser extent for the LL pulses. The correlation of sawtooth period with density is less clear, where sawtooth periods decrease as the density rises, but there is very little clear shape or q_{95} dependence.

Figure 2.7 shows the sawtooth inversion radius, normalised to the plasma minor radius, plotted against β_N. We can see a differentiation between the LL and HH pulses at higher β_n, with the LL pulses having roughly a 25% larger inversion radius for a given β_n. We also see that the inversion radius increases slowly with β_N. There is little differentiation of different q_{95} pulses.

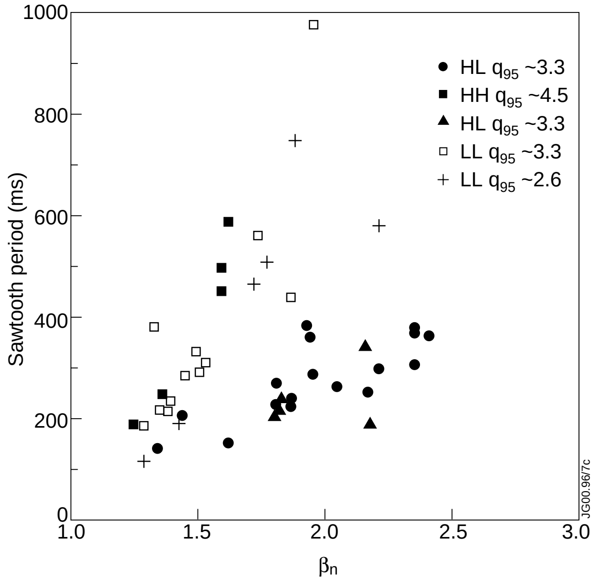

Fig.2.6: Sawtooth period plotted against β_n.

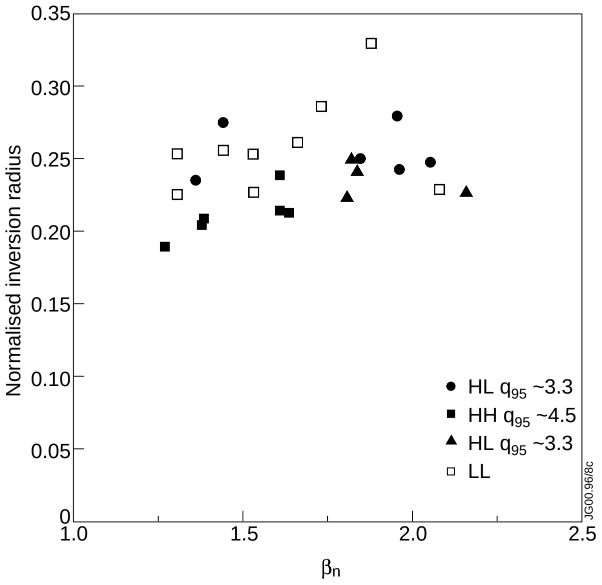

Fig. 2.7: Sawtooth inversion radius plotted against β_n.

Figure 2.8 shows the percentage drop in the soft x-ray signal at a sawtooth crash plotted against β_n, this gives an indication of the magnitude of the sawtooth. We see a marked difference between the LL pulses and the HH and HL pulses, with the LL pulses having much larger sawtooth crashes than the HH and HL pulses, which are very similar to each other. There does not seem to be a dependence on q_{95}. We can see an increase in sawtooth magnitude as β_N is increased, with the effect being much more pronounced for the LL pulses than the HH and HL pulses. This trend is also confirmed from the magnetics data, although it is much less clear in this case.

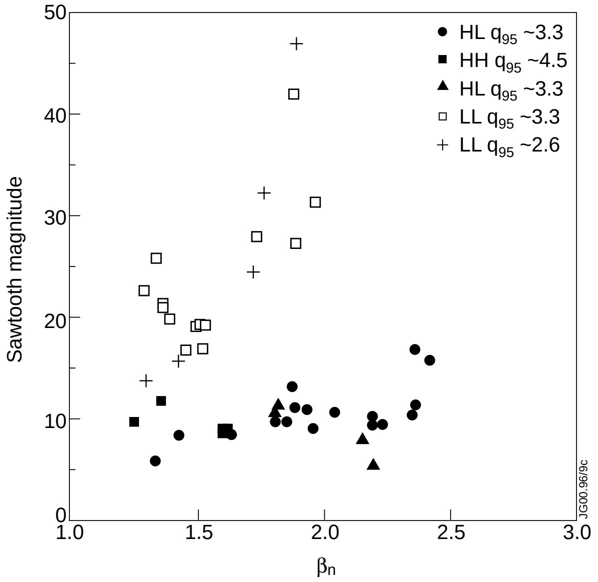

Fig.2.8: Sawtooth magnitude plotted against β_n.

In summary, more highly shaped plasmas have shorter sawtooth periods, resulting in smaller crashes (in terms of MHD or SXR emission). Higher β_N results in longer periods and larger events, as might be expected. The dominant shape effect seems to be through elongation, with HH and HL pulses behaving similarly. This might also be expected, as triangularity at q=1 is much reduced compared to at the edge of the plasma. Inversion radii do not vary so significantly, but are generally larger for LL pulses at a given β_N.

Influences on NTM threshold

The strong correlation between the time of NTM onset and a sawtooth crash, shown in Table 2.1, confirms that sawteeth are the triggering mechanism for the NTMs. The only exception occurs where an NTM onset coincides with a peak in sawtooth related n=1 activity, rather than the crash itself.

Table 2.1 Correlation between NTM onset and sawtooth crash

Pulse	**NTM onset time (s)**	**Sawtooth period (s)**	**$(t_{NTM}-t_{crash})/\tau$**	**$(t_{NTM}-t_{peak\ n=1})/\tau$**
49572	22.09	0.18	0.91	0.000
49579	21.82	0.48	0.021	0.010
49586	24.33	0.28	0.011	0.046
49596	19.73	0.40	0.012	0.121
49164	18.00	0.44	-0.009	–
49168	17.78	0.58	-0.003	–
49566	23.354	–	–	–

The lower threshold observed for LL pulses correlates well with the observation of larger sawtooth events for LL plasmas. This is likely to be the main reason for the lower thresholds. However, as discussed in section 2.1 the other terms in the sawtooth coupling and the modified Rutherford island evolution equation will also depend on shape, and may play a role.

Table 2.2 Relative sizes of the q=1 and q=3/2 surfaces

(m)	**HH q_{95}=3.4** **49596, ~59.7s**	**LL q_{95}=3.4** **49579, ~62.1s**
R(inv’ n) ECE	3.38	3.30/cor to Zmag
R(q=1.5) ECE	3.57	3.48/cor to Zmag
R_{magax} EFIT	3.13	3.06
$R_{cen\ q=1.5}$ EFIT	3.08	3.02
r (inv’ n) **r (q=1.5)**	**0.51**	**0.52**

A comparison of the relative sizes of q=1 and q=1.5 surfaces (the sawtooth and NTM resonant surfaces) shows little change with plasma shape. This is shown in table 2.2 which lists the locations of the inversion radius and the q=3/2 surface for a typical HH and LL pulse. Thus, we expect that the coupling of the sawtooth to the NTM surface (which occurs via 2,2 harmonics of the sawtooth) to be similar for the two configurations.

Examining rotation profiles, the LL pulses all have much lower rotation, as shown in Fig.2.9, with differential rotation between q=1 (at R~3.3m) and 1.5 (at R~3.6m) much reduced. This will reduce the dynamic shielding of the sawtooth MHD, making the seeding process easier (and so seed island larger), offering further potential to lower thresholds for LL pulses. It is interesting to note that at the time of NTM onset, there is no locking between the q=1 and q=1.5 surfaces.

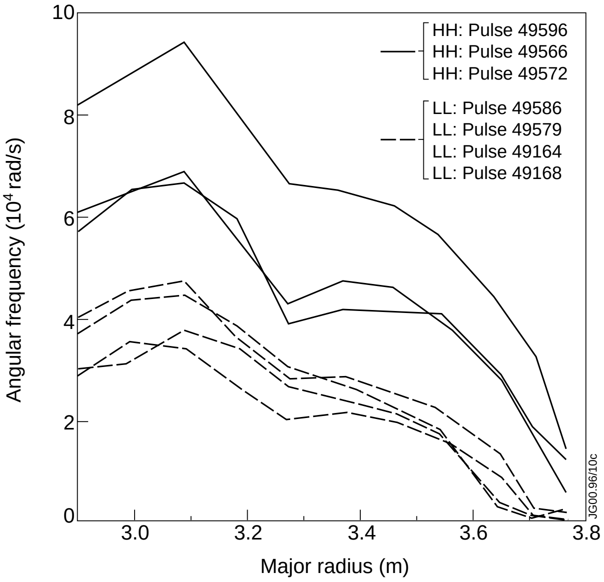

Fig.2.9: Rotation profiles (measured by charge exchange) vs major radius (m), for shape scan pulses at times of NTM onset. Despite similar heating powers, β_n, and ranges in toroidal field, the LL pulses all have substantially lower rotation.

To examine other terms in the evolution equation for the NTM, analyses are underway to fit the island evolution equation to the full mode evolution as β changes. This will show variation in the various NTM drive/suppression terms - Δ', bootstrap current, island size at onset and ion polarisation effects.

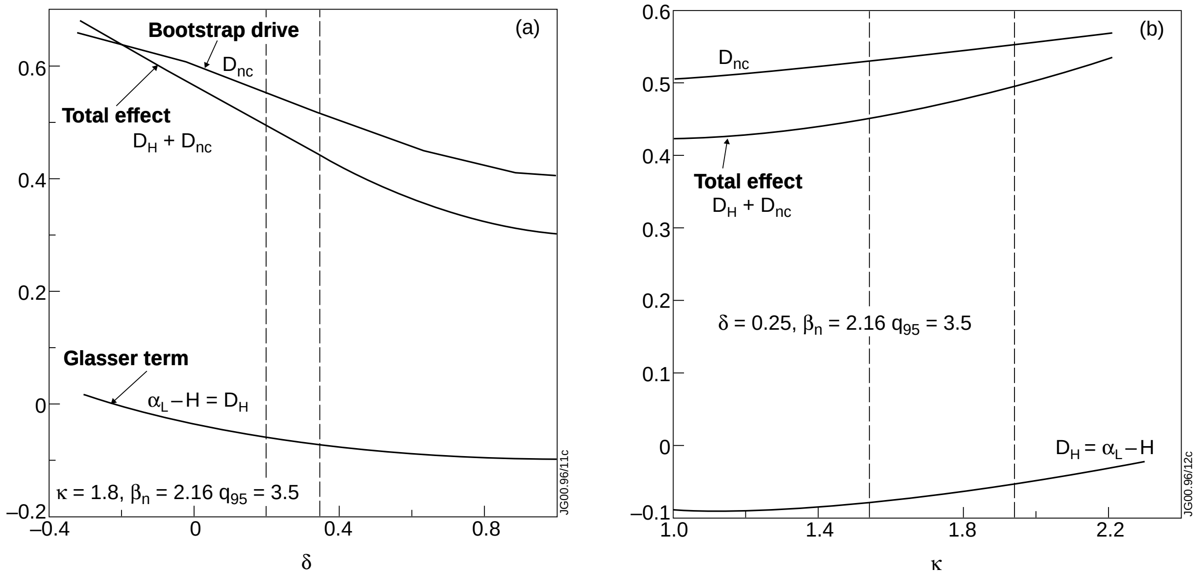

Fig.2.10: Effect of the bootstrap and Glasser terms

Finally variation in the bootstrap and Glasser terms may be playing a role. Although this cannot be calculated for small island sizes, it can be calculated when island sizes are saturated, and thus act as a reasonable indicator of the size and direction of the effect. Calculations based on standard shape plasmas, based on the equilibrium profiles, (see Fig.2.10) indicate the shaping effects are relatively weak and may cancel out. However, these calculations scan separately in elongation and triangularity; as there are strong cross terms involved, a full calculation must be done (and is underway) to exactly reproduce LL and HH shapes. .

2.3 Summary and future directions

There is no significant difference in NTM thresholds in β_N between high and low shaping pulses on JET. However, when parameters more closely associated with the physics mechanisms underlying NTM behaviour are examined, a clear difference is observed, with thresholds higher for high shaping configurations.

Much of the effect of a lower NTM threshold at lower shaping can be explained in terms of the seeding of the NTM, with sawteeth events larger at lower shaping, and differential rotation (between q=1 and q=1.5) lower (which implies weaker dynamic shielding) - both of which contribute to the lower NTM threshold. Geometric coupling factors are thought to be less significant, with little variation in the ratio of sizes of the q=1 to q=1.5 surfaces. The role of the seed is confirmed by the strong correlation between sawteeth and NTM onset.

Further analyses are underway to examine variation of other drive terms in the evolution equation. Initial results indicate that changes in bootstrap and Glasser terms have a weak effect and elongation and triangularity dependence may cancel out. Clearly there is a need to further investigate the seeding process and understand the underlying mechanisms more fully, not least to validate the assumptions in present models.

The higher thresholds (in local parameters) with higher shaping are encouraging for ITER-FEAT and an enhanced JET, but of course limits in global parameters (β_N) will also depend on profiles. The smaller sawteeth in the more shaped discharges are also encouraging from a confinement perspective.

2.4 Pulse List

The following tables list the pulses for the ITER shape scan experiments in Weeks 43 and 47. They are listed as the six separate scans.

High elongation and high triangularity (HH) scan at 2.1 T / 1.8 MA

Pulse number	B [T]	I [MA]	q_{95}	kappa	delta	PNBI [MW]
49126	2.1	1.8	3.1	1.9	0.31	18
49128	2.1	1.8	3.1	1.9	0.31	15
49129	2.1	1.8	3.4	2.0	0.37	18
49130	2.1	1.8	3.3	1.9	0.35	19
49131	2.1	1.8	3.3	1.9	0.34	16
49133	2.1	1.8	3.4	1.9	0.33	15
49134	2.1	1.8	3.4	1.9	0.36	19
49136	2.1	1.8	3.3	1.9	0.34	19
49137	2.1	1.8	3.3	1.9	0.35	19
49138	2.1	1.8	3.3	1.9	0.36	17
49139	2.1	1.8	3.3	1.9	0.36	18
49160	2.1	1.8	3.3	1.9	0.36	15
49161	2.1	1.8	3.4	1.9	0.36	17
49591	2.1	1.8	3.3	1.9	0.36	16
49592	2.1	1.8	3.3	1.9	0.36	17
49596	2.1	1.8	3.4	1.9	0.36	17

High elongation and high triangularity (HH) scan at 2.7 T / 2.5 MA

Pulse number	B [T]	I [MA]	q_{95}	kappa	delta	PNBI [MW]
49140	2.7	2.5	3.2	1.9	0.33	12
49144	2.7	2.5	3.2	1.9	0.33	16
49145	2.7	2.5	3.3	1.9	0.35	18

High elongation and high triangularity (HH) scan at 2.7 T / 1.8 MA

Pulse number	B [T]	I [MA]	q_{95}	kappa	delta	PNBI [MW]
49152	2.7	1.8	4.5	1.9	0.35	17
49153	2.7	1.8	4.5	1.9	0.35	15
49154	2.7	1.8	4.5	1.9	0.36	18
49156	2.7	1.8	4.5	1.9	0.36	18
49157	2.7	1.8	4.5	1.9	0.35	15
49159	2.7	1.8	4.4	1.9	0.34	14

High elongation and low triangularity (HL) scan at 1.9 T / 1.8 MA

Pulse number	B [T]	I [MA]	q_{95}	kappa	delta	PNBI [MW]
49146	1.9	1.8	3.2	1.8	0.18	17
49147	1.9	1.8	3.3	1.8	0.19	17
49149	1.9	1.8	3.3	1.8	0.19	18
49151	1.9	1.8	3.3	1.8	0.18	17
49573	1.9	1.8	3.3	1.8	0.19	17

Low elongation and low triangularity (LL) scan at 2.7 T / 1.8 MA

Pulse number	B [T]	I [MA]	q_{95}	kappa	delta	PNBI [MW]
49164	2.7	1.8	3.2	1.6	0.23	13
49165	2.7	1.8	3.2	1.5	0.24	15
49166	2.7	1.8	3.2	1.5	0.24	14
49167	2.7	1.8	3.2	1.5	0.24	11
49168	2.7	1.8	3.2	1.5	0.23	15
49169	2.7	1.8	3.2	1.5	0.23	15
49170	2.7	1.8	3.2	1.5	0.23	14
49172	2.7	1.8	3.2	1.5	0.23	15
49173	2.7	1.8	3.2	1.5	0.22	15
49581	2.7	1.8	3.2	1.5	0.23	12
49582	2.7	1.8	3.2	1.5	0.23	18
49583	2.7	1.8	3.2	1.5	0.23	14

Low elongation and low triangularity (LL) scan at 2.7 T / 2.2 MA

Pulse number	B [T]	I [MA]	q_{95}	kappa	delta	PNBI [MW]
49180	2.7	2.2	2.6	1.6	0.21	13
49181	2.7	2.2	2.6	1.6	0.20	14
49182	2.7	2.2	2.6	1.6	0.21	16
49185	2.7	2.2	2.7	1.6	0.20	15
49186	2.7	2.2	2.6	1.6	0.20	11

Shape scan pulses with NTMs

Pulse number	B [T]	I [MA]	q_{95}	kappa	delta	PNBI [MW]	NTM onset time
49164	2.7	1.8	3.2	1.6	0.23	13	58
49168	2.7	1.8	3.2	1.5	0.23	15	57.78
49566	1.45	1.35	3.6	1.9	0.37	16	63.35
49572	1.4	1.5	2.72	1.9	0.36	16	62.09
49579	1.7	1.15	3.4	1.6	0.23	8.1	61.82
49586	1.6	1.3	2.67	1.6	0.22	15.5	64.33
49596	2.0	1.85	3.35	1.9	0.36	17.4	59.73

Acknowledgements

This work was funded by EURATOM, under the JET data validation contract. Also thanks are due to G Huysmans and M Zabiego for help with Fig 2.10 and the associated theory work.

References

[2.1] “The ITER project: ITER-FEAT”, presentation at 7th European Fusion Physics Workshop, Kloster Seeon (1999) (p639 of proceedings).

3. THE INTERPLAY BETWEEN PELLETS AND ITBS

C Gowers[1]

JET Joint Undertaking, Abingdon, Oxon, OX14 3EA, UK
[1] Euratom/UKAEA Fusion Association, Culham Science Centre, Abingdon, UK.

3.1 Overview

During the autumn 1999 campaign a High Field Side (HFS) pellet launcher became available for the first time at JET and the effect of injecting pellets into plasmas with an existing Internal Transport Barrier (ITB) was further investigated. Experiments were conducted to determine:

1. the lifetime of an existing ITB after pellet injection
2. the differences between HFS and Low Field Side (LFS) pellet injection
3. the differences in performance between using an ELMy and an L-mode target plasma
4. the overall electron density evolution with and without pellets - the aim being to try to raise the density in ITB plasmas by injecting pellets
5. if pellets can be used to peak up the density in the target plasma as in the past with the so called PEP (Pellet Enhanced Performance) modes [3.1]

3.2 Results

1. Pellets into plasmas with existing ITBs

Figure 3.1 shows a selection of signals from #49006, a reference ITB plasma pulse in which the ITB formed at around 5 s. The upper trace shows the line integrated density from a vertical chord of the FIR interferometer overlaid with the calculated line integral signal from the measured LIDAR density profile. The next trace is the D_α showing the plasma going ELM free just prior to the giant ELM at 5.81s. The centre trace is the neutron rate which increases rapidly once the full heating begins at 4.2s. The bottom trace shows the Ar influx which is added to control the edge conditions. All the pulses in the series had Ar added.

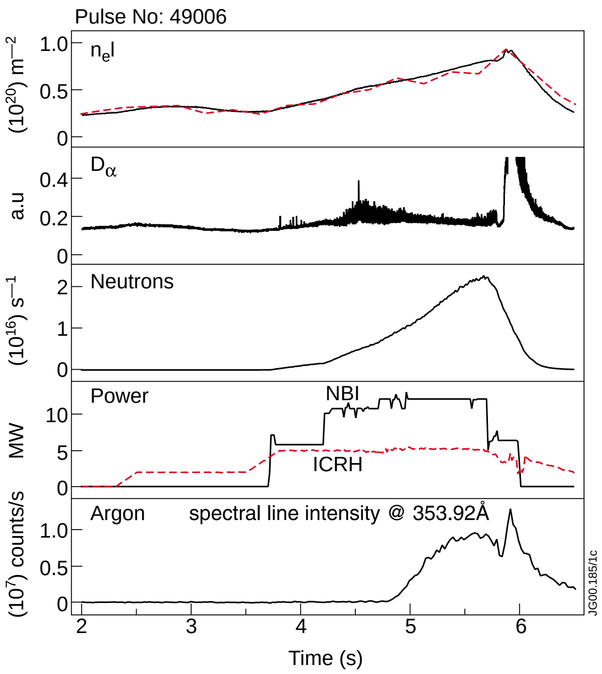

Fig.3.1: Typical reference ITB pulse with argon seeding

The formation of the ITB can be seen in the electron temperature profile where a steep gradient forms. This is shown here in Fig.3.2 where the occurrence of the steep gradient region can be seen by plotting several different frequency (and therefore radii) channels of the ECE heterodyne diagnostic(lower trace). The steep gradient region on the profile is seen as an increasing separation of the signals from adjacent channels . This can sometimes be seen more clearly if the difference between adjacent ECE channels is plotted (upper trace). The formation of the ITB appears as a “spike” on one or two of these difference signals. In this pulse the ITB remained until just after the heating was stepped down at 5.7s.

The second pulse, #49012 Fig.3.3, started in a similar way but a HFS pellet was fired in at 5.18 s as can be seen on the density and D_α traces. This clearly leads to the destruction of the ITB as can be seen again in the ECE traces Fig.3.4 where the signals, having initially separated at barrier formation, collapse back together as the plasma rapidly cools on the arrival of the pellet. This behaviour was typical of all pellet pulses fired into existing ITB’s in the Autumn 1999 campaign, be they HFS or LFS pellets. #49012 was interesting because only one HFS pellet was used and the ITB reformed at about 5.53s, some 350 ms after the arrival of the pellet.

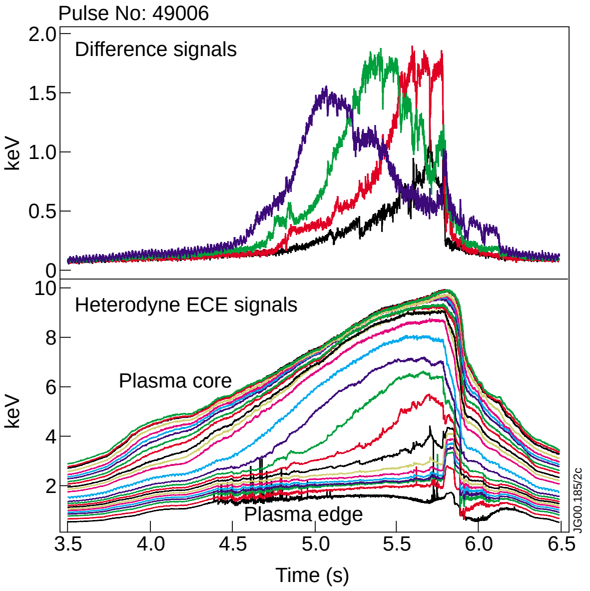

Fig.3.2: ECE signals from various radii across the plasmas (odd channels of KK3/TE01to TE19), the formation of the barrier is evident from the separation of channels as indicated by the upper difference signals

Generally, since one of the aims was to try to increase the peak density of the ITB discharges by using the pellets, several pellets were fired in at 4 or 5 Hz. Thus any reforming ITB was quenched by the arrival of another pellet. Figures 3.5 and 3.6 show this for pulse 49008. The

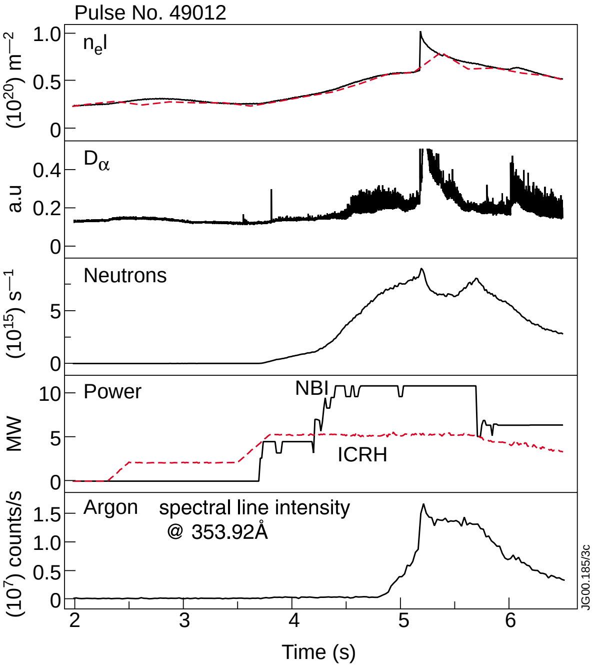

Fig.3.3: Typical pulse(49012) into which a pellet is fired at 5.18s after the ITB is formed

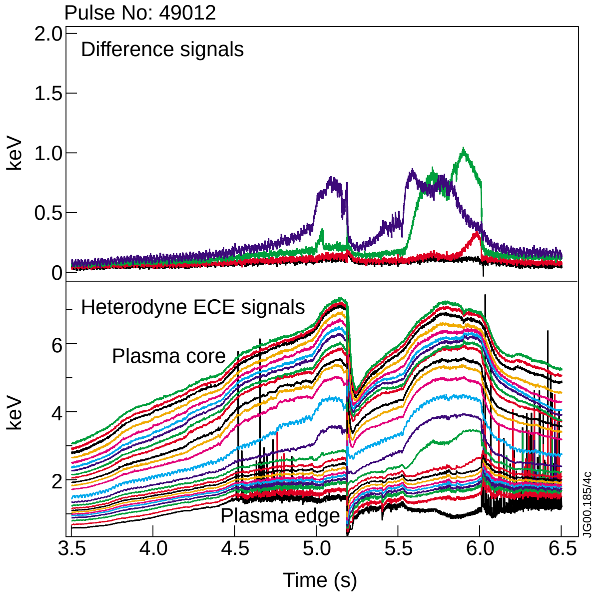

Fig.3.4: As Fig.3.2 but for pulse 49012

density trace, Fig.3.5 upper, shows the pellets arriving at ~5.14 and 5.34s. There is a hint that the barrier had begun to reform as can be seen by brief recovery of the neutron rate signal, Fig.3.5 (centre), the ECE channel separation, Fig.3.6 lower and the spike at 5.3 on the upper traces.

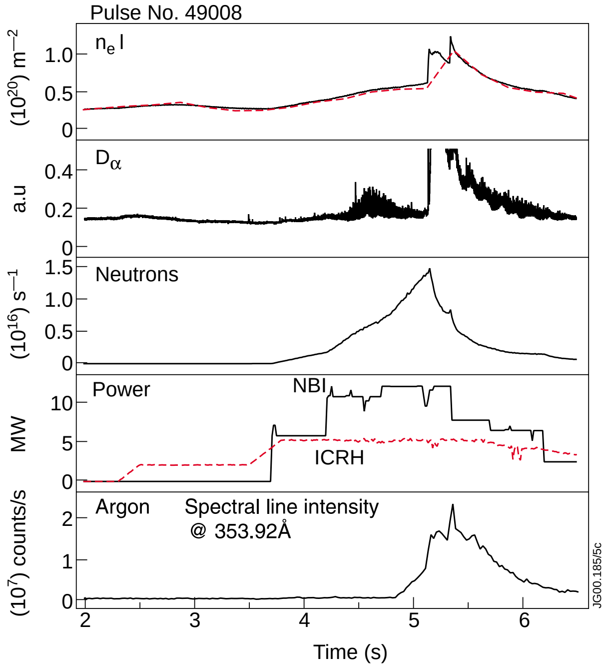

Fig.3.5: Typical pulse (49008) into which 2 pellets are fired at 5.14s and 5.34s after the ITB is formed

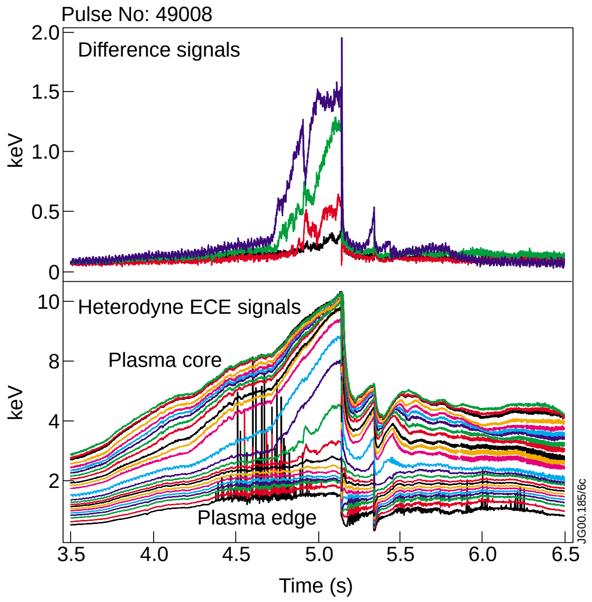

Fig.3.6: As Fig.3.2 but for pulse 49008

Figure 3.7 shows a comparison of several channels of the ECE heterodyne system on 2 different discharges, one, #49676, had a HFS pellet injected and the other, #49675, had a LFS pellet injected. The temperature drop close to the plasma axis in the former was about 3keV while for the latter it was only just over 1 keV. Also the time to reach the minimum T_e on axis compared with the time of the start of the T_e drop at the edge (arrival time of the pellet in the plasma) was only about 50-60 ms for the former but 120ms for the latter . Clearly pellets launched from the HFS have a more dramatic effect on plasmas with pre-formed ITB's than do LFS pellets.

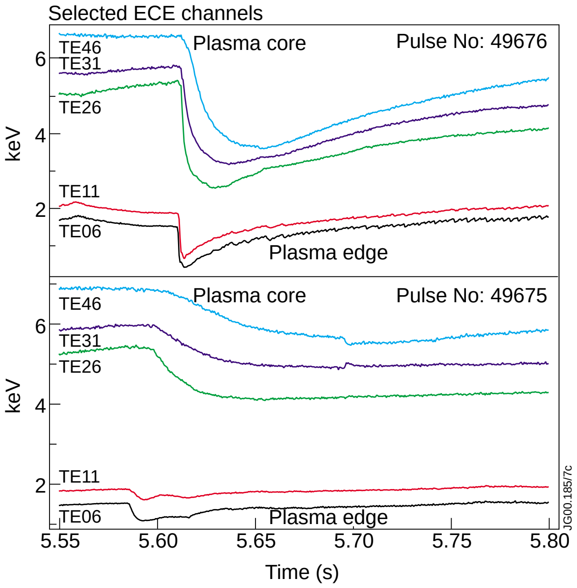

Fig.3.7: Comparison of effect on ECE temperatures of HFS (upper plot) and LFS (lower plot) pellets

Both ELMy and "L-mode" target plasmas were used in the ITB+pellet series to establish if there were advantages in using one or the other. The "L-mode" cases were deemed to be those in which the type III ELMs had all but disappeared as shown in Fig 3.8. The figure depicts example D_α.traces for several of the pulses in the series, some were HFS and some LFS pellets as indicated. However, the outcome was always similar to that shown in Fig 3.7, i.e. the type of target plasma did not affect the outcome, the pellet destroyed the barrier either rapidly (HFS) or more slowly (LFS).

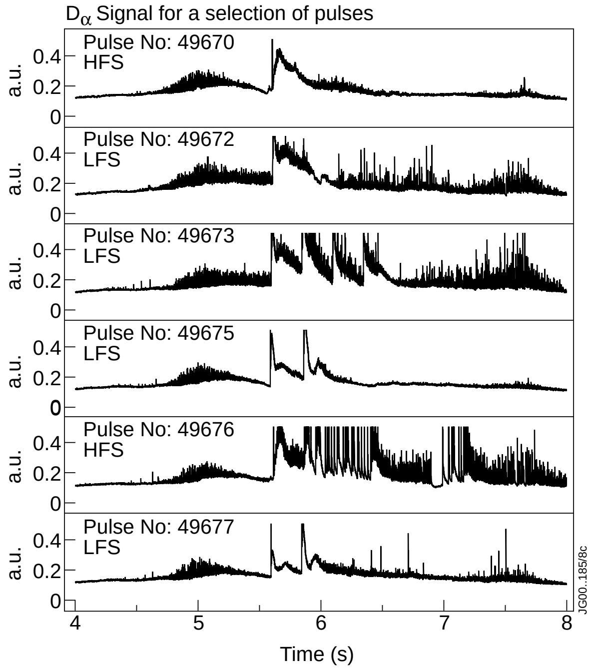

Fig.3.8: D_α traces for a selection of HFS and LFS pellets with L-mode and ELMy H-mode target plasmas

The density evolution story is shown in Figs 3.9 and 3.10. On the left hand side of each figure are traces from the reference pulse. The top traces are the now familiar heterodyne ECE signals showing the barrier formation. Below are shown a series of overlaid density time traces for a number of near centre radii from the 4 Hz LIDAR Thomson scattering system. In the lowest box these time traces are averaged to form an average central density trace. This simply produces a central density with reduced statistical spread compared with a single axial LIDAR trace. On the right hand side in each figure are the similar boxes for either #49012,

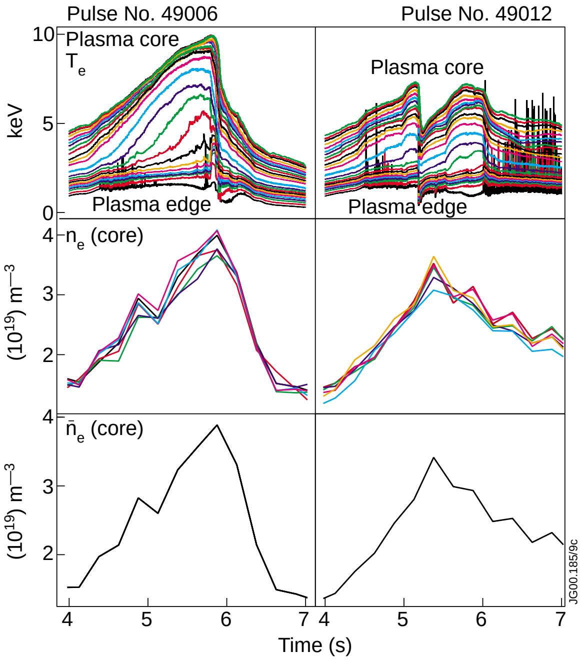

Fig.3.9: ECE temperatures (upper traces), central LIDAR densities (middle traces) and average of these densities (lower traces). The left hand figures are for a non-pellet reference shot while the right hand figures have a pellet at 5.18s.

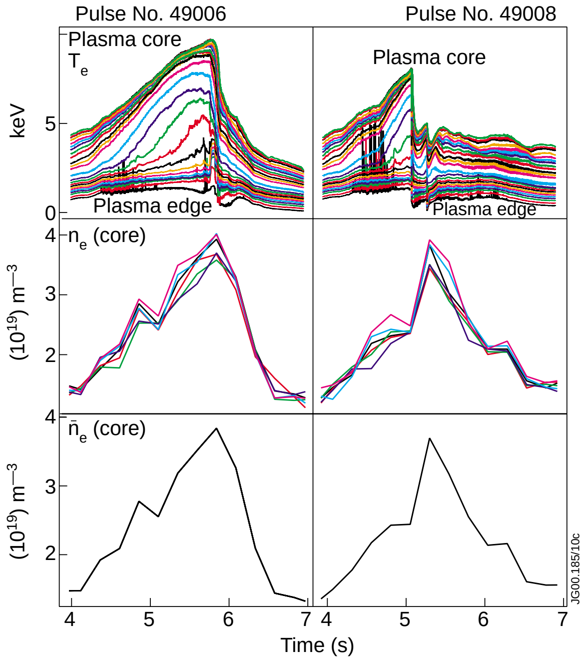

Fig.3.10: As Fig.3.9 but comparing non-pellet reference (left hand figures) with a 2 pellet HFS shot (right hand figures)

Fig.3.9 or #49008, Fig.3.10. In the former, as we have seen, only one HFS pellet was injected and the ITB recovered. However, what we observe when we compare the density traces is that although the ITB recovered and despite the introduction of the HFS pellet, the peak density achieved was still somewhat less than that produced when no pellet was injected and the density rise was that associated with NB.

In the latter case, #49008 was a pulse in which a second pellet was injected just as the ITB was reforming after destruction by the first pellet. However, in this case, the density peak immediately after the second pellet does appear to be equivalent to that of the reference pulse which had no pellet injection. This may indicate the way to increase the density in ITB plasmas i.e. fire in several pellets but at a lower rate. From #49012 one would deduce that a series of 2 Hz pellets should be tried. This would give a clear recovery period for ITBs to reform after each pellet and may allow the density to be "ratchetted" up to a level significantly higher than in the reference, no pellet, case.

Table 3.1 lists the pulses in which pellets were injected into existing ITB plasmas in the Autumn 1999 campaign and summarizes some of the measurements above.

Results 2. PEP-mode attempts

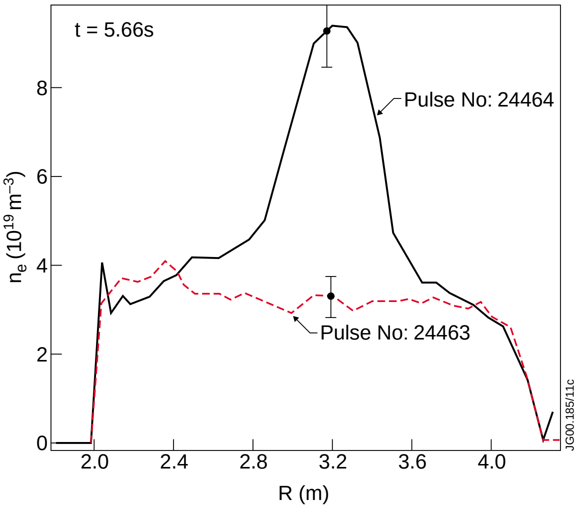

Fig.3.11: Density peaking achieved in a 1992 PEP mode (24464)

Here the aim was to try to reproduce target density profiles similar to those generated in the past in the so called Pellet Enhanced Performance mode. An example of the steep gradient, high central peak density profile produced in the past is that shown in Fig.3.11. This shows LIDAR n_e profiles for old pulses #24464 (with pellet) and #24463 (reference without). It should be noted that PEP modes were re-established in 1998 (eg pulse 46365)

Some typical traces for a pulse in the Autumn 1999 campaign are shown in Fig.3.12 for pulse #49338. This shows the q(0) from EFIT in the top box followed by the heating waveforms, the number of pellets and their timing and the evolution of the resulting neutron rate in the bottom box.. For this pulse, the density profiles from the LIDAR system just before and just after the pellets were injected are shown in Fig.3.13. The sequence shows that initially, the pellet ablates in the outer regions of the plasma producing hollow density profiles . These then proceed to "fill in" to produce the target n_e profiles like that at 3.627 s.

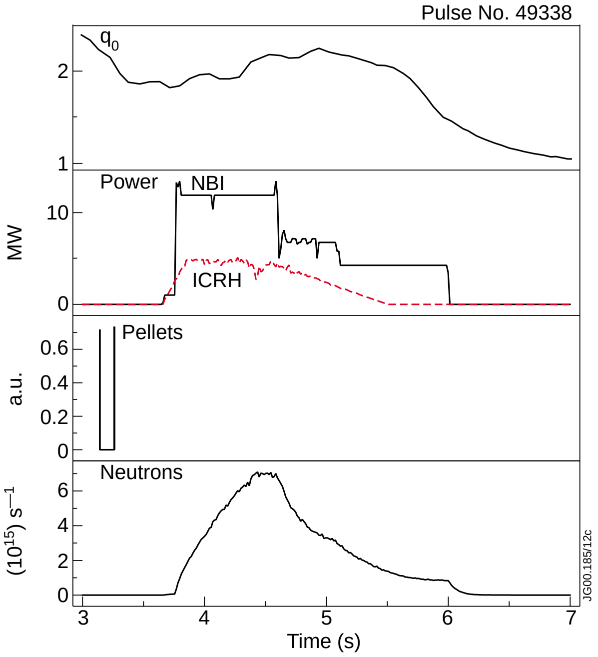

Fig.3.12: Time traces for a PEP mode attempt from the Autumn 1999 campaign

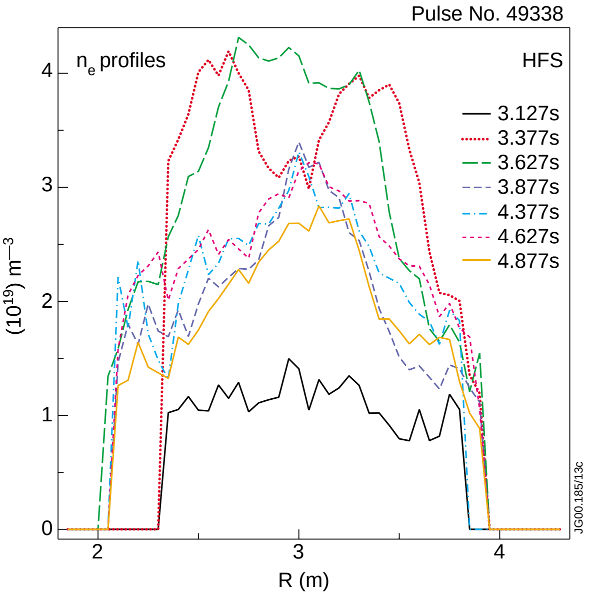

Fig.3.13: Evolution of the density profile for the pulse shown in Fig 3.12

Although peaked on axis, these are rather broad density profiles and the peak value is not very high in comparison with the old data. There were 2 notable exceptions in the data set. Virtually all the HFS pellet launches produced results like those for #49338 except #49334, Figs 3.14 and 3.15. The target n_e profile for this pulse at 4.127s has a density peak which although small, bears a remarkable resemblance (steep gradient, central peak) to those of the old PEP mode. In addition, for this pulse the q(0) evolution is significantly different. Unlike the rest in which EFIT indicates that the q(0) hovers around 2, for #49334, q(0) plunges down towards1.

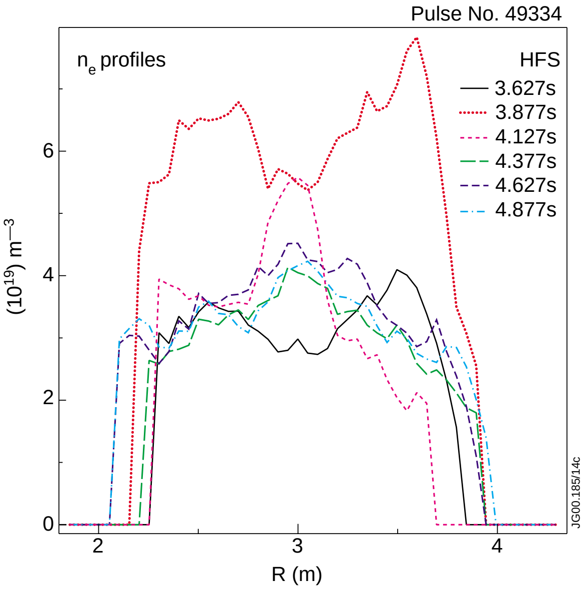

Fig.3.14: Evolution of the density for pulse 49334 which has string of HFS pellets before the heating is applied (see Fig.3.15)

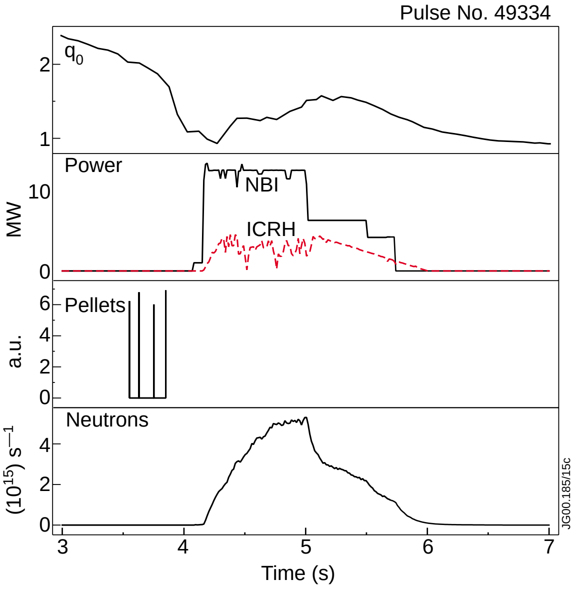

Fig.3.15: Time traces for pulse 49334

A similar difference has been observed when trying to form an ITB. In plasmas which do not form an ITB, q(0) stays high i.e. above 2 whereas in plasmas that do form an ITB, q(0) does swiftly move to values of q(0) significantly below 2.

Figures 3.16 and 3.17 show the results for a LFS pellet launch #49357. Here again the behaviour is remarkably different in that the density reached is a factor ~3 higher than for the HFS launch. This was the only PEP attempt in the campaign with a LFS launch. Clearly, both these cases warrant further study in the coming campaigns in the attempts to raise the density in ITB plasmas.

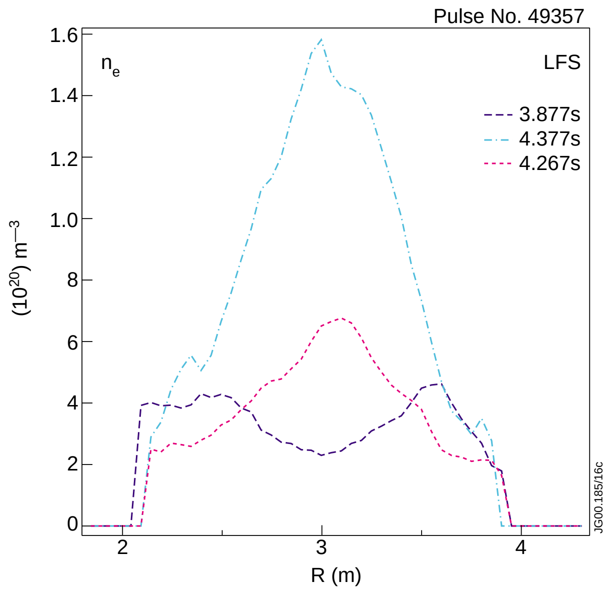

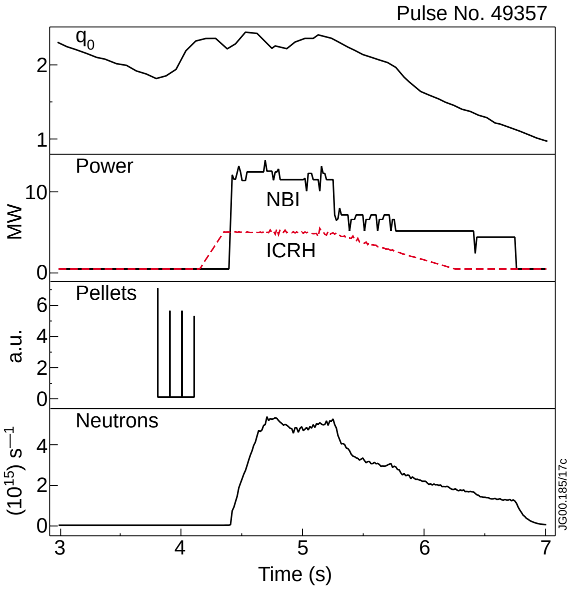

Fig.3.16: Evolution of the density for a LFS PEP mode attempt

Fig.3.17: Time traces for pulse 49357

Table 3.2 lists the PEP attempt pulses of the Autumn 1999 campaign. It also contains the number and timing of the last pellet and the start time of the main NB heating pulse. The results, though not as good as the old PEP performance, are nevertheless in some cases within about 30% in terms of R_{nt} of the results achieved in the past.

3.3 Summary and future directions

In no case studied in the Autumn 1999 campaign did a pre- existing ITB survive pellet injection. However, ITBs did reform after the pellet induced collapse. The decay time of the core T_e is significantly shorter for HFS pellets than for those from the LFS. Choosing ELMy or L-mode target plasmas made no significant difference to the outcome. In this data set, reformed ITB plasmas after pellet injection did not produce higher central densities than plasmas without pellet injection. However, the pellet rate at 4 Hz was certainly too high to allow ITB recovery for any significant time between pellets. Only modest performance enhancements of R_{nt} were achieved in PEP mode target plasma attempts but these were within about 30% of those produced in the past.

In the future we should:

- To try to raise the density in ITB plasmas, a pellet rate of no greater than 2 Hz should be used. This should allow the ITB to recover and last for a sufficient time to re-establish some density recovery which may yet lead to “ratchetting up” of the central density.
- In addition, LFS pellet injection should be used as this seemed less destructive
- Try smaller (1/2 size?) pellets to lessen the impact and allow faster recovery
- For PEP mode targets, try to build on the n_e profile of #49334 which although lower density, was remarkably similar to the old PEP modes. Also try to use LFS pellet injection in this case.

Decisions on future directions for pellet experiments should be aided by pellet ablation modelling which is now proceeding in some EURATOM Associations.

3.4 Shot List

Table 3.1 lists the pulses in which pellets were injected into existing ITB plasmas in the Autumn 1999 campaign and summarizes some of the main parameters.

Table 3.1: Pulses from the Autumn 1999 in which pellets were fired into an existing ITB

Pulse	**pellet 1 time**	**pellet 2**	**pellet 3**	**pellet 4**	**HFS or LFS**	**Plasma at Inj. Time**	**Decay core (ms)**	**t(ms) edge**	**Tot pow (MW)**
49006	None	REFERENCE PULSE				Grassy ELMs			17.5
49008	5.1				H	ELMy	70,	~1ms	17
49012	5.2				H	ELMy	45,	~1ms	16
49015	5.25				H	~L-mode	65,	~1ms	17.5
49666	5.6	5.85			H	~L-mode	39, 25, 35	~1ms	22
49668	5.6	5.85			H	~L-mode	45, 36	~1ms	22
49670	5.6				H	L-mode	40,	~1ms	22
49672	5.6				L	ELMy	160,	~5ms	22
49673	5.6	5.85	6.1	6.35	L	ELMy	100, 100	~3ms	23
49675	5.6	5.85			L	L-mode	98, 120	~5ms	21
49676	5.6	5.85			H	~L-mode	54,	~1ms	23
49477	5.6	5.85			L	~L-mode	100,		24

Table 3.2 lists the PEP attempt pulses of the Autumn 1999 campaign. It also contains the number and timing of the last pellet and the start time of the main NB heating pulse.

Table 3.2: PEP attempt pulses of the Autumn 1999 campaign (Ip=2.5MA and Bt=2.6T pulses)

Pulse no	NB (MW)	RF (MW)	Pellets	LFS or HFS	Time last pellet	NB on	dt	ne(0)	ne peak	Wdia (MJ)	HFS	Rnt LFS	24464
49330	6.9	4.7	2	High	44.1	44.157	0.057	1.9	1.171		0.17		
49331	12	5	3	High	44.1	44.16	0.06	4.6	1.313	3.3	0.37		
49332	12	5	4	High	44.1	44.4	0.3	5	2.063	4	0.53		
49333	12	5	3	High	43.85	44.16	0.31	4.6	2.016	4.1	0.63		
49334	12.5	4	4	High	43.85	44.16	0.31	5.6	3.802	4.1	0.53		
49338	12	4.8	2	High	43.25	43.75	0.5	4	1.86	4.1	0.7		
49339	11.5	5	3	High	44.35	44.67	0.32	6.5	2.133	4.2	0.6		
49352	12	5	4	High	44.1	44.4	0.3	4.8	1.895	4	0.6		
49357	12	5	4	Low	44.1	44.4	0.3	14.5	2.594	3.6		0.36	
49358	12	5	3	High	45.1	45.4	0.3	6.2	1.874	4.2	0.65		
24464	13	0	1	Low	45	45.02	0.02	9		7			0.95

References

[3.1] C D Challis et al. Fusion Engineering and Design 26 (1995) 17-28

4. OBSERVATION OF SNAKES IN THE OPTIMISED SHEAR REGIME

B. Alper[1], S. Allfrey[1], Yu. F. Baranov[1], D.N. Borba[2], T.C. Hender[1], N.C. Hawkes[1]

JET Joint Undertaking Abingdon, Oxon, OX14 3EA, UK.
[1] EURATOM/UKAEA-Fusion Association, Culham Science Centre, Abingdon, Oxon, UK.
[2] EFDA–JET Close Support Unit, Abingdon, Oxon, OX14 3EA, UK.

4.1 Overview

Background

Snakes with an (m,n)=(2,1) topology were regularly seen in Optimised Shear (OS) discharges[1] following formation of a strong Internal Transport Barrier (ITB). These snakes were seen in cases where a strong ITB formed inside, but close to, the q=2 magnetic surface. Their formation is believed to be dependent on the low magnetic shear and low values of transport coefficients that prevail locally under these conditions.

The radial location of the snake was inside, but near the foot of the ITB. It generally moved inwards with time**.** Erosion of the ITB, from the outside inwards, took place following formation of the snake. This led to loss of both the ITB and the snake. The enhanced heat loss from the erosion of the ITB usually resulted in an ELM-free H-mode and a termination of the good confinement phase with a Giant ELM. However, when impurities (e.g. Ar or Kr) were puffed in to the plasma to cool the edge, a cyclic ITB /snake behaviour could be observed.

Objectives

The primary aim, here, is to produce a database of pulses from the autumn ’99 experiments where snakes have been identified and where possible to detail, in time and space, the location of the q=2 surface as an aid to magnetic profile analyses. In addition, an evaluation of snake phenomenology and the conditions under which they occurred would be carried out.

4.2 Results

Results of the survey

A detailed survey of fast magnetics data for Task Force B/C shots was carried out. Fourier spectra from the 1MHz magnetics data of the KC1F diagnostic were examined from the autumn 1999 campaigns. Signs of the multiple-harmonic traces, characteristic of the presence of snake as illustrated in Fig.4.1, were sought.

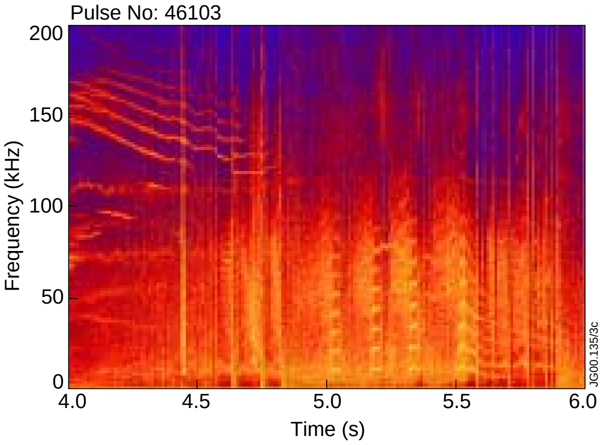

Fig.4.1: Fourier spectrogram from the KC1F diagnostic showing the multiple harmonic character of the snake which appears 4 times between 5.0 and 5.6s.

Those discharges in which a *possible* snake was identified are summarised in Table 4.1.

Table 4.1: A detailed summary of all the snake-candidate shots from the autumn '99 campaign. In only ~4 shots was a clear unambiguous signature of a snake apparent in the raw data.

Shot	Times	CATS Window?	Type	Comments
48907	5	No	Startup	Lives for~100ms
48960	5/5.2	No	Startup	Clear KC1F data
48974	5	Yes at 3.55m	Startup	Weak but just visible
49017	5.3-5.7	Yes	High -βn	Many (~11) too faint to see in raw data
49340	5.4	Yes at 3.4m	NBI only	Long Lived (200-400ms)/ Good CATS/ (3,1) from Mag?
49342	5.3	Yes (at 45.65s)	NBI only	Long Lived mode (over 400ms) -kink rather than snake
49365	5.5	No	NBI only	Snake becomes kink mode
49392	4.5	Yes	Sept. Av.	4 extremely short bursts, probably a chirp?
49406	7.2	Yes	Sept. Av.	one extremely short event swamped by other large MHD
49415	6.7	No	Sept. Av.	one , ~20ms, between CATS windows
49615	6.0-6.3	No	High -βn	only a faint hint
49616	6.1-6.3	No	High -βn	maybe 3 faint bursts in KC1F
49618	6.0-6.2	Yes	High -βn	similar to 49616 - lost in background
49619	5.9 - 6.1	No	High -βn	similar to 49616
49680	6.2	No	LH preheat	~20ms duration
49788	5.9	No	High -βp	more like WB mode than snake
49794	5.9	Yes	High -βp	Faint hint only - not visible in raw data
49798	6	Yes	High -βp	2 short bursts - global mode dominant

Where a snake was suspected, more detailed examination was performed using data from the CATS fast data acquisition system provided a fast window was available at that time. Otherwise, the raw data traces from only the CATS continuous magnetics channel were used.

From this survey it became apparent that:

- the occurrence of snakes was low in the autumn campaign,
- where present, the snakes generally produced only a weak magnetic signal and were almost undetectable in the SXR and ECE data,
- they had little or no apparent effect on confinement … and
- in a number of cases evolved into an 'internal kink' mode i.e. a harmonically purer, less localised, (m,n) = (2,1) mode.

Only four cases of a ‘clear’ snake were observed in the data set and only one had good CATS data to localise the mode. This was shot 49340 with the snake centred on 3.42 metres. Valid MSE data is available for this discharge, so the location of a q=2 surface at this radius can be used as a constraint in any fit to the q profile.

For completeness a similar, but less detailed survey, of possible snakes from the spring 1999 campaign (i.e. pre – EPS ’99) was performed and is summarised in Table 4.2. The occurrence of snakes was somewhat higher here particularly in the earlier half of the campaign.

Table 4.2: A summary of snake candidate shots from the spring ’99 campaigns. Strong snake signatures were more common early in the campaigns.

Shot	Times	Comments	CATS Window?
47011	5.8	20ms ends barrier	No
47049	5.7	30ms strong	Yes
47057	6.1	30ms strong	No
47058	5.7	30ms strong	Yes
47070	6.0/6.3	30ms	No
47078	5.8	30ms strong	No
47104	6	2s snake?	No
47201	6.5	2s Global mode?	Yes (end)
47227	6	strong	No
47228	6.3	strong	No
47229	5.9	~30ms	No
47232	6.5	~20ms	No
47234	6.2	~20ms	No
47235	6.9	~10ms	No
47336	6.6	~20ms	No
47342	6.9	~10ms	No
47349	7.1	~10ms	No
47402	7.3	~10ms	No
47432	6.3	OK	Yes at 3.48m
47444	6.3/6.9	as ‘ 452	Yes at 3.55m /No
47449	6.2	Faint	Yes?
47452	6.3/6.8	snake & saturates	Yes/Yes
47459	7.1	Mode-locks	At onset
47685	5.3	faint	No

Shot	Times	Comments	CATS Window?
47705	5.3	Global mode?	Yes
47843	3.3	Long	Yes
47849	3.4	~400ms	Yes
47867	3.5	~30ms	
47868	3.5	~30ms	
47887	5.4	20ms faint	
47888	5.6	20ms faint	
47903	4.8	v.low freq.	
48163	5.7/5.9	20ms faint	
48165	5.2	20ms faint	
48167	5.2	20ms faint	
48168	5.2	20ms faint	
48169	4.2	20ms faint	

Snake Phenomenology

A detailed 'CATS' analysis of the properties of the snake for shot 49340 was performed. In Fig.4.2 a cross-correlation between the ECE (T_e) diagnostic and a magnetics signal was carried out. The multiple harmonics in the magnetics signal (trace (d)) are clearly seen in trace (c) which correlate well with the ECE data –trace (a) – at around 3.4m. Trace (b) indicates no phase change across the snake, suggesting a kink-like structure.

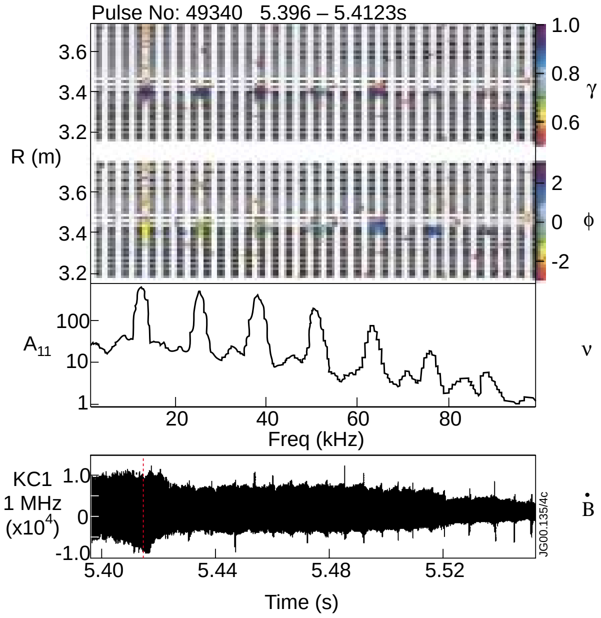

Fig.4.2: Plot of cross-correlation between a magnetics signal and the ECE diagnostic array (KK3). The strong coherence is localised at R=3.4m .

It is believed the relatively low rate of snake occurrence in this data set is primarily due to the fact that a push to achieve high performance OS shots was not an objective of the autumn '99 run. It is in such discharges that strong transport barriers occur which appear to be a key trigger to the formation of a snake. For comparison, a scatter plot of β_N vs. l_i for the data in Table 1 combined with data from earlier O.S. shots is presented in Fig.4.3. The four clear snakes are shown as filled circles and the rest as light squares. Their location on the plot is consistent with the earlier data set. The four snakes are also included for comparison with an

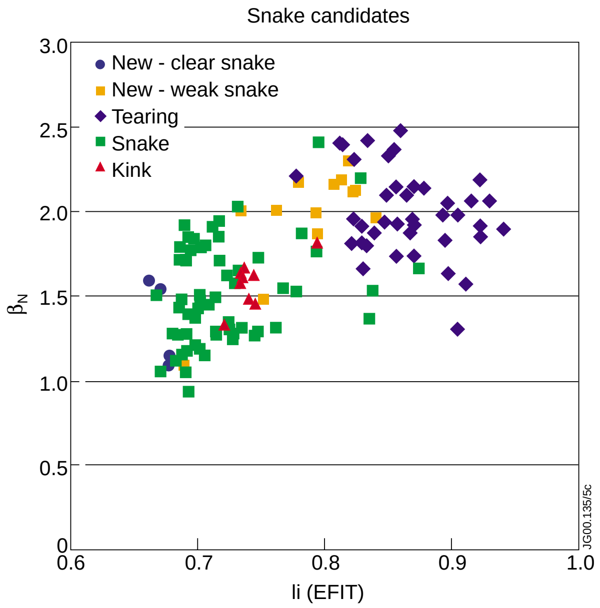

Fig.4.3: Scatter plot of β_N vs. l_I categorised according to MHD activity. The properties of autumn '99 data set are consistent with the earlier (pre EPS '99) shots.

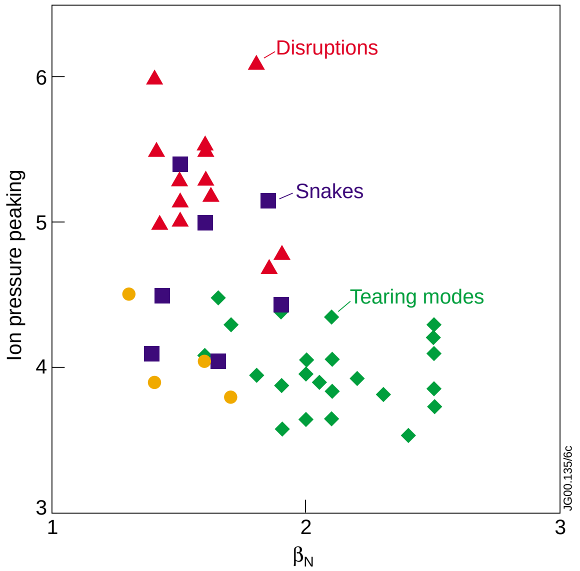

Fig.4.4: Scatter plot of ion pressure peaking vs. β_N for pre EPS '99 data (taken at peak performance) with the 4 clear snake candidates included as filled circles.

earlier data set in Fig.4.4 which shows a scatter plot of Ion Pressure Peaking against β_N. It should be noted that points in the earlier data set are taken at peak performance only.

As noted above, some of these shots evolved away from the localised structure of a snake into 'internal kink' modes. This is illustrated in Fig.4.5, which gives two 2ms snapshots, 60ms apart, of a magnetics signal for shot 49365. The relatively sharp spike, characteristic of a snake, seen in trace (a) soon evolves into a more regular signal, trace (b), characteristic of an internal kink.

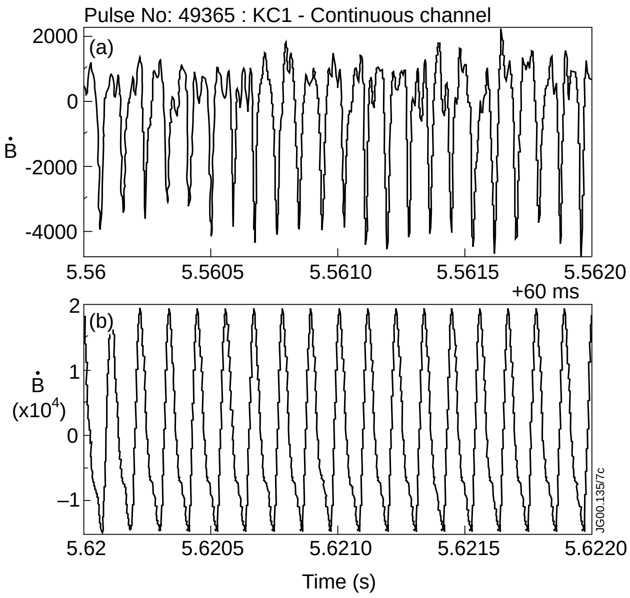

Fig.4.5: Magnetics signals for two 2ms windows separated by 60ms illustrating how the narrow 'spiky' signal characteristic of a snake evolves into a broader signal characteristic of an internal kink.

4.3 Summary

A comprehensive data set of m=2 snake occurrences from the 1999 campaigns has been produced. In general snakes were less prevalent in these campaigns than in the higher performance discharges from earlier O.S. campaigns. Where they did occur, their properties were consistent with those found previously. It is recommended that an examination of KC1F spectra for snake occurrences is carried out on the days immediately following an OS campaign and a record kept to aid subsequent q-profile analyses.

References

[4.1] Spontaneous appearance of q=2 Snakes in JET Optimised Shear Discharges, B. Alper *et al,* 26 th EPS Conf. on Contr. Fusion and Plasma Physics, Maastricht, 14 - 18 June 1999 ECA Vol.23J (1999) 173 – 176

5. HIGH NORMALISED BETA PLASMAS WITH INTERNAL TRANSPORT BARRIERS IN JET

C Gormezano[1] , Y Baranov[2], T C Hender[2].

JET Joint Uundertaking, Abingdon, Oxon, OX14 3EA, UK
[1] Present address: Associazone Euratom/ENEA sulla fusione, Frascati, Italy
[2] EURATOM/UKAEA Fusion, Association, Culham Science Centre, Abingdon, UK

5.1 Overview

The so-called advanced tokamak scenarios might allow more effective, and economic, reactor operation than the ELMy H mode reference scenario, considered for ITER. In addition to common requirements with the reference ITER scenario, such as those referring to access to high density operation, divertor compatibility and helium retention, advanced scenarios require operation with simultaneously:

- high confinement,
- high-normalised beta and
- high bootstrap current operation, i.e. high poloidal beta.

So far, some of these conditions have been achieved in plasmas with Internal Transport Barriers (ITB) where turbulence is at least partly stabilised either at the location of the ITB or within the ITB. This section will describe the results achieved in JET on the development of high confinement, high-normalised beta advanced scenarios based on plasmas with ITBs. It will be shown that steady plasmas with wide ITBs, high confinement and high-normalised beta (H89x β_N~7.3) have been achieved in Optimised Shear plasmas, by controlling edge conditions and pressure peaking through impurity injection and control of the heating waveform. In this type of discharge interaction with the septum is thought to lead to an eventual collapse of the ITB and techniques of avoiding the septum by moving the divertor strike-points has allowed steady high-normalised beta plasmas to be obtained. These data, together with data achieved at high β_P (see Section 6) are very encouraging for future developments on JET and for the future of advanced scenarios.

5.2 Results

Optimised Shear scenario with steady ITBs

In JET, plasmas with ITBs are produced in the so-called optimised shear scenarios [5.1] with pre-heating and the main heating during the current ramp-up phase of the plasma. A moderate heating (about 2 MW of Ion Cyclotron Heating, ICRH) during the ramp-up phase of the current (rate of about 0.4 MA/s) slows down the diffusion of the plasma current without triggering MHD activity, which in-turn might induce anomalous current diffusion. The timing of the main heating phase (Neutral Beam Injection, NBI, and ICRH) is adjusted to have a rational q surface, generally q=2, in the plasma of adequate radius [5.2]. In order to delay the triggering of an

H-mode (the applied power being generally higher than the L to H-mode power threshold) the strike points of the last closed magnetic surface (LCMS) are located in the corner of the Gas Box divertor, in order to maximise the pumping. Even if an H-mode is triggered, good pumping prevents the build-up of large edge pressure gradients that have been found to prevent the formation of an ITB [5.3].

In JET, steady ITBs are only produced when excessive peaking of the pressure profile is avoided [5.4] which might otherwise lead to disruptive external kink modes or to creation of snakes [5.5]. This is achieved by controlling the plasma edge with impurity injection (argon or krypton) and by adjusting the power waveforms to slowly build-up the plasma pressure. Radiation from injected impurities, in the range of 40% of total radiated power, allows the current profile to be controlled and type I ELMs to be avoided. In this case the q=2 surface slowly increases and large ITBs are produced, allowing good confinement to be achieved. These ITBs being rather wide are very sensitive to the radial energy losses occurring during large ELMs. An example of a high beta steady pulse produced for a magnetic field of 3.4T is shown in Fig.5.1.

Large steady values of the product $H_{89}x\beta_N$ (up to 7.3), have been produced for several confinement times, for OS plasmas at B_t=2.6T as shown in Fig.5.2 [5.6]. $H_{89}x\beta_N$ is the usual reference quality factor for advanced scenarios. A fusion yield of up to 10MW of equivalent DT power is achieved for the pulse shown in Fig.5.1, with confinement and beta significantly exceeding the corresponding values obtained with an ELMy H-mode plasmas produced at similar magnetic field and plasma current [5.6]. Such high performance can be maintained for as long as the power is applied. This time of about 5 to 6s, which corresponds to the maximum technical capability in JET, is only a few times the energy confinement time.

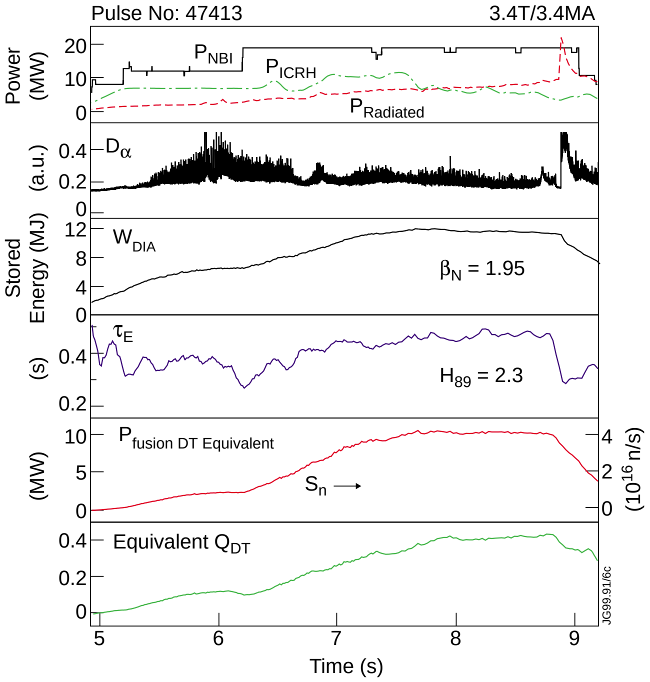

Fig.5.1: Time evolution of typical traces of pulse 47413.

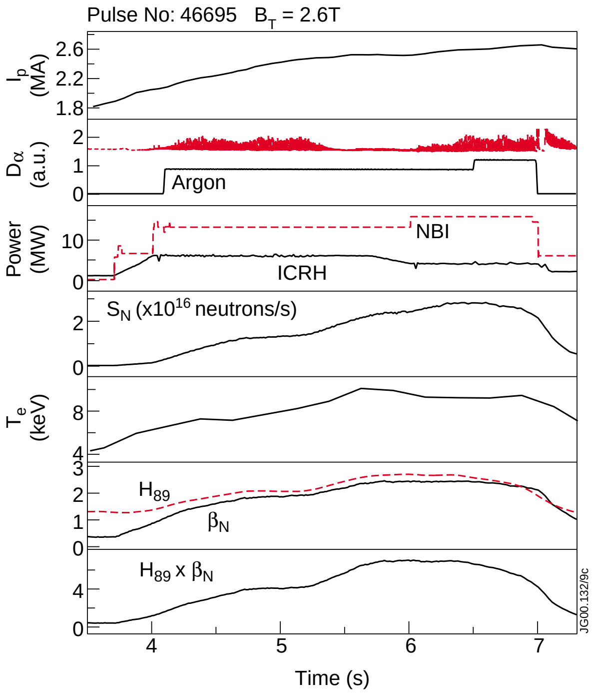

Fig.5.2: Time traces of typical signals for pulse 46695 (2.6T).

It is to be noted that some event, especially at high beta, often interrupts the high performance phase before the end of the additional heating power phase. An example of this can be seen in the pulse shown in Fig.5.1. A small event appears just before the end of additional heating application, which does not corresponds to any MHD activity and induces a neutron rollover. A possible explanation is linked to interaction with the septum part of the Gas Box divertor, which will be discussed in the next sub-section.

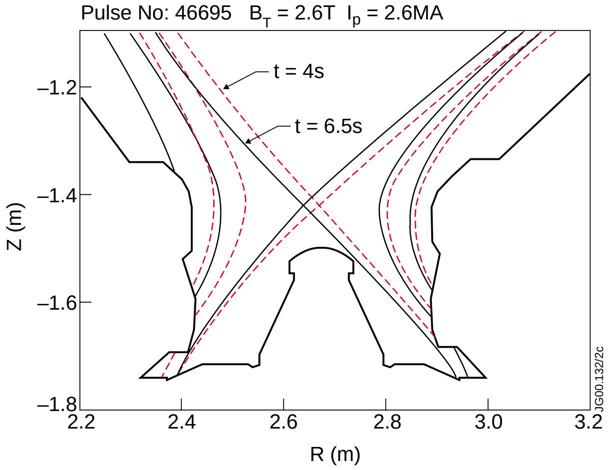

Fig.5.3: Last closed magnetic surfaces for a high normalised beta pulse at B_t=2.6T (pulse 46695) during the low and the high beta phases of the discharges (from EFIT).

Interaction with the septum

As shown in Fig.5.3**,** the last closed magnetic surface for standard optimised shear configurations came very close to the septum when beta increases; some visible light emitted from the septum was often observed in such cases.

In order to possibly assess the effects on the plasma associated with such an interaction, optimised shear plasmas at relatively low betas were produced with the LCMS very close to the septum as shown in Fig.5.4. With such a configuration, large ELMs are triggered about 1 sec after the time where the magnetic surface is set close to the septum, as seen in Fig.5.5**.** An edge density increase is also observed. This is likely to be due to the gas release during the interaction

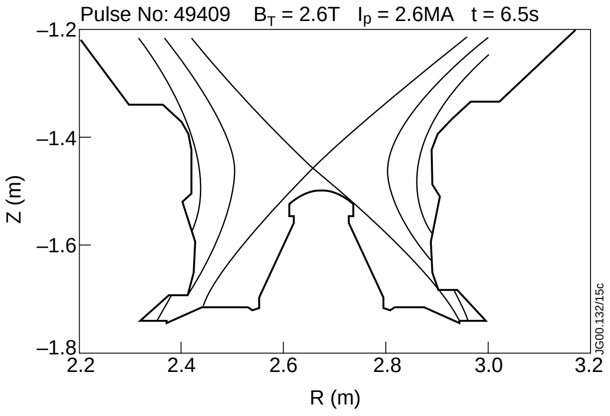

Fig.5.4: Last closed magnetic surface for pulse 49409.

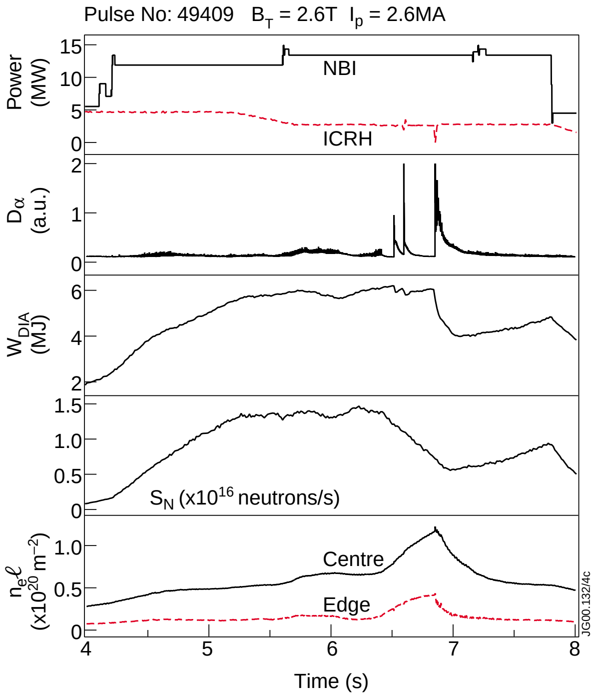

Fig.5.5: Time evolution of typical traces for pulse 49409. The increase in central and edge density is linked to the triggering of type I ELMs.

with the septum, which seems to play a similar role as gas injection in the scrape-off plasma. As a result, the edge conditions are modified, in particular the nature of the ELMs: from very grassy ELMs to large ELMs (which seem like type I ELMs). This might be due from changing edge plasma conditions with high Te and low ne to edge plasmas with low T_e and high n_e [5.7]. In that process Type I ELMs are triggered after a period of type III ELMs. It can be seen from the neutron signal evolution, that the triggering of large ELMs entails the loss of the ITB [5.8].

As an attempt to avoid this interaction, discharges have been developed in which the magnetic configuration has been modified once the ITB was triggered in order to avoid interference with the septum as shown in Fig.5.6. Strike points are moved up on the divertor vertical target plates. The triggering of large ELMs can only be avoided when the clearance to the septum is sufficiently large.

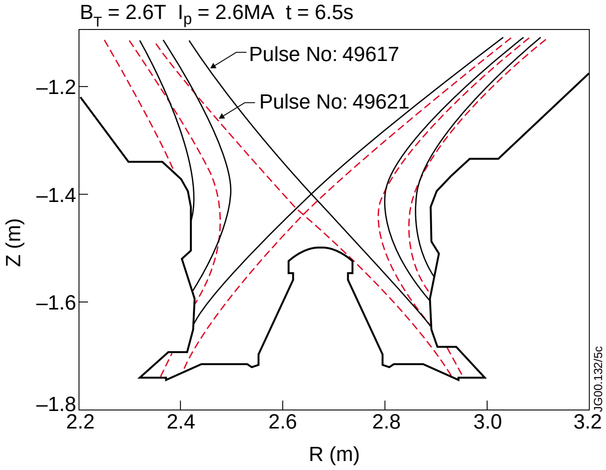

Fig.5.6: Last closed magnetic surfaces for pulses 49617 and 49621.

As a result plasmas with ITBs can be maintained without changes in the edge behaviour, as shown in Fig.5.7. The time evolution of edge plasma density is shown in Fig.5.8 for this series of pulses. In the case of septum interaction, the edge density remains low when the strike points stay in the divertor corner with relatively high pumping speed. But then edge density starts to increase before the triggering of large ELMs.

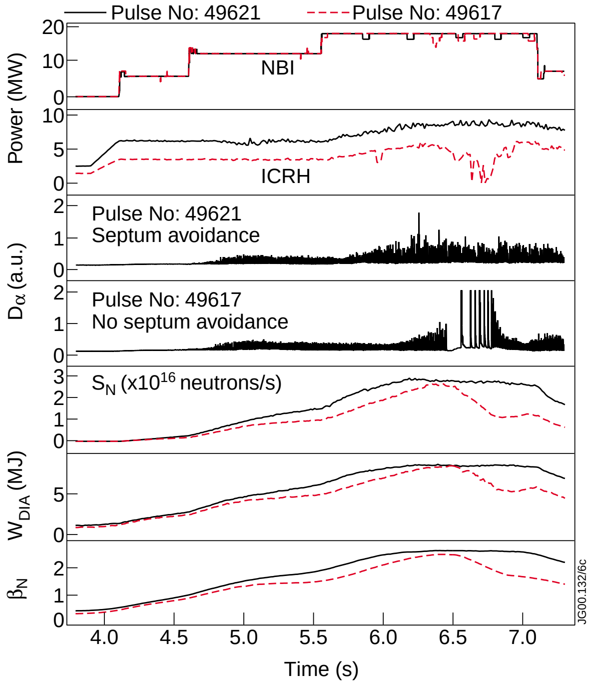

Fig.5.7: Time evolution of typical traces for pulses 49617 and 49621 with and without septum interaction.

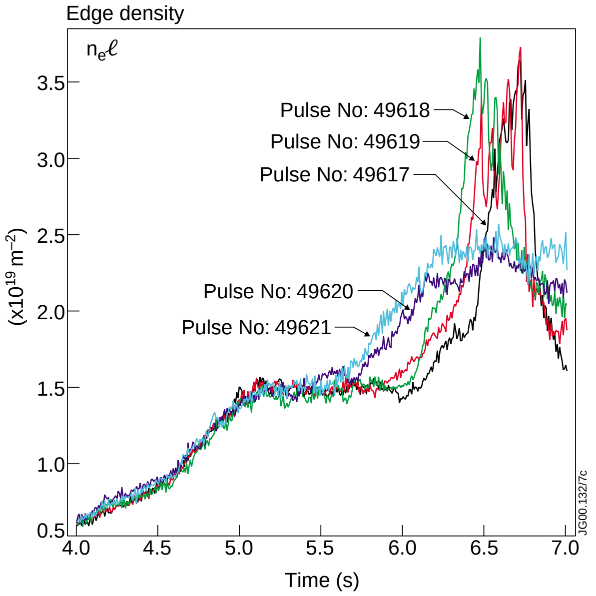

Fig.5.8: Comparison of edge density with and without septum interaction. Signals are integrated along a chord located at R=3.75m.

When the septum is avoided, the edge density increases, probably due to lower pumping, but remains at a steady value allowing ITBs to be maintained. This is confirmed by the time evolution of the ITB as given from the radial profiles of electron temperature (shown in Fig.5.9). The ITBs are rather wide (about r/a~ 0.7) and the electron temperature outside the ITB is quite high. As a result, the pressure gradient in the ITB area tends to weaken. A weakening of the ITB can also be observed at a radius of about 3.5m. This can be linked to tearing modes and will be discussed later.

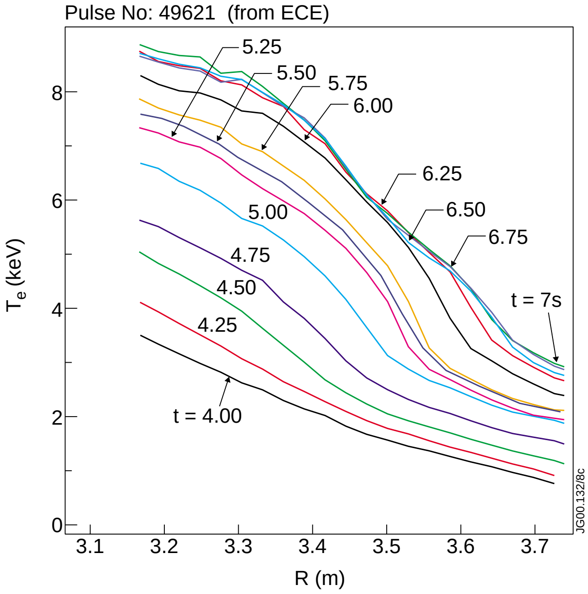

Fig.5.9: Time evolution of radial electron temperature profiles (from ECE data).

So, even though steady ITBs at high beta have been produced in this way, this technique of septum avoidance might not be a long-term solution due to this increase in edge pedestal. A real long-term solution is probably the removal of the septum (as planned for 2001).

High normalised beta data base

Two set of databases have been set-up for optimised shear discharges produced at magnetic field values 2.6 and 3.4T , for which a large number of pulses exist. The database that will be discussed here refers to the dependence of normalised beta with power in an attempt to establish if a limit in normalised beta has been observed. Therefore, selected pulses are of the type shown in Fig.5.1 (3.4T) and in Fig.5.2 (2.6T) (see annexes 1 and 2). The selected pulses are:

- disruption free, i.e. not limited by kink modes,
- do not show snakes,
- have an ITB triggered when a q=2 magnetic surface exists,
- show a steady value of normalised beta,
- total power is maintained more or less constant for about 0.5sec before the steady phase of β_N.

In order to achieve steady ITBs, argon seeding at the edge has been used for most of the pulses in the database. ITBs so produced are wide and the pressure peaking is moderate.

The dependence of normalised beta versus additional power is shown on Fig.5.10. It should be noted that the power required for triggering an ITB at a magnetic field of 2.6T is around 15 MW. Therefore, the achieved normalised beta at this power level might be low due to the closeness to “threshold” conditions, but ITBs have been produced in all pulses of Fig.5.10.

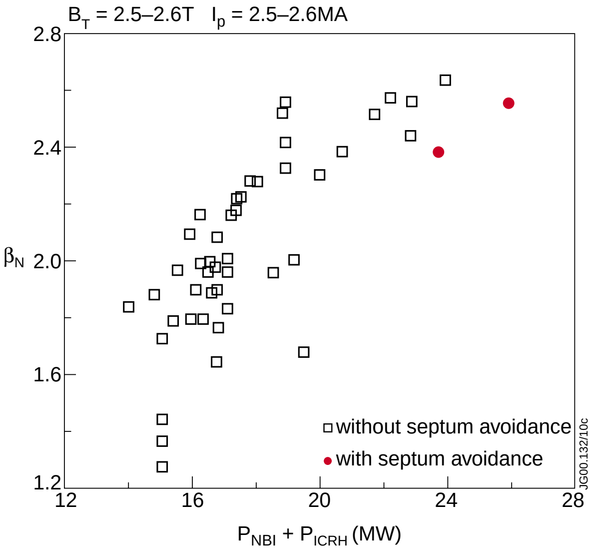

Fig.5.10: Normalised beta versus additional heating power for Bt = 2.6T. Open points correspond to data achieved with septum avoidance technique. Solid points correspond to a set of consecutive pulses with very similar conditions but for septum avoidance.

It is also to be noted that the 46 pulses used for this database were produced with varying conditions, in particular concerning the timing of the high power phase and the shape of the power waveform. This explains a substantial scattering of data for a given power. Since we are interested in assessing a possible beta limit, the envelope of the maximum values of normalised betas should considered for this purpose. A weak saturation is clearly observed. It is also to be noted that the beta normalised achieved with septum avoidance technique discussed in the preceding section, are slightly below the trend of the other data. This is further exemplified in Fig.5.11 were only data achieved with similar conditions (power and argon waveforms, etc…) are plotted. The only difference for these consecutive pulses is the location of the last closed magnetic surface strike points for the pulses with the septum avoidance technique and for the power. In this figure, a saturation of normalised beta is not obvious. Power in excess of the available power for this series of experiments: 18 MW of NBI and 10 MW of ICRH is really necessary to assess the beta limit.

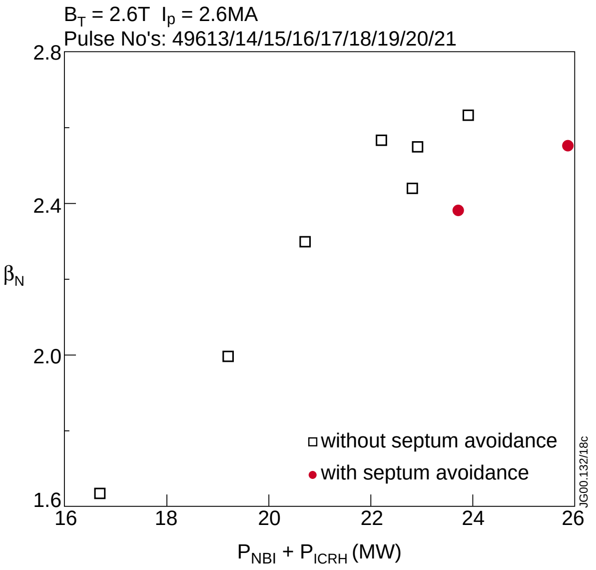

Fig.5.11: Normalised beta versus additional heating power for steady ITBs achieved for similar conditions but for the location of the last closed magnetic surface strike points and for the power. (Pulses 49613 to 49621).

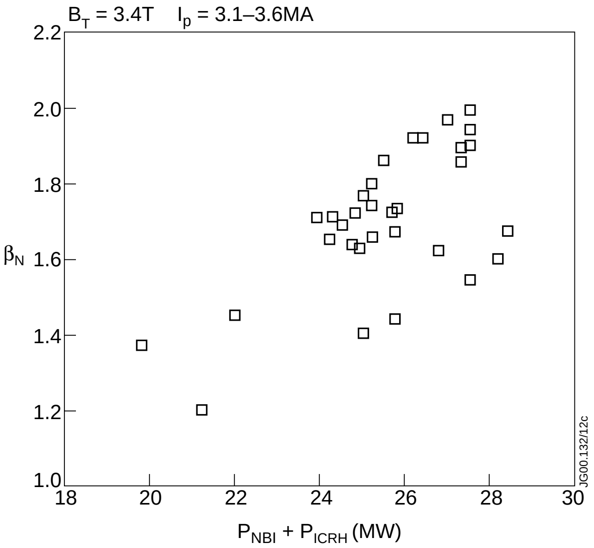

Fig.5.12: Normalised beta versus additional heating power for Bt = 3.4T.

A similar plot of normalised beta versus additional power for a magnetic field of 3.4 T is shown in Fig.5.12. Here also some scatter of the data is observed but there is no clear indication of beta saturation. Available power is clearly not sufficient to assess beta saturation, at least for these scenarios.

Normalised beta saturation and MHD activity

MHD analysis of JET optimised shear discharges has indicated that the pressure profile plays a key role, especially for the external kink modes [5.4] and also for the appearance of snakes [5.5]. In this report, only soft events, such as tearing modes, are present in all pulses used for the normalised beta database.

Typical spectrograms of MHD activity are given in Fig.5.13 for pulses with and without septum avoidance. They show the presence of high n tearing modes, including n=2, 3 and 4 modes with no indication of a precursor in the case of the non-septum avoidance case whose ITB collapses when type I ELMs are triggered. The displacement and the phase of the n=3 mode at about 51 kHz is shown in Fig.5.14. The phase inverts at about 3.38 m indicating an island of about 2 cm width. This mode also couples to another mode near 3.6m with only a 0.5cm displacement. This mode may be the cause of the weakening of the electron ITB, that can be observed in Fig.5.9.

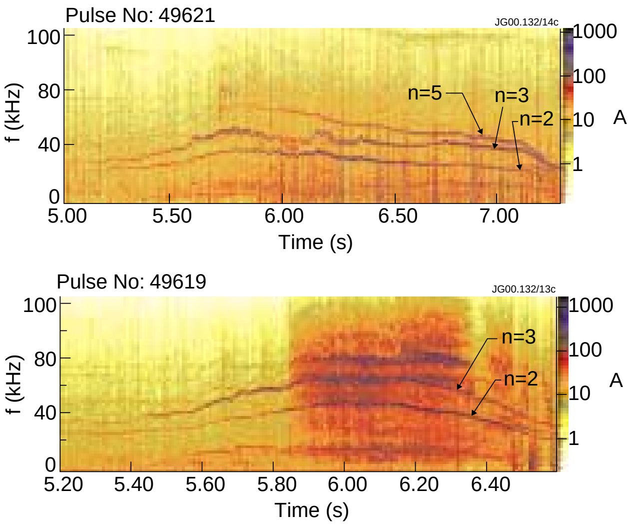

Fig.5.13: MHD spectrograms for pulse 49619 (without septum avoidance) and 49621 with successful septum avoidance.

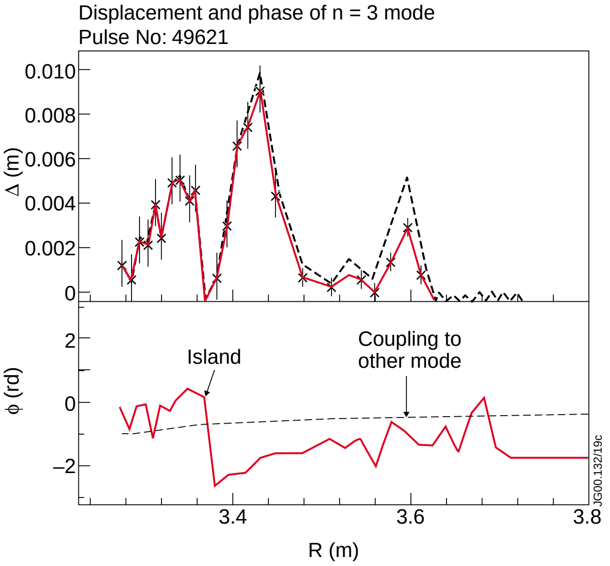

Fig.5.14: Displacement and phase of the n=3 mode for pulse 49621.

Modes with even higher n number have been observed with n up to 8 and frequencies up to 100 kHz. For instance, there is a long-lived n=5 mode throughout the high power phase of the steady high fusion yield pulse 47413 (Fig.5.1). These modes might produce a slight local weakening of the transport barrier but they are no indications that they are causing the neutron rollover.

The neo-classical nature of these modes is debatable. An MHD analysis has been made of pulse 46695 (Fig.5.2) [5.9]. Modes (n=2 and n=6) grow out of the noise without any obvious trigger event, and the n=2 mode amplitude seems to be well correlated with beta. This might point towards a neo-classical nature for this mode. But there is no inversion in phase (from ECE channels) for this n=2 mode, therefore indicating kink mode type behaviour. So, the nature and drive of these modes remains an issue for further study. Irrespective of their origin these modes seems to affect the quality of the ITB and therefore the achievable beta [5.10] (but do not lead to a beta saturation). It will be interesting to develop techniques aimed at avoiding them.

It is interesting to note that an estimate of the MHD stability of the JET optimised shear plasmas, with relevant pressure profiles, has indicated that plasmas with normalised betas up to 2.5 will be stable against external kink modes. This analysis was done assuming some wall stabilisation [5.11]. Achieving higher beta values would require modification of the current profile.

5.3 Summary and future directions

- Steady plasmas with wide ITBs, high confinement and high-normalised beta have been achieved with Optimised shear plasmas by controlling edge conditions and pressure peaking.
- Steady values of the product H89x β_N, which is the usual factor of merit for advanced scenarios, have been obtained up to 7.3 for 2.6T/2.6 MA discharges with an argon seeded edge.
- Interaction with the septum is likely to induce type I ELMs and subsequent collapse of the ITB.
- Septum avoidance techniques have been developed by moving up the strike points on the vertical plates once the ITB is formed, and steady high-normalised beta plasmas have been obtained.
- But these plasmas with raised strike points have a somewhat lower β_N, probably due to too high an edge pressure caused by the lack of pumping. A real long-term solution appears to be the removal of the septum.
- High n MHD modes seem to locally affect the ITB but do not cause a saturation of $\beta_{N.}$. Their neo-classical nature is debatable and should be the subject of further study.
- Total present available power (18MW NBI and 10 MW ICRH) is not sufficient to really assess β_N limits in the presently developed OS scenarios in JET.
- These data, together with data achieved at high β_P, are very encouraging for future developments on JET and for the future of advanced scenarios.

5.4 Shot Lists

Pulse list for 2.5T high beta plasmas

pulse number	Pnbi+Picrh(MW)	betan	neutrons(10x16/sec)
45345	15.400	1.7900	1.4000
45363	16.800	1.9000	1.6000
45369	14.800	1.8800	1.5000
45585	15.900	1.8000	1.4000
45593	14.000	1.8400	1.4000
45847	15.000	1.7300	1.6000
45867	18.500	1.9600	1.4800
45870	19.500	1.6800	1.2000
45885	17.200	2.1600	1.6400
45886	16.600	2.0000	1.4000
45887	18.000	2.2800	1.8000
45888	17.300	2.2200	1.7800
45898	17.800	2.2800	1.8000
45926	15.500	1.9700	1.6000
46123	16.200	2.1600	1.9800
46124	16.900	1.9800	1.8000
46124	16.600	1.8900	1.8000
46695	18.800	2.5200	2.9000
46701	18.900	2.5500	2.7000
46703	20.000	2.3000	2.1600
46708	21.700	2.5100	2.7200
47007	18.900	2.3200	2.3500
47939	15.000	1.4500	0.80000
47942	15.000	1.3700	0.80000
48231	15.000	1.2800	0.43000
49404	17.100	1.9700	1.8000
49406	17.100	2.0100	1.7400
49408	17.100	1.8300	1.5500
49617	22.800	2.4400	2.5200
49620	23.700	2.3800	2.4500
49621	25.900	2.5500	2.7000
46125	16.800	2.0800	1.9000
46125	16.800	1.7600	1.5000
46290	16.300	1.8000	1.3000
46410	15.900	2.0900	1.7000
46415	16.500	1.9700	1.6000
46416	16.100	1.9000	1.2000
46437	16.200	1.9900	1.6000
46693	17.300	2.1800	1.9000
46694	17.500	2.2200	2.0000

pulse number	Pnbi+Picrh(MW)	betan	neutrons(10x16/sec)
47022	18.900	2.4200	3.0000
49613	16.700	1.6400	1.1800
49614	19.200	2.0000	2.0000
49615	20.700	2.3800	2.5000
49616	22.200	2.5700	2.8000
49618	22.900	2.5500	2.8000
49619	23.900	2.6300	2.9000

Pulse list for 3.4T high beta plasmas

pulse number	Pnbi+Picrh(MW)	betan	neutrons(10x16/sec)
46374	27.500	1.5400	3.1000
46376	25.800	1.4400	2.5000
46381	26.800	1.6200	3.5000
46464	26.400	1.9200	4.3000
47210	24.800	1.6400	2.7000
47213	25.000	1.7600	3.0000
47214	24.200	1.6500	2.7000
47215	23.900	1.7100	2.7500
47219	24.800	1.7200	2.8000
47221	24.900	1.6300	2.8000
47351	25.200	1.6600	3.4000
47352	27.300	1.8900	3.9000
47357	27.300	1.8600	3.7000
47360	27.500	1.9300	4.2000
47401	25.000	1.4000	2.5000
47402	27.500	1.9000	3.8000
47403	25.200	1.7500	3.8000
47405	25.800	1.6800	3.3000
47410	25.800	1.7300	3.4000
47413	26.200	1.9200	4.1000
47414	27.000	1.9700	4.1000
47417	28.400	1.6800	3.0000
47418	28.200	1.6000	2.8000
47420	25.700	1.7200	3.5000
47424	25.500	1.8600	4.0000
47426	27.500	1.9900	4.2000
47450	24.500	1.6900	3.5000
47451	24.300	1.7100	4.0000
47457	22.000	1.4500	2.6000
47465	25.200	1.8000	3.3000
47411	21.200	1.2000	1.4000
46637	19.800	1.3700	2.5000

References

[5.1] Sips AAC et al, Plasma Phys. Control. Fusion 40 (1998) 1171

[5.2] Challis C. et al, in Controlled Fusion and Plasma Phys. (Proc. 26th Eur. Conf, Maastricht 1999) vol 23J, European Physical Society, Geneva, (1999) p 69

[5.3] JET Team (C Gormezano), Nuclear Fusion, Vol.39, No. 11Y (1999) 1875

[5.4] Hender T. et al, Proc.26th EPS Conf. On Controlled Fusion and Plasma Physics (Maastricht, 1999) vol. 23A(Geneva: EPS)

[5.5] Alper B. et al, Proc.26th EPS Conf. On Controlled Fusion and Plasma Physics (Maastricht, 1999) vol. 23A(Geneva: EPS)

[5.6] Gormezano C, Plasma Phys. Control. Fusion 41 (1999) B 367

[5.7] Sartori R et al, to be presented at EPS Budapest

[5.8] Sarrazin Y et al, to be presented at EPS Budapest

[5.9] Maraschek M., private communication

[5.10] Baranov Yu. et al. Nucl. Fusion 39 (1999) 1463

[5.11] Bondeson A. et al, Nucl. Fusion 39 (1999) 1523

6. HIGH B$_P$ STUDIES

C D Challis[1], B Alper[1], Yu F Baranov[1] and T C Hender[1]

JET Joint Undertaking, Abingdon, Oxon., OX14 3EA, UK.
[1] EURATOM/UKAEA Fusion Association, Culham Science Centre, Abingdon, Oxon., OX14 3DB, UK.

6.1 Overview

The study of internal transport barriers in the high β_P domain is directly relevant to the assessment of the potential reactor relevance of plasma scenarios with improved core confinement. High values of β_P are required to generate a substantial neoclassical bootstrap current, which is required in the currently envisaged steady state tokamak reactor concepts, and so the study of ITB dynamics in this regime is of great importance. In this work the JET Optimised Shear domain has been extended to high values of β_P (up to 1.6) in an attempt to observe the effect on confinement and stability. The bootstrap current has been estimated to provide about one third of the total plasma current in roughly steady conditions at $\beta_P \approx 1.4$ with the neutral beam driven current contributing a further quarter. The fraction of the plasma current provided non-inductively was therefore about 0.6, which is lower than expected due to the large fast ion component contained within the total plasma stored energy. Nevertheless, the non-inductive current profile has a similar shape to that of the total current, which is encouraging for the prospects of good bootstrap current alignment for the combination of a broad ITB and a monotonic q-profile. The confinement improvement over L-mode (H factor) and overall stability (β_N) are not yet of the standard required for a truly 'Advanced' tokamak regime and there are signs that the achievable β_P in reactor relevant conditions may be limited by stability rather than confinement in these experiments. The preliminary investigations reported here provide substantial scope for future development and optimisation, which should be focussed on the demonstration of the reactor compatibility of the JET Optimised Shear regime.

6.2 Results

Background

A steady state tokamak reactor will require the plasma current to be provided non-inductively using externally driven mechanisms such as the injection of radio frequency waves or neutral beams as well as the plasma pressure driven neoclassical bootstrap current. The optimisation of the bootstrap current is beneficial as it can minimise the requirement on external drive systems that contribute to the recirculating power of the reactor as a whole. This optimisation has two main considerations: the total bootstrap current must represent a substantial fraction of the plasma current required by a reactor; but the bootstrap current profile must, at the same time, be well matched to the overall current profile so that no additional counter current drive is necessary to maintain the desired profile shape. These considerations can be used in the assessment of candidate plasma regimes being developed for steady state application, in addition to the requirements on confinement and stability, which affect the economic feasibility of such a reactor device.

The provision of a large fraction of the plasma current using the bootstrap mechanism required the achievement of high β_P since the bootstrap current fraction if roughly given by [6.1] as:

$$\frac{I_{bootstrap}}{I_{plasma}} \approx A\sqrt{\varepsilon}\beta_P$$

where ε is the inverse aspect ratio and A is typically about two thirds and depends mainly on the plasma profiles. For JET and ITER-FEAT the aspect ratio is of order 3 and so 75% of the plasma current can be provided by the bootstrap current at $\beta_P \approx 2$. This leads to a simultaneous requirement on plasma stability through β_N for the same plasma aspect ratio as follows:

$$\beta_N \approx \frac{C\beta_P}{q_{95}}$$

where C depends mainly on the plasma shape and is typically 9-10 for the cases being discussed here. The fusion yield of a tokamak is maximised at low q_{95} for a given toroidal magnetic field strength and β_N. This leads to the requirement for a compromise between the highest achievable β_N and the largest acceptable q_{95}. Additionally, the operation at intermediate q_{95}, and plasma current, which may result from such a compromise, provides a further requirement on plasma confinement in the form of a large H factor. High values of these three parameters: β_P; β_N and H factor, must be achieved simultaneously together with good bootstrap current alignment for a regime to be directly applicable to a steady state tokamak reactor.

The experiments described in this section were designed to investigate the potential for the JET Optimised Shear regime to meet these objectives. A single day of operation, with 12 good plasma pulses, was devoted to this study and so the results only represent a superficial assessment, and the process of optimising the scenario is very far from complete. However, these initial experiments give some indication of the progress that has been made towards a self-consistent reactor regime and also highlights the areas where further progress is required.

Method

In order to achieve high β_P with the heating power available on JET it is necessary to operate at modest plasma current. This results from the dependence:

$$\beta_P \propto I_P^{-1}$$

at a given heating power level and assuming the plasma confinement is proportional to the plasma current. To provide the compromise between the low q_{95} and high β_N requirements described above, the plasma current and toroidal magnetic field were chosen to be 1.5MA and 2.6T respectively giving $q_{95} \approx 6$ and $\beta_N \approx 1.6\beta_P$.

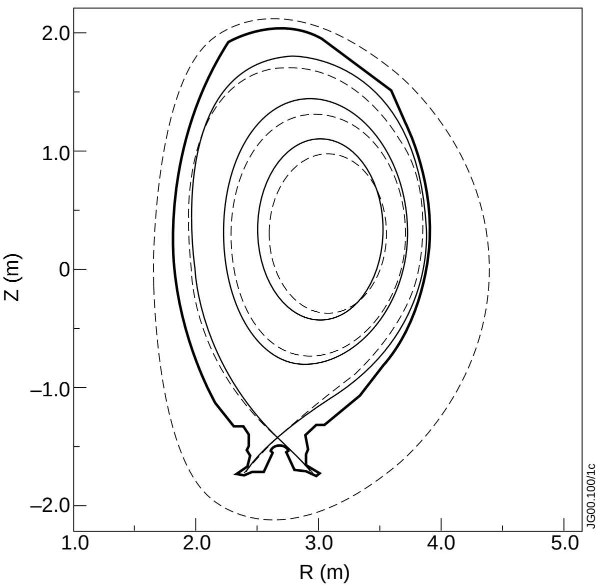

Fig.6.1: Comparison of the flux surface equilibrium at 5.5s for a standard Optimised Shear plasma (#49783 – solid lines) with $\beta_P = 0.75$ and a high β_P plasma (#49794 - broken lines) with $\beta_P = 1.6$.

Two operational difficulties arise from the attempt to access the JET Optimised Shear regime at these plasma parameters. The first concerns the requirement that the X-point configuration in the proximity of the divertor septum be maintained against the natural shape change of the plasma at high β_P. This was achieved by careful tuning of the feed-forward waveforms for the divertor coil currents. The X-point and divertor configuration was maintained close to the conditions typical of other Optimised Shear experiments (see Fig.6.1) and gross interaction with the divertor septum was avoided at values of $\beta_{P,DIA}$ up to 1.6. However, further development of the configuration to avoid the septum interaction altogether was not attempted and the possibility that this plays a role in the performance limitations of these experiments cannot be discounted. Further discussion on this point is provided in section 5 on the high β_N studies.

The second difficulty concerns the H-mode behaviour and, in particular, the interaction of ELMs with the Internal Transport Barriers (ITBs), which are produced in the optimised Shear regime. It has been observed on JET that large type I ELMs can destroy ITBs by eroding the high confinement region. The power levels required for the production of an ITB is typically several times larger than the H-mode power threshold and, consequently, well into the region where type I ELMs are seen in conventional ELMy H-mode plasmas. These large ELMs are avoided in transient Optimised Shear experiments by the use of a positive current ramp, which acts to increase the H-mode power threshold. The use of low plasma current in these high β_P studies results in the main heating pulse being applied during the current flat-top phase. Earlier heating in the current ramp phase would precede the arrival of the q=2 magnetic surface in the plasma which is thought to be beneficial for ITB formation in the plasma core. For pulses where the main heating pulse persists into the current flat-top an argon seeding technique has been developed to prevent the emergence of large ELMs. Figure 6.2 shows the comparison of a standard Optimised Shear pulse with a continuous current ramp and argon seeding, where type III ELMs are maintained and an ITB produced, and two high β_P pulses with current flat-top heating and similar argon seeding rates. The performance of the current flat-top pulses is much poorer than the conventional scenario despite the similar conditions at the start of the main heating pulse. The target q-profile is almost unaltered in the plasma interior by the change in current waveform as the main heating pulse starts soon after the point where the current waveforms diverge and

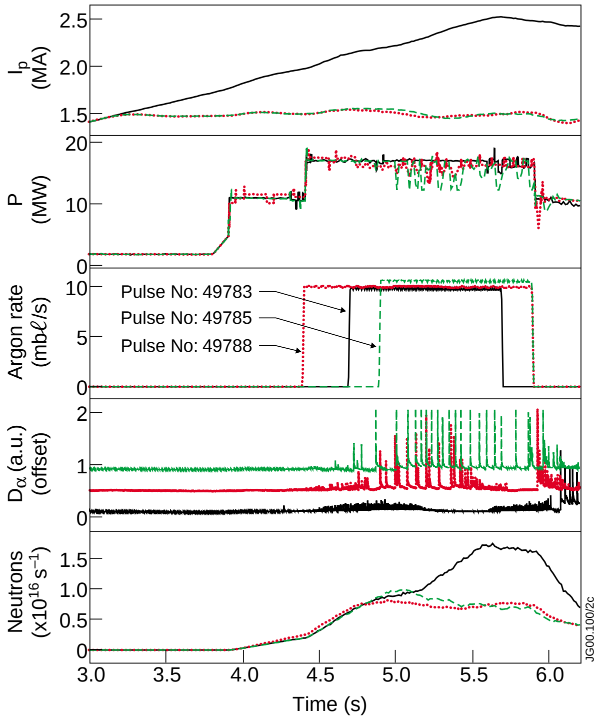

Fig.6.2: Time evolution of similar Optimised Shear pulses with (#49783 – solid lines) and without (#49788 – dotted lines and #49785 – dashed lines) current ramp during main heating. During the current flat-top large ELMs are generated, despite the argon seeding, which inhibit the formation of a strong ITB as evidenced by the neutron yield.

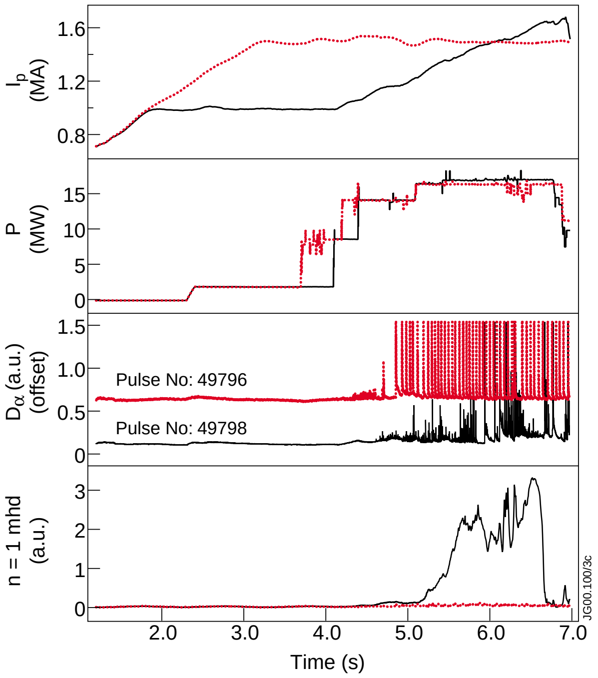

Fig.6.3: Time evolution of similar pulses with a two stage current ramp (#49798 – solid lines) and a single stage current ramp (#49796 – dashed lines) showing the reduction in ELM amplitude during a second current ramp phase.

‘freezes’ the core current profile. The difference in performance is attributed to the large ELMs in the current flat-top case which inhibits the formation of a strong ITB.

An alternative current waveform was developed to avoid the occurrence of large ELMs during the main heating phase by delaying the final current ramp as shown in Fig.6.3. This technique was partially successful in the suppression of the large ELMs, but the current ramp waveform had necessarily diverged from the conventional case much earlier allowing a different evolution of q in the plasma core. In the delayed current ramp case shown in Fig.6.3 a large n=1 island appeared during the main heating phase, which is believed to inhibit the formation of ITBs [6.2]. No further optimisation of this regime

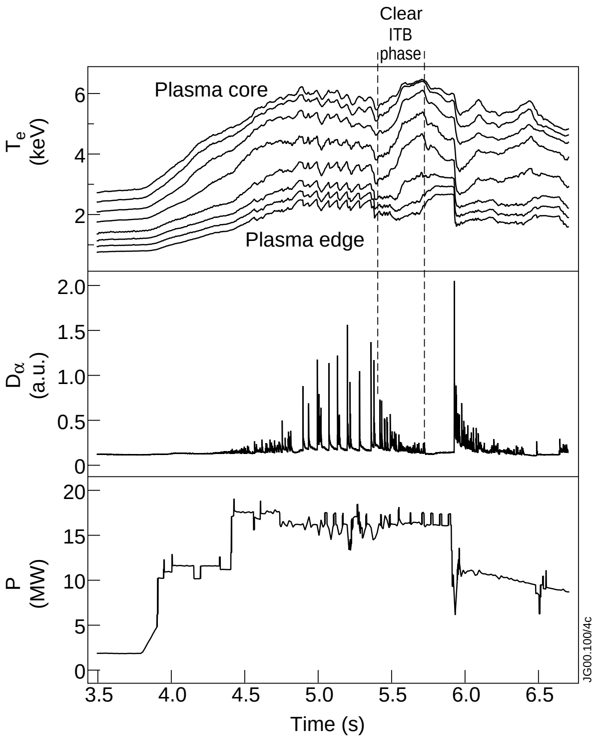

Fig.6.4: Time evolution of a high β_P plasma (#49788) where a clear ITB emerges, as evidenced by the steep gradients in the electron temperature measured using a heterodyne radiometer, during the phase indicated where type III ELMs are observed.

was attempted, but modification of the target q-profile would be required (e.g. by varying the timing of the main heating pulse) to avoid the growth of the island in the plasma core.

Despite these difficulties ITBs were produced during the current flat-top heating pulse. Figure 6.4 shows a case where large type I ELMs are initially produced, but then a back transition to type III ELMs is observed at which time a clear ITB emerges. This ELM behaviour is reminiscent of observations reported in the conventional ELMy H-mode regime without the presence of current ramps, argon seeding or ITBs [6.3]. These spontaneous phases of type III ELMs were sufficiently common as to allow a study of ITBs in the high β_P conditions, but further development would be required to provide the quiescent conditions desirable for a more thorough investigation of this domain.

ITBs in high β_P plasmas

It should firstly be noted that ITBs were achieved in plasmas with high β_P. An example of the evolution of an ITB under these conditions is illustrated by the electron temperature profiles shown in Fig.6.5. In this case the $\beta_{P,DIA}$ was about 1.3 during the ITB phase. Whilst this is by no means the first such observation in a tokamak experiment (see [6.4] for example), there has been some interest in the role of β_P and the Shafranov shift in the mechanisms responsible for ITB production. Experiments such as these may provide a useful contribution to such investigations.

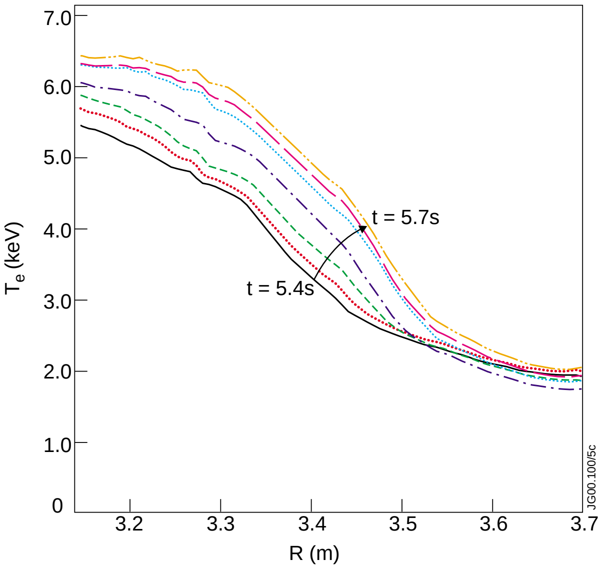

Fig.6.5: Electron temperature profiles, measured using a heterodyne radiometer, illustrating the evolution of the ITB during the type III ELM phase indicated in Fig.6.4 (5.4-5.7s) for #49788.

Figure 6.6 shows the peak values of $\beta_{P,DIA}$ and $\beta_{N,DIA}$ that were achieved in these experiments as a function of additional heating power. There is no sign of a saturation of performance with heating power up to the maximum level used of 20MW. It can be seen that the highest β_P value achieved of 1.6 corresponds to a β_N of 2.6. Figure 6.7 compares the peak $\beta_{N,DIA}$ with the value after 1.5s of main heating. This illustrates the difficulty in maintaining the highest values of β_N in steady conditions and that a roll-over in performance is encountered in the region of $\beta_{N,DIA} \approx 2.5$. This observation suggests that the experiments performed may have approached a β-limit at the highest applied power level and this may, in practice, limit the achievable value of β_P.

Figure 6.8 shows the time evolution of a pulse during which such a roll-over in performance is observed. It can be seen that the neutron yield peaks at 5s and then falls back to a steady value, which is maintained until the power step-down nearly 2s later. The ITB, seen from the strong

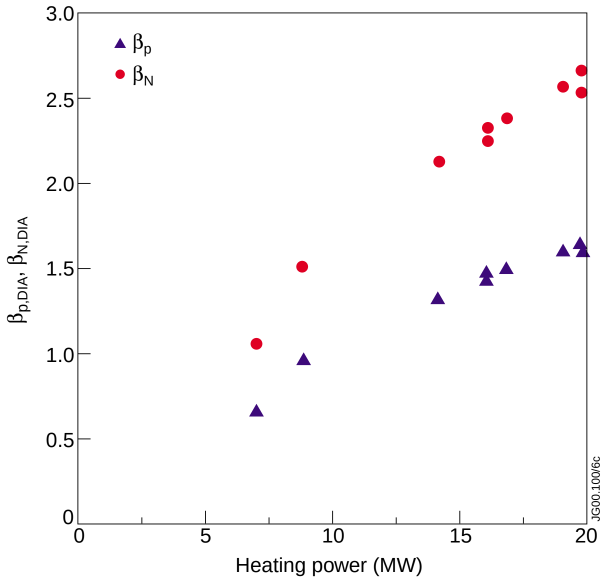

Fig.6.6: Peak $\beta_{P,DIA}$ and $\beta_{N,DIA}$ plotted against heating power for the high β_P experiments showing a continuous rise in plasma performance up to the 20MW power level.

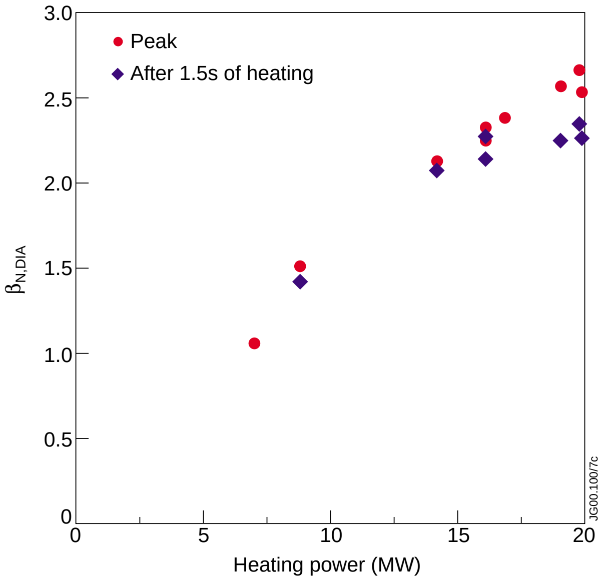

Fig.6.7: Comparison of the peak value of $\beta_{N,DIA}$, plotted against heating power, with the value 1.5s after the start of the main heating pulse suggesting a possible performance saturation at $\beta_{N,DIA} \approx 2.5$.

gradients in the temperature profiles, is not lost at the roll-over and, although it is disturbed by the ELM free phase and subsequent large ELM at 5.8-6.0s, it persists throughout the main heating phase. It should be noted that the value of the ion temperature shown in Fig.6.8 has been calculated from charge-exchange recombination spectroscopy using a multi-component Gaussian fit technique which is known to overestimate the temperature in the presence of argon in the plasma (see section 13). The cause of this roll-over in plasma performance has not been identified. n=2 mhd activity is sometimes observed during the high β_N phase of these discharges, but no causal link with the roll-over has been established. In some cases changes in the ELM activity appears to coincide with this event and interaction between the plasma and the divertor septum might play a role in altering the edge plasma conditions at these high values of β_P. The confinement enhancement factor with respect to the ITER89L-P scaling [6.5] is shown in Fig.6.9 for the pulse illustrated in Fig.6.8, together with the time evolution of β_P and β_N. At the roll-over point H_{89} reaches 2.5 and $H_{89}\beta_{N,DIA}$ peaks at about 6. However, during the steady phase with type III ELMs (6.0-6.8s) H_{89} settles to a value just above 2 with $H_{89}\beta_{N,DIA} \approx 5$.

Higher values of both of these parameters would be required for an economic reactor scenario. A technique, which has been found to be effective for increasing the achievable β_N in the JET Optimised Shear experiments, is the use of a wider ITB. This provides a broader pressure profile, which is stable at a higher value of plasma stored energy [6.6]. High β_P plasmas in these experiments with peaked pressure profiles, such as the pulse shown in Fig.6.4, encounter an n=1 mhd mode, and consequent collapse in the pressure gradient localised in the ITB region, which is thought to be pressure driven. This observation is consistent with the common occurrence of pressure driven n=1 global kink mode disruptions in conventional high performance Optimised

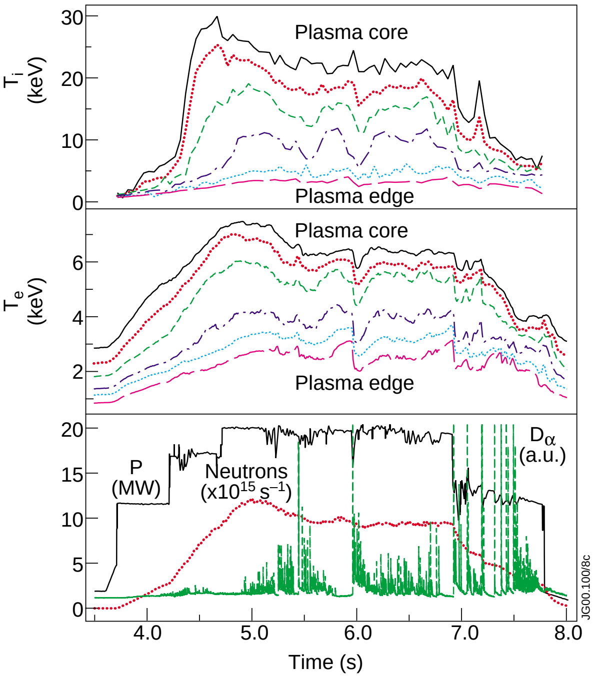

Fig.6.8: Time evolution of a high β_P plasma (#49793) where the ITB persists throughout the main heating phase illustrated by the steep gradients in ion temperature profile measured by charge-exchange recombination spectroscopy and electron temperature measure using a heterodyne radiometer

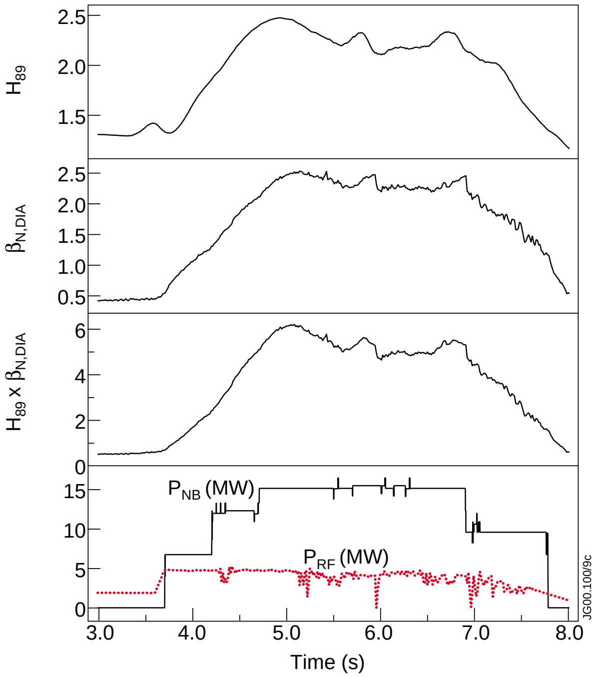

Fig.6.9: Time evolution of the plasma confinement enhancement factor (H_{89}) and $\beta_{N,DIA}$ for the pulse illustrated in Fig.6.8 (#49793).

Shear pulses with narrow ITBs. The soft roll-over encountered at $\beta_{N,DIA} \approx 2.5$ in these high β_P experiments is observed in cases where broader pressure profiles are produced. However, the production of ITBs at much wider radius has been achieved in other Optimised Shear experiments at JET and no attempt has yet been made to optimise the high β_P regime in this regard.

Non-inductive current drive

The non-inductive contribution to the plasma current in these high β_P pulses has been estimated using the TRANSP transport simulation code [6.7]. Figure 6.10 shows the calculated beam driven and neoclassical bootstrap current for the pulse shown in Fig.6.8. The bootstrap current is calculated to be about 35% of the plasma current while the beam driven mechanism calculation gives a further 25%. This estimation yields a total non-inductive component in the region of 60% of the total plasma current. The bootstrap current is only calculated for the thermal component of the plasma pressure since the contribution

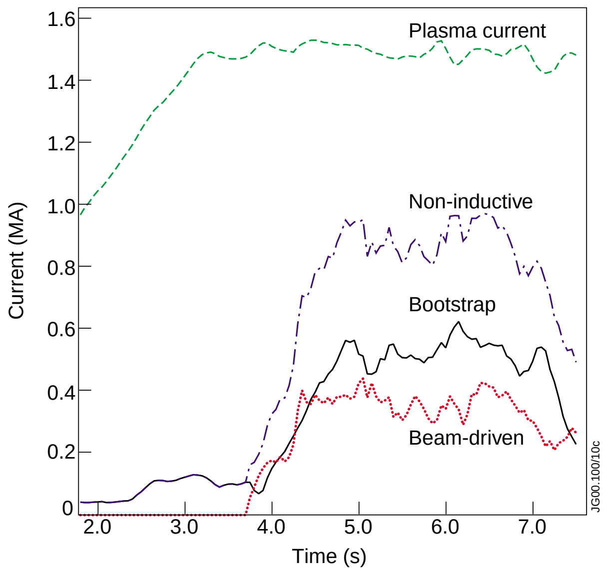

Fig.6.10: Beam driven and neoclassical bootstrap current calculated using TRANSP for a high β_P plasma (#49793) indicating that 60% of the plasma current was provided non-inductively.

of the fast ion pressure is not thought to be large. The fast particle population is calculated to contribute about one third of the total plasma stored energy during the high performance phase of this discharge. This explains the rather low value of the bootstrap current calculated compared with the evaluation of the simple bootstrap current fraction expression above using $\beta_{P,DIA}$.

The TRANSP simulation shown in Fig.6.10 was made using the ion temperature produced using the multi-component Gaussian fit technique and, consistent with the overestimation expected by this method, the simulated neutron yield and plasma stored energy are higher than the equivalent measured values. To estimate the effect of the uncertainty in the ion temperature measurement on the current drive calculation a second TRANSP simulation was made using an ion temperature profile which had been artificially scaled by a factor 0.75 in the plasma interior during the main heating phase. In this case the calculated neutron yield and plasma stored energy were brought into much better agreement with the measure values. The comparison of the calculated non-inductive currents in these two simulations is shown in Fig.6.11. It can be seen that the bootstrap current is reduced slightly in the case where the ion temperature has been reduced, but the reduction is less than 10% and is within the other uncertainties concerned with the bootstrap current calculation. The overall non-inductive current is close to 60% of the plasma current in both simulations, which demonstrates that the calculation of this quantity is relatively insensitive to the uncertainty in the ion temperature measurement. Other simulated quantities, such as the plasma surface voltage, are reasonably well matched and indicate that the simulation is a credible one.

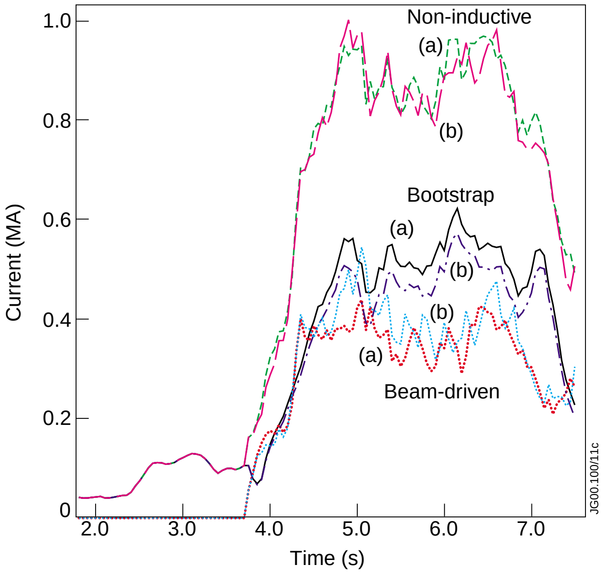

Fig.6.11: Comparison of non-inductive currents calculated by TRANSP for #49793 using the standard ion temperature profile analysis (a) and an artificially reduced ion temperature (b) showing the relative insensitivity of the total non-inductive current drive to uncertainties in the ion temperature measurement.

Typical current profiles from the TRANSP simulation are shown in Fig.6.12. The total non-inductive current profile is similar in shape to the total current profile. To illustrate the good alignment the calculated non-inductive current profile has also been artificially scaled up in magnitude to represent a ‘fully non-inductive’ plasma with the same non-inductive current profile shape. This case of good non-inductive current alignment with the overall current profile is one of the requirements discussed above for a practical steady state reactor scenario. It should be noted that the electron temperature and density profiles in this simulation have been provided by the LIDAR Thomson scattering system and have a spatial resolution of about 12cm. This effectively smoothes the pressure profiles and consequently broadens the calculated bootstrap current profile slightly. Nevertheless, the relatively good alignment shown in the simulation illustrates the compatibility of relatively broad ITBs, such as can be produced in the JET Optimised Shear regime, with the overall current profile. The q-profile in this case is monotonic, which gives good bootstrap current alignment more naturally than scenarios that rely on a region of negative magnetic shear for the production of an ITB. The q-profile determined using EFIT magnetic equilibrium reconstruction [6.8, 6.9] constrained by data from the motional Stark effect (MSE) diagnostic (see section 14) was used to initialise this TRANSP simulation at the start of the main heating pulse. The initial q-profile and the simulated evolution during the first 2 seconds of main heating (4.4-6.4s) are illustrated in Fig.6.13.

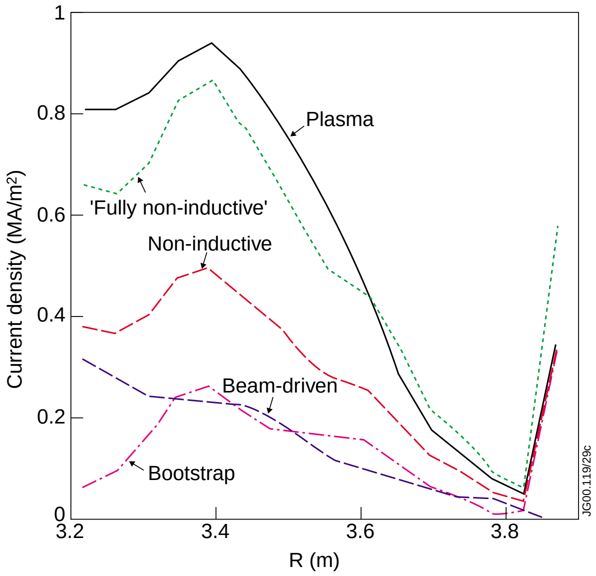

Fig.6.12: Current profiles for a high β_P plasma (#49793 at 6.4s) calculated by TRANSP showing relatively good alignment between the non-inductive current and the total plasma current. The non-inductive current profile has also been scaled up artificially to represent a 'fully non-inductive' plasma with the same non-inductive current profile shape.

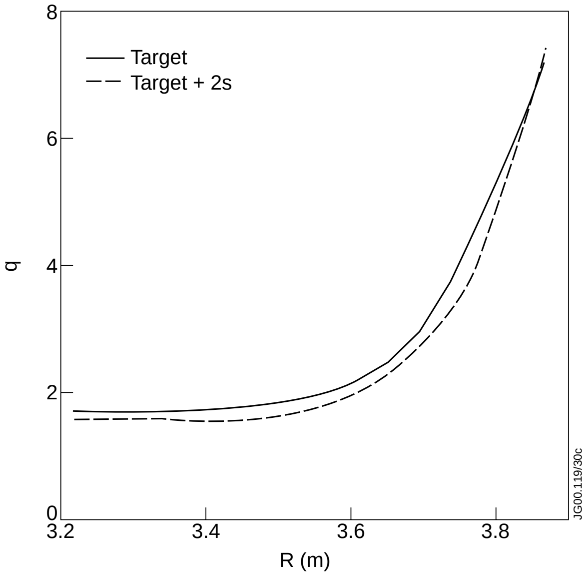

Fig.6.13: Comparison of q-profile for a high β_P plasma (#49793) determined from EFIT equilibrium reconstruction constrained using MSE diagnostic data (at 4.4s) and the evolution during the next 2 seconds simulated using TRANSP.

6.3 Summary and future directions

The extension of tokamak regimes capable of producing improved internal confinement to the domain of interest for currently envisaged 'Advanced' reactors (high β_P, β_N and H) is a necessary part of the process of validation for potential steady state reactor concepts. These initial attempts to perform this exercise for the JET Optimised Shear scenario have been very useful providing encouragement for the prospects of good non-inductive current profile alignment for broad ITBs produced with monotonic q-profiles. The overall performance in terms of the three key parameters listed above is not yet adequate for a truly 'Advanced' scenario. Nevertheless, the results reported here were achieved in very few plasma pulses and much further development and optimisation may be possible. In particular, broader ITBs than those produced in these experiments have already been demonstrated in other JET Optimised Shear experiments [6.10] and could be exploited in this domain with the aim of increasing the achievable β_N and hence β_P. It should be noted, however, that the interaction of the plasma with the divertor septum is more difficult to avoid at high β_P and represents an important issue for the future development of this scenario in the present JET configuration. The prospects for increased plasma density should also be investigated to reduce the fraction of the plasma stored energy contributed by the fast particle population. It would also be desirable to further extend the high β_P Optimised Shear domain to a wider variety of q-profiles, including those with reversed central magnetic shear. In the experiments described in this report steady conditions were not achieved and, in particular, the production of large ELMs, which can be destructive to the ITB, was not entirely avoided. The interplay between the plasma edge and the transport in the plasma interior will be an important consideration in the development of stationary tokamak scenarios and the establishment of steady edge plasma conditions must remain a high priority in the further development of this regime.

6.4 Shot List

The overall pulse range for this investigation was #49781 to #49802. All experiments were performed at 2.6T and employed argon seeding. The pulses of particular interest during this study are listed below:

shot no.	flat-top I_P (MA)	max. P (MW)	max. $\beta_{P,DIA}$	Comment
49782	2.5	17	0.65	Test of conventional current ramp scenario with plasma centroid position control for reference (cf. #49613). Very little sign of an ITB.
49783	2.5	17	0.8	Heating start time advanced by 200ms. Good ITB, but some suggestion of septum contact?
49784	1.5	17	1.35	Septum avoidance tuning with reduced plasma current for high β_P.
49785	1.5	17	1.45	Further septum avoidance tuning. Disruption after main heating pulse.
48786	1.5	17	1.3	Further septum avoidance tuning. Disruption after main heating pulse (followed by a recovery pulse).
49788	1.5	17	1.4	Further septum avoidance tuning.
49789	1.5	17	1.45	Main heating pulse advanced by 200ms. Disruption after main heating pulse (followed by a recovery pulse).
49791	1.5	19	1.6	Higher heating power and longer heating phase. Disruption at the end of main heating pulse (followed by a recovery pulse).
49793	1.5	20	1.6	Further tuning of X-point configuration. Disruption after main heating pulse.

shot no.	flat-top I_P (MA)	max. P (MW)	max. $\beta_{P,DIA}$	Comment
49794	1.5	20	1.6	Further tuning of X-point configuration. Disruption during main heating pulse (followed by a recovery pulse).
49796	1.5	16	1.3	Reduced heating power. Disruption in current ramp down phase.
49797	1.0/1.7	9	1.1	Modified current waveform with 1MA flat-top followed by second ramp phase. NBI tripped on low density interlock.
49798	1.0/1.7	17	1.35	Main heating delayed by 200ms with shorter NBI preheat. Large n=1 mode observed during main heating. Disruption during main heating pulse.

Acknowledgements

It is a pleasure to recognise the contribution of the JET Team to the execution and analysis of these experiments through the operation of the JET systems and the validation of data. The authors also gratefully acknowledge the remote participation of colleagues at Max-Planck-Institut für Plasmaphysik, EURATOM Association, D-85740 Garching, Germany (A C C Sips, R Neu, A Staebler and W Suttrop) who contributed particularly in the optimisation of the plasma configuration in the divertor region.

References

[6.1] J G Cordey, C D Challis and P M Stubberfield, Plasma Phys Contr Fusion **30** (1988) 1625.

[6.2] C D Challis, et al., 26th EPS Conf on Contr Fusion and Plasma Physics, Maastricht 1999, ECA Vol 23J (1999) 69.

[6.3] R Sartori, et al., 26th EPS Conf on Contr Fusion and Plasma Physics, Maastricht 1999, ECA Vol 23J (1999) 197.

[6.4] Y Kiode, et al., Phys Rev Lett **72** (1994) 3662.

[6.5] P N Yushmanov, et al., Nucl Fusion **30** (1990) 1999.

[6.6] T C Hender, et al., 26th EPS Conf on Contr Fusion and Plasma Physics, Maastricht 1999, ECA Vol 23J (1999) 89.

[6.7] R J Goldston, et al., J Comput Phys **43** (1981) 61.

[6.8] L L Lao, et al., Nucl Fusion **25** (1985) 1611.

[6.9] D P O’Brien, et al., Nucl Fusion **32** (1992) 1351.

[6.10] X Litaudon, et al., 26th EPS Conf on Contr Fusion and Plasma Physics, Maastricht 1999, ECA Vol 23J (1999) 965.

7. NEON IMPURITY TRANSPORT EXPERIMENTS

K-D Zastrow[1], C Giroud[2]

JET Joint Undertaking, Abingdon, Oxon, OX14 3EA, UK
[1] UKAEA Fusion, Culham Science Centre, Abingdon, OX14 3DB, UK
[2] CEA Cadarache, DRFC/SIPP/CFM,F-13108 Saint Paul lez Durance Cedex, France

7.1 Overview

During the 1999 autumn campaign, we attempted Neon impurity transport experiments in ITB discharges. We chose the standard JET recipe with Argon radiation for edge control, since this provides the most steady background plasma conditions for these experiments. However, due to the difficulty of analysing the charge-exchange data (see section 13), we have been unable to progress with any transport analysis.

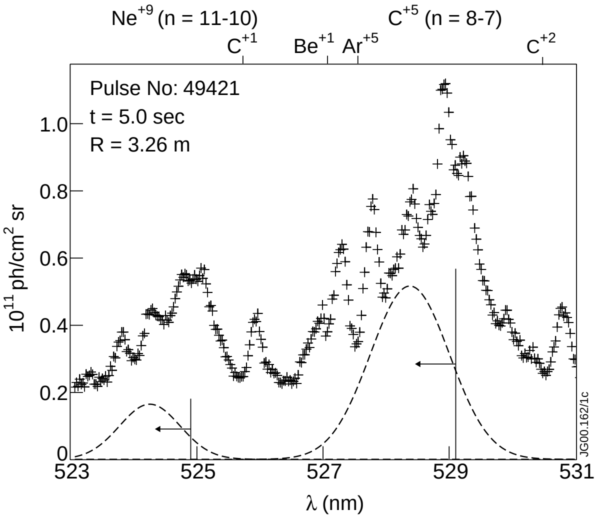

Fig.7.1: Charge exchange spectra from KS5A with Argon edge emission superimposed on the Carbon and Neon features. The Gaussian line shapes are an indication only of where the CX signal appears, and are not the result of the spectral analysis.

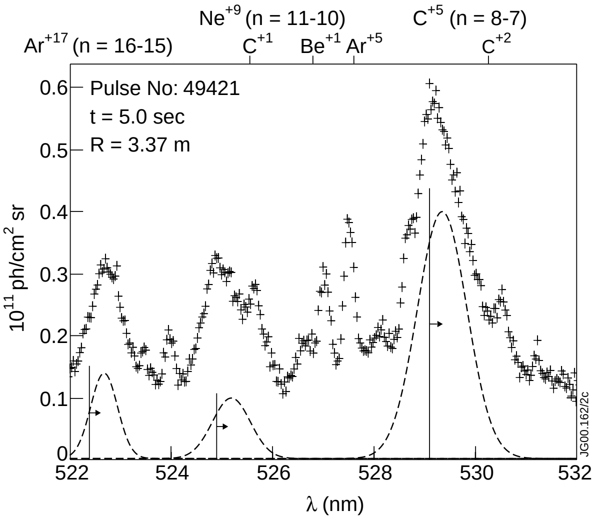

Fig.7.2: Charge exchange spectra from KS5B with Argon edge emission superimposed on the Carbon, Neon and Argon features. The Gaussian line shapes are an indication only of where the CX signal appears, and are not the result of the spectral analysis.

7.2 Results

The only analysis that could be performed is for discharge 49421, which had three NBI notches applied. The results are included in Section 13.

7.3 Summary and future directions

We are developing new analysis software to describe the CX spectra with Argon edge emission. It is possible that this will enable us to analyse these experiments. Impurity transport experiments under TF-S2 are proposed without Argon for edge control.

7.4 Shot List

Neon puff: 49418/2.5MA/2.6T and 49437/3.5MA/3.5T

Neon bleed before ITB, 49421/2.5MA, 2.6T and 49436/3.5MA, 3.5T

8. ITBS PRODUCED WITH LHCD PREHEATING

C D Challis[1], J Mailloux[1], Yu F Baranov[1], N C Hawkes[1], T C Hender[1] and S E Sharapov[1].

[1] JET Joint Undertaking, Abingdon, Oxon., OX14 3EA, UK.
EURATOM/UKAEA Fusion Association, Culham Science Centre, Abingdon, Oxon., OX14 3DB, UK.

8.1 Overview

The Optimised Shear regime in JET relies on relatively fast current ramp-up phase (of the order of 0.5MA/s) immediately following the plasma initiation. During this phase only Ohmic, and sometimes low power ICRH (up to 2MW), is applied, which maintains a relatively low plasma temperature. This typically provides a monotonic target q-profile for main heating with low magnetic shear in the plasma core whilst still allowing the central value of q to fall below 2 during the current ramp-up phase. The presence of a q=2 surface in the plasma interior has been found to assist in the formation of high performance ITBs in the JET scenario [2.1] while the continuation of the current ramp during the main heating phase avoids the development of large ELMs that are generally incompatible with ITB sustainment.

In the experiments described in this section LHCD has also been applied during the current ramp-up phase, before the main heating pulse, in order to modify the target q-profile. This scenario results in the formation of a target q-profile with lower or reversed central magnetic shear. The application of high power heating in these conditions generates a core ITB that is evidenced by steep gradients on the radial profiles of T_i, T_e and n_e. In contrast to the standard Optimised Shear scenario, this ITB does not appear to be linked to an integer q surface and does not significantly vary in location during the pulse or when the main heating start time is altered. A link between the location of the ITB and the q-profile has not been established beyond the suggestion that it resides within the reversed shear region. The resilience of the position of the ITB might also be related to the heating and torque deposition profiles. Both ITBs can be produced simultaneously following and LHCD prelude phase.

In low power experiments with an LHCD prelude the power required to form an ITB can be much lower than the threshold normally encountered with the standard Optimised Shear scenario. Further experiments are required to identify the critical conditions that determine this threshold power.

8.2 Results

Background

A typical example of the time evolution of a JET Optimised Shear experiment is illustrated in Fig.8.1. The X-point is formed soon after the plasma initiation and a large volume plasma is maintained throughout the current ramp-up phase. For the case shown in Fig.8.1 very little additional preheating was used (≈0.5MW of ICRH from 2.5s) and the main heating was increased to full power over 300ms during which time the plasma density was increased by the NBI fuelling to a suitable level for high power heating. After a short period of main heating a transport barrier formed in the plasma interior as indicated by an increase in the rise rate of the plasma neutron yield. This basic scenario with a fast current ramp-up phase and early application of additional heating is similar to the method used on other tokamaks (e.g. [8.2-8.4]).

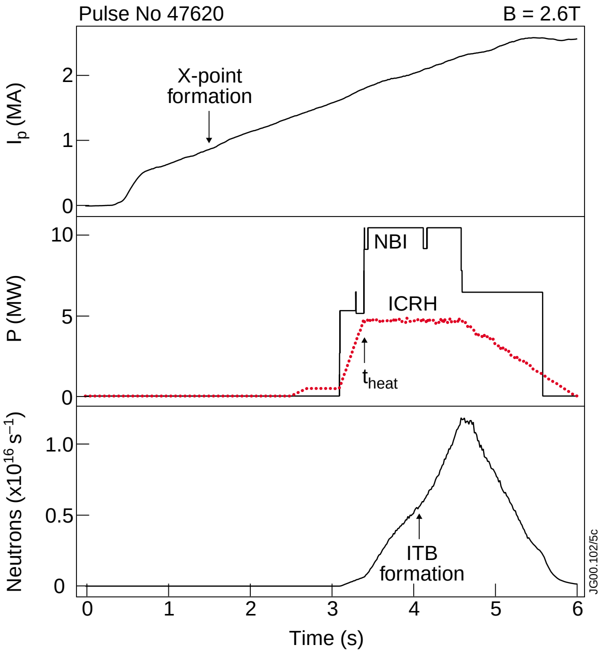

Fig.8.1: Time evolution of the plasma current, heating power and neutron yield for a standard Optimised Shear pulse.

An experiment to investigate the effect of the target q-profile by systematically varying the start time of the main heating pulse has previous reported confirmation of the important role played by integer q surfaces in the ITB formation process in the JET Optimised Shear regime [8.1]. Recent re-analysis of the target q-profiles for this series of pulses using the equilibrium reconstruction code EFIT [8.5, 8.6] constrained by data from motional Stark effect (MSE) measurements has now confirmed those initial findings.

Figure 8.2 shows the central q value at t_{heat}, the start of the main heating phase, for the series of pulses, which are similar to the one illustrated in Fig.8.1, but where t_{heat} has been systematically varied. 0.5MW of ICRH was applied from the same time in the preheat phase of all these pulses as indicated in Fig.8.1. The fall of central q with time in these pulses illustrates the rapid plasma current penetration in a relatively cold plasma during the current ramp-up phase and early part of the current flat-top.

Figure 8.3 shows the peak neutron yield obtained during the main heating phase for each of the pulses shown in Fig.8.2 plotted against the value of q_0 at the start of the main heating phase. Three pulses are indicated which exhibit an n=1 tearing mode in the plasma core suggesting a q=2 ‘island’ and electron temperature sawteeth are only evident on the pulse with the latest heating time. These indications provided benchmarks for the analysis process to determine the q-profile. It should be noticed that the highest performance was achieved when the main heating start time follows promptly the arrival of the q=2 magnetic surface in the plasma. This observation has been used to suggest that the q=2 surface can play a role in triggering an ITB in the JET Optimised Shear regime [8.1].

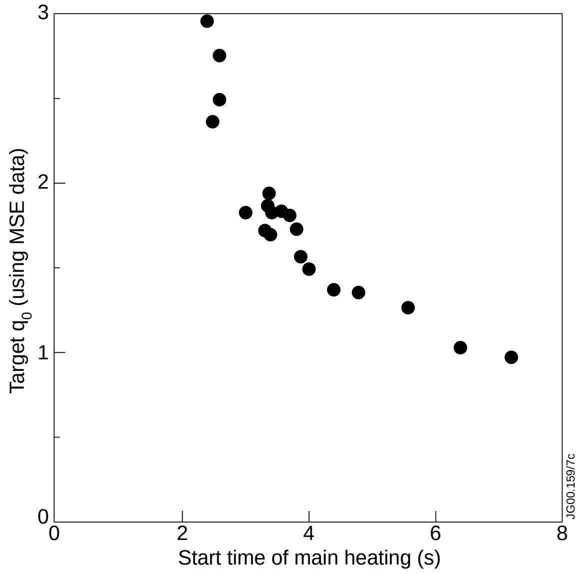

Fig.8.2: Variation of the target q_0 value with main heating start time, t_{heat}, in a series of discharges similar to that shown in Fig.8.1.

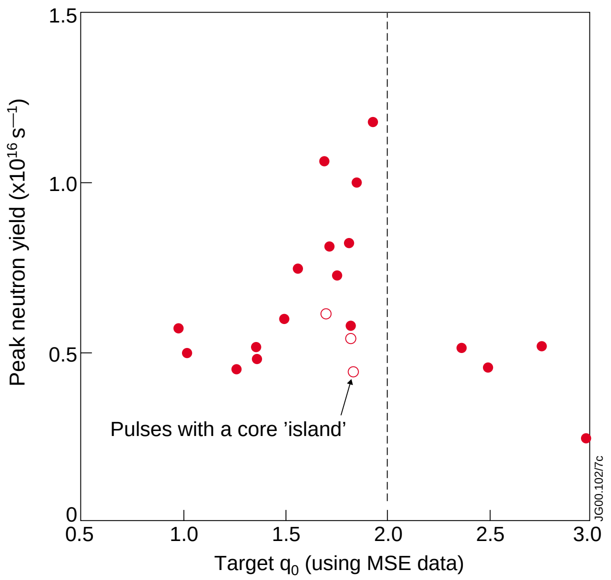

Fig.8.3: Peak neutron yield obtained during the main heating phase plotted against the start time of the main heating phase for the pulses shown in Fig.8.2.

Figure 8.4 shows the target q-profile for two different values of the main heating start time from the same series of pulses. It can be seen that in both cases the central magnetic shear is low, but that the q-profiles are monotonic. The early heating case has central q just below 2 at the start of the main heating pulse. A 'strong' ITB is formed in the core as evidenced by the production of a steep gradient in the profile of the electron temperature. This ITB expands rapidly and provides the high fusion yield indicated for this situation in Fig.8.3. In the case with the later heating the current penetration is more advanced and the central value of q is lower, although the radial profile of the magnetic shear has not been significantly altered. This results in a wider q=2 surface and coincident wider ITB trigger point. The pressure gradients obtained with a wider ITB tend to be lower than the case where the trigger point is on the plasma core. Ideally the q-profile should be studied at the moment of the ITB formation, but the analysis of the MSE data is most reliable at the beginning of the neutral beam heating pulse when the measurements are not confused by overlapping signals from different beams. In

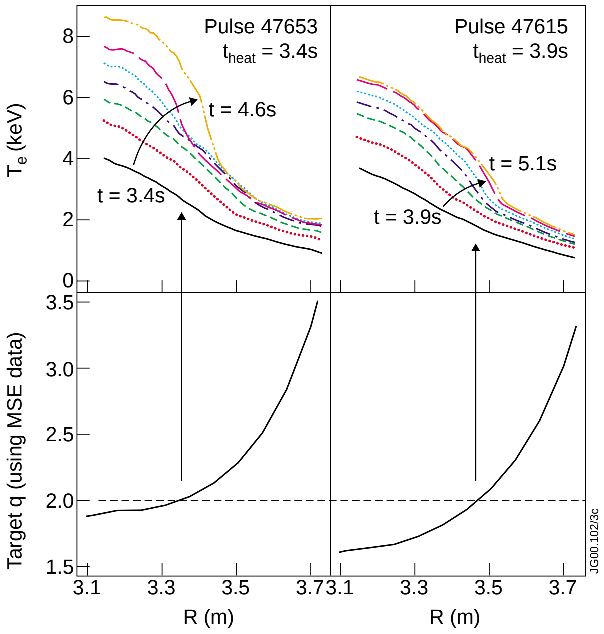

Fig.8.4: Target q-profile (at t_{heat}) and time evolution of the electron temperature profile during the main heating pulse, as measured from ECE emission using a heterodyne radiometer, for two values of the main heating start time.

any event it is believed that the q-profile does evolve significantly during the short time between the start of the main heating pulse and the ITB formation due to the high plasma temperature.

The link between the location of the q=2, and possibly q=3, magnetic surfaces and the formation of ITBs in JET might be explained by a perturbation in the plasma profiles due to MHD activity associated with the rational q surface. This possibility is discussed in section 9. The experiments described below were devised to investigate further the relationship between the q-profile and the transport in the plasma interior by varying the magnetic shear.

LHCD prelude on q-profile evolution

The most effective use of LHCD to modify the q-profile in JET Optimised Shear plasmas is during the current ramp-up phase. During the main heating pulse the plasma temperature is sufficiently high that the time required to substantially modify the current distribution in the plasma core is long compared with the typical high power pulse length. During the ramp-up phase, on the other hand, the plasma is much cooler so that the effect of both the non-inductive current drive and plasma electron heating act to significantly modify the q-profile evolution. This effect is illustrated in Fig.8.5, which show the plasma internal inductance two seconds after plasma initiation for pulses with various levels of applied LHCD power. The effect of applying LHCD power at this early time in the discharge is to significantly broaden the current profile as indicated by the reduction in the internal inductance. It should be noted that the current profile can also be affected to some extent by varying the current ramp rate. A detailed comparison of the classes of q-profile that can be obtained by the two different techniques has not been undertaken. It is likely that the two processes give different results as the LHCD drives current and provides heating to the plasma interior while the Ohmic current ramp adds current at the plasma edge. Further experiments are also required to assess the relative importance of the plasma heating with LHCD, which tends to ‘freeze’ the plasma current in the plasma interior, and the non-inductive current drive itself. In this report the net result of applying LHCD during the current ramp-up phase will be discussed together with the effects on the ITB dynamics.

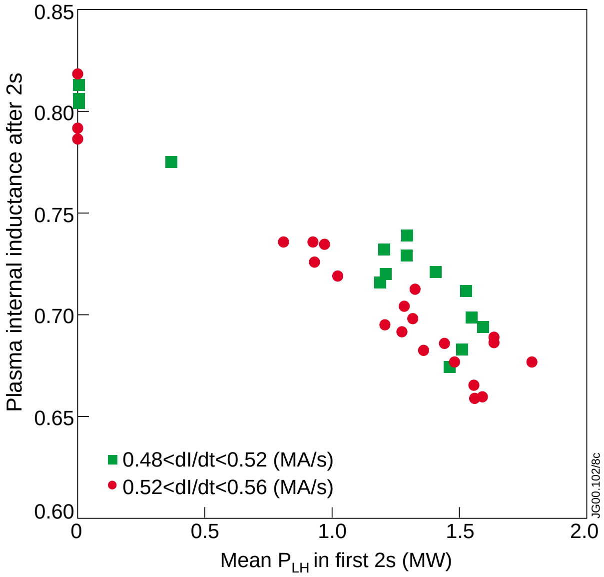

Fig.8.5: Plasma internal inductance 2 seconds after plasma initiation plotted against average LHCD power level up until the same time. The data are divided into 2 groups depending on the plasma current ramp rate.

A practical limitation on the current ramp-up rate and, possibly, the level of LHCD power that can be applied during this phase, is given by MHD instabilities encountered as q close to the plasma edge crosses low order rational values. Figure 8.6 shows the time evolution of a discharge with LHCD preheat that encounters an MHD instability as q_{edge} crosses 6. The plasma internal inductance changes abruptly due to the instability indicating that anomalous current penetration has occurred. Since these experiments were specifically intended to provide a broad target current profile for main heating, this anomalous transport of the plasma current is highly undesirable and the discharges were carefully tuned to avoid it.

It has been found that reducing the plasma triangularity has the effect of reducing the likelihood of such an instability being encountered as illustrated in Fig.8.7, which show the incidence of significant MHD associated with q_{edge}=6 in plasmas with different plasma current ramp rates, LHCD power levels and values of triangularity. It can be seen that for low shape plasmas there is a threshold in the plasma current ramp rate for the onset of this mode. However, there is no sign yet that increasing the LHCD power level causes this mode to be destabilised, despite the fact that the current profile is further broadened by this technique. This suggests that the application of LHCD is a much more effective tool for target q-profile control, and potentially for generating reversed magnetic shear plasmas, than simply varying the current ramp rate. With slightly higher triangularity plasmas the MHD mode is encountered with a lower current ramp rate, indicating a further means for optimisation of this scenario for producing very broad target current profiles.

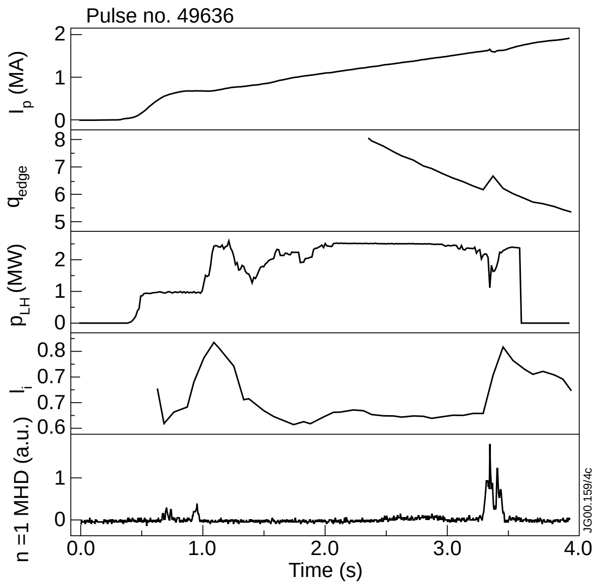

Fig.8.6: Time evolution of a discharge with LHCD preheat showing the plasma current, q near the plasma edge, LHCD power, l_i and level of n=1 MHD activity.

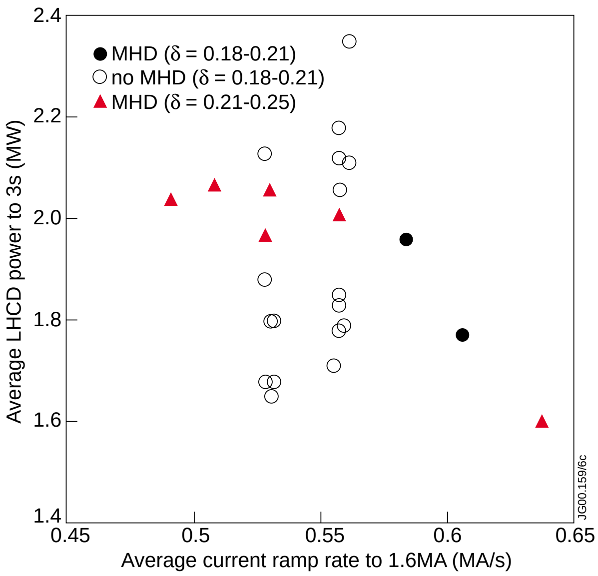

Fig.8.7: Average plasma current ramp rate in the period up to 1.6MA, close to q_{edge}=6, plotted against the average LHCD power applied during the first 3 seconds of the discharge. Circles represent low triangularity pulses (δ=0.18-0.21) and triangles indicate higher triangularity plasmas (δ=0.21-0.25). Solid symbols indicate cases where MHD activity is encountered at q_{edge}=6.

The effect of the LHCD prelude phase on the target q-profile for main heating is illustrated in Fig.8.8, which shows a comparison of the q-profiles, one with an Ohmic current ramp-up phase and the other with an average of 2.1MW of LHCD applied from the plasma initiation to the first application of NBI and ICRH power. The current ramp rate is slightly lower in the Ohmic ramp case, but the effect of this is small compared with the difference in LHCD power. The Ohmic prelude case produces a relatively peaked target current profile for main heating. The current ramp rate is slower than the cases shown in Fig.8.4. This, together with the absence of any ICRH preheat explains the relative increase in the magnetic shear seen in the Fig.8.8 example. The LHCD prelude dramatically broadens the target q-profile and is able to generate the magnetic shear reversal illustrated in the same figure.

TAE modes are typically seen in the ICRH preheat phase of JET Optimised Shear plasmas. In Fig.8.9 spectrograms of the MHD activity detected using fast magnetic sensors are compared for cases with and without LHCD power. The TAE modes are clearly seen in the no LHCD case as continuous modes in the frequency range around 120kHz. In the example with LHCD the classical signature of the TAE modes is absent, but instead cascading MHD modes are observed throughout the LHCD phase and this difference in behaviour persists long after the end of the LHCD pulse. TAE modes are known to be sensitive to plasma density and the q-profile. Since the density evolution of these two discharges is similar, the dramatic differences between the TAE mode character is thought to originate from the

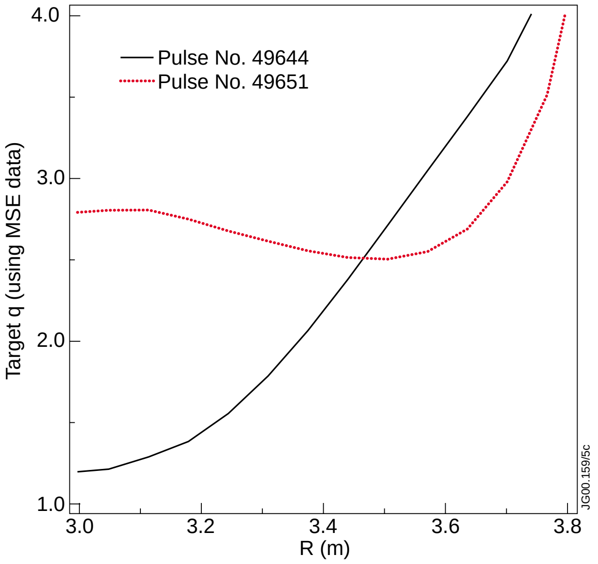

Fig.8.8: Target q-profiles for main heating for a case with an Ohmic current ramp-up phase (#49644 – solid line) and with an LHCD prelude (#49651 – broken line).

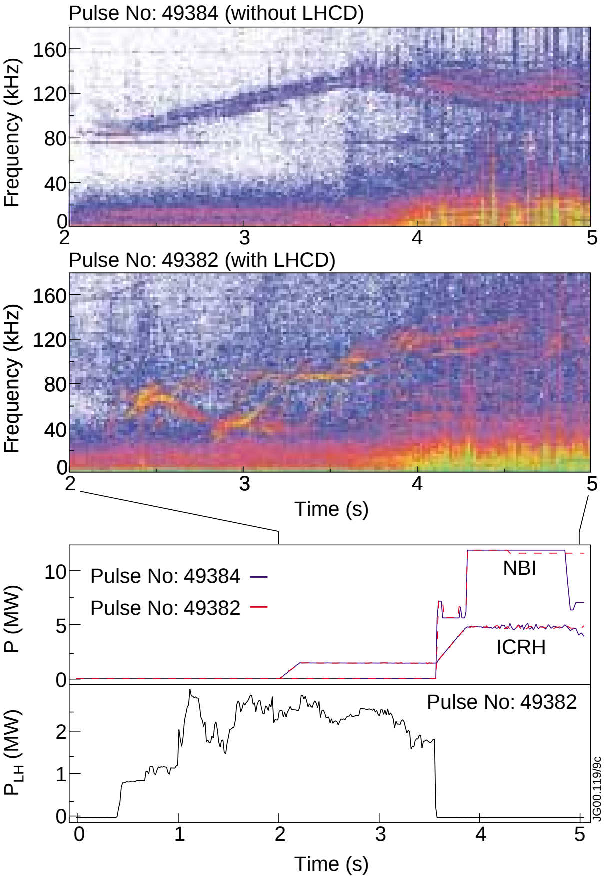

Fig.8.9: Spectrograms of the MHD activity detected using fast magnetic sensors for a plasma with (#49382) and without (#49384) LHCD. Both pulses have ICRH preheat.

modification of the q-profile during the LHCD phase. MHD similar to the LHCD case has been seen on other tokamak experiments with reversed magnetic shear [8.7]. The persistence of the change in the TAE behaviour also indicates that the legacy of the target q-profile modification remains throughout the main heating pulse and that differences in the ITB behaviour can be attributed to the changes in the target q-profile.

Sawtooth-like MHD events are sometimes seen during the LHCD prelude, which seems to be correlated with the level of LHCD power applied during the early phase of the current ramp. Figure 8.10 shows the sawtooth-like activity in the core of a plasma during the LHCD prelude as evidenced on the ECE data. In the presence of a substantial fast electron population generated by the LHCD, the magnitude of the electron temperature determined from the heterodyne radiometer measurements should be taken with some caution. However, the collapses in the plasma interior can be clearly seen on this data and mainly affect a same region near the plasma centre. In two cases where ICRH was also applied during the prelude phase the sawtooth-like events were absent. This may be due to a modification of the pressure or current profiles due to the addition of ICRH, although the divergence in the behaviour of the two discharges chosen to illustrate this in Fig.8.10 seems to occur before the ICRH power is applied. Nevertheless, an alternative explanation for the persistent absence of collapses in the combined LHCD and ICRH case is that the fast ion generated by the ICRH might stabilise this MHD mode. The possibility exists that these core collapses result in a redistribution of the plasma current which could act to prevent the development of a region of deeply reversed magnetic shear. In fact an analysis, using MSE data, of the q-profile generated in one of the combined LHCD and ICRH prelude phases suggests that indeed deep shear reversal might have been achieved, although this conclusion is

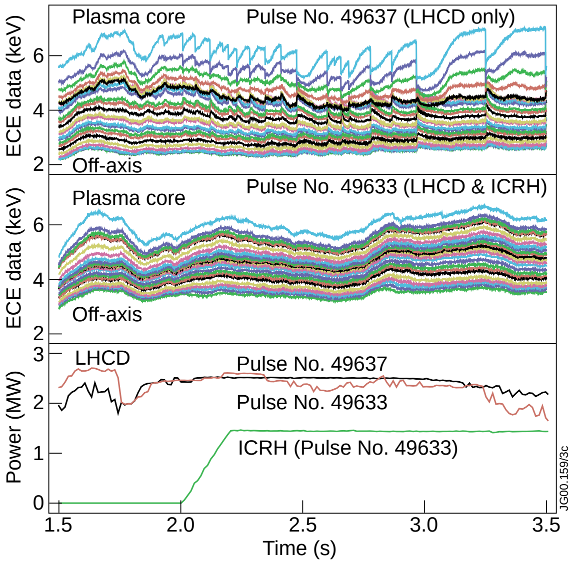

Fig.8.10: Time evolution of ECE data measure using the heterodyne radiometer during the prelude phase for pulses with LHCD and ICRH (#49633) and LHCD only (#49637).

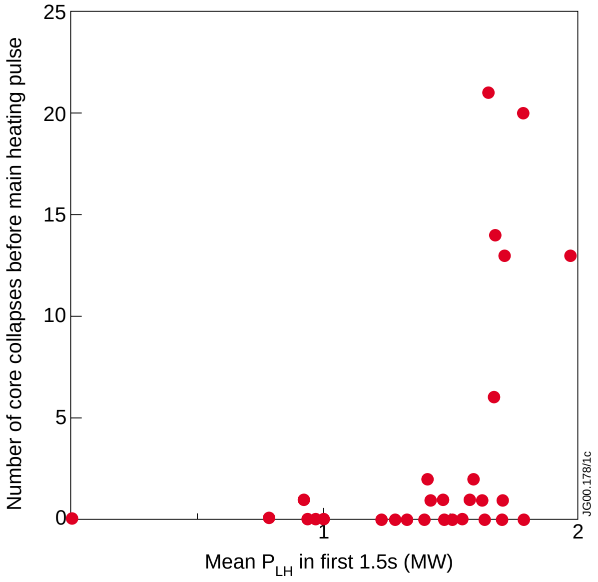

Fig.8.11: Number of sawtooth-like events during the LHCD prelude plotted against the average LHCD power coupled to the plasma during the first 1.5 seconds of the discharge.

inconsistent with data from the polarimeter (see section 14). Further investigation and analysis using the current profile diagnostics would be required for any firm conclusions to be drawn concerning the effect of this MHD phenomenology on the target q-profile.

Figure 8.11 shows the number of such sawtooth-like events during the LHCD prelude plotted against the average LHCD power coupled to the plasma during the first 1.5 seconds of the discharge. There seems to be a threshold in the LHCD power level for the onset of this instability, which might suggest a link to the q-profile modification affected by the application of LHCD.

Effect of LHCD prelude on ITB dynamics

Even before the main heating pulse there is some indication of an enhancement to the core confinement on the electron temperature profile. This effect can be seen the ECE data shown in Fig.8.10 for the LHCD only prelude where the signals on the core channels become well separated during the latter phase of the preheat. In contrast the combined LHCD and ICRH preheat case exhibits a lower core electron temperature despite the higher heating power level. A more thorough assessment of the heating, equipartition and loss channels must be performed before a conclusion that an electron transport barrier has been formed can be established.

A clearer conclusion can, however, be reached concerning the effect of applying high power heating to such discharges. Figure 8.12 shows the target q-profile with weakly reversed magnetic shear produced by an LHCD prelude phase together with the time evolution of the electron temperature profile during the subsequent high power heating phase, which exhibits the formation of an ITB at a plasma radius of about 3.35m. In this case the q-profile shown, which has been determined using MSE data, is consistent with the polarimetry measurements.

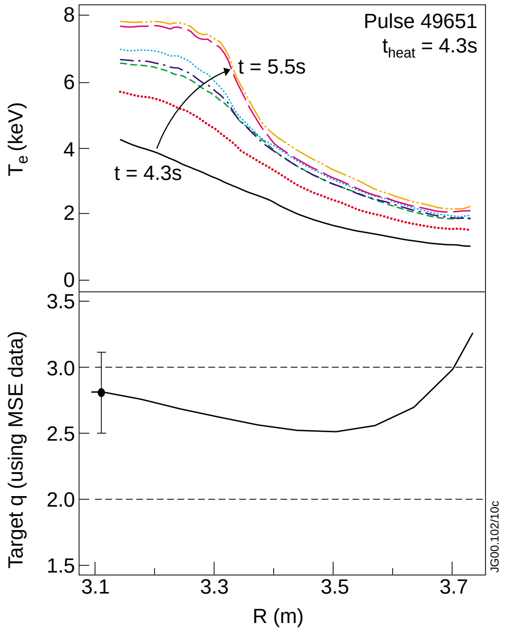

Fig.8.12: Target q-profile (at t_{heat}) after LHCD prelude and electron temperature profile evolution during the subsequent high power heating phase.

In contrast to the standard JET Optimised Shear regime, as illustrated in Fig.8.4, there is no obvious link between the location of the ITB and an integer q surface. However, in the case shown in Fig.8.12 the possibility that a second q=3 surface might exist in the plasma core cannot be ruled out due to the uncertainties in the determination of the value of central q. A coarse timing scan has been performed to determine whether this core ITB depends on the location of integer q surfaces following the methodology described above for the standard Optimised Shear experiments and illustrated in Figs.8.2 to 8.4. Although the higher electron temperature provided by the LHCD prelude may act to reduce the sensitivity of the value of central q to the start time of the main heating, the penetration of the plasma current is not completely avoided and this, together with the shot-to-shot irreproducibility of the plasma initiation, must result in some variation in the q-profile in the plasma core. Figure 8.13 shows the ion and electron temperature profiles for three discharges where the start time of the main heating was varied by 1.2 seconds. A core ITB located at about 3.35m is evident on all the pulses and is a typical feature of experiments with an LHCD prelude. The insensitivity of the location of this ITB to the timing of the main heating pulse and the irreproducibility of the plasma initiation conditions, and the absence of any significant ITB expansion during the main heating phase, as illustrated by the comparison of the ITB evolution in Fig.8.12 and 8.4, lead to the conclusion that integer q surfaces do not play a significant role in its formation or evolution. It is also evident in Fig.3.13 that both types of ITB can be generated simultaneously. The outer ITB is linked an integer q surface, either q=2 or q=3, and displays the usual sensitivity to main heating start time, while the location of the inner ITB remains close to 3.35m.

The critical parameter, which determines the location of the core ITB following an LHCD prelude, has not been identified. It is likely that the magnetic shear plays a role since this is the key parameter that is altered by the LHCD phase, and the possibility that the radius of q_{min} is linked to the location of the ITB cannot be discounted within the uncertainties of the q-profile determination. It should also be borne in mind that the power and torque deposition profiles are essentially invariant in these experiments and that these may provide an optimum location for suppression of turbulence through the plasma flow shear which they generate.

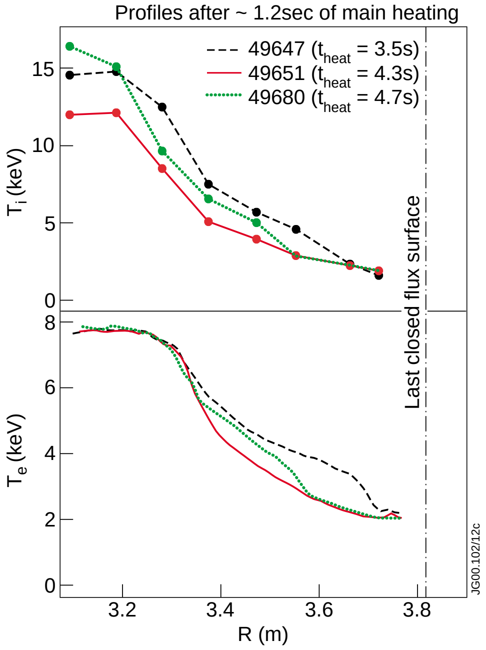

Fig.8.13: Ion and electron temperature profiles generated by a period of main heating following an LHCD prelude. The start time of the main heating pulse has been varied for the three pulses.

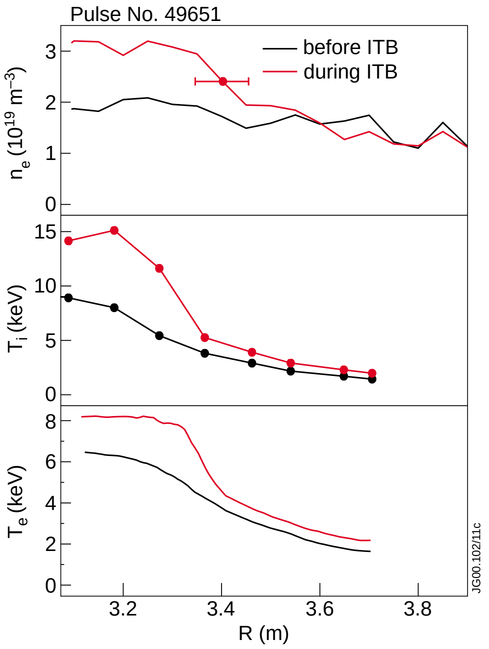

Fig.8.14 Profiles of T_e, T_i and n_e before (solid lines) and after (broken lines) the formation of an core ITB in a case with an LHCD prelude.

The core ITB produced after an LHCD prelude is evident on the profiles of T_e, T_i and n_e as illustrated Fig.8.14. This characteristic is also typical of ITBs in the standard JET Optimised Shear regime.

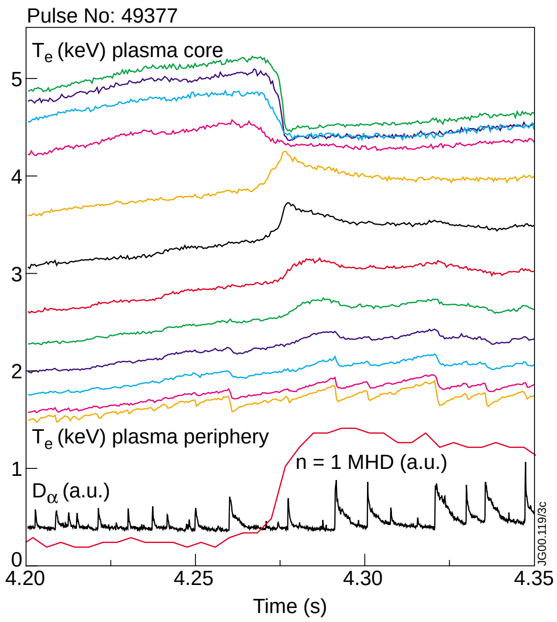

Fig.8.15: Time evolution of the plasma electron temperature at various radii from the plasma core to the periphery together with signals indicating the relative $D\alpha$ emission and level of n=1 MHD activity.

Core collapses are sometimes encountered during the high power heating phase of these discharges. Figure 8.15 shows the time evolution of the electron temperatures at various radial locations from the plasma core to the periphery in a plasma where such a collapse occurred. The collapse is seen to be localised in the plasma core and is not related to the ELM activity as the plasma edge, signified by the spikes in the $D\alpha$ emission. An n=1 tearing mode is evident at the time of the collapse. Cross correlation between the fast magnetics data and soft x-ray measurements signifies a phase inversion at the plasma centre suggesting an odd-m mode number. This is then thought to signify q=3 'islands' in the plasma at a radius of 3.23m, the location being inferred from fast ECE emission measurements. The relative phase of the ECE and magnetics signals suggests that the islands exist in a region of reversed magnetic shear. Given that the main heating start time is earlier in this case than the pulse shown in Fig.8.12, and consequently the target central q value is expected to be slightly higher. This is consistent with both the conclusions drawn from the collapse characteristics concerning the location of a q=3 surface and with the q-profile measurements for both pulses.

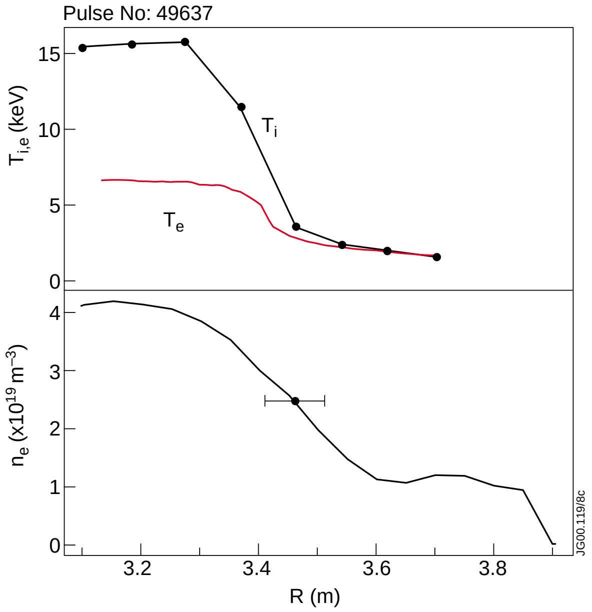

Fig.8.16: Profiles of T_e, T_i and n_e at ≈7.4s for a plasma with 20MW of main heating following an LHCD prelude phase. The error bar on the LIDAR n_e profile indicates the region over which the measurement is effectively smoothed.

So far only one attempt has been made to examine the dynamics of this ITB with high power and long pulse heating. Figure 8.16 shows the very steep gradients that were achieved in this case with 20MW of additional heating (15MW of NBI and 5MW of ICRH). This plasma disrupted soon after the time at which the profiles shown in Fig.8.16 were measured, presumably due to an MHD instability driven by the very large and localised pressure gradient. Although the generation of this very strong ITB was partly due to a lack of control of the ELMs during the current flat-top, it illustrates the need to investigate means by which the ITB radius can be increased in this scenario if it is to be exploited for high performance applications.

Preliminary experiments have been performed to evaluate the power threshold for ITB formation in plasmas with an LHCD prelude. At 7MW (5MW of NBI and 2MW of ICRH), the lowest power level attempted, an ITB was still formed. This is contrasted with the usual power levels required to form a clear ITB in the standard JET Optimised Shear regime in Fig.8.17. All of the standard scenario pulses illustrated in Fig.8.17 are believed to have monotonic q-profiles with ITBs formed close to the q=2 magnetic surface. The reason for the achievement of an ITB at lower power following the LHCD prelude has not yet been established, but this result indicates that optimisation of the q-profile shape can strongly affect the heating power required to achieve ITB formation.

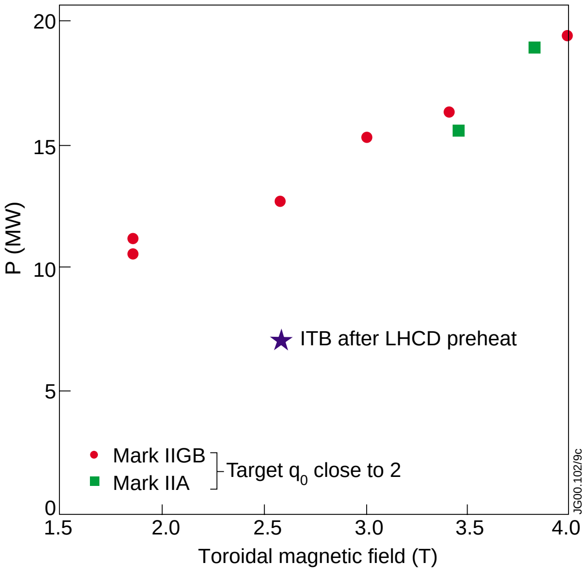

Fig.8.17: Power level required to form a clear ITB as a function of toroidal magnetic field strength for the standard JET Optimised Shear regime and the lowest power case of an ITB following an LHCD prelude at 2.6T.

8.3 Summary and future directions

This section describes the production of an internal transport barrier with characteristics that differ from the standard JET Optimised Shear regime. The ITB, which is obtained during high power heating following an LHCD prelude phase, is located in the plasma core apparently within a region of reversed magnetic shear. The position of the ITB does not vary significantly during the pulses or from shot-to-shot, and it therefore unlikely to be linked to the location of an integer q surface. The transport barrier is, however, evident on T_e, T_i and n_e, as is typical of ITBs in JET. Preliminary experiments suggest that the power threshold for ITB formation is lower in this scenario than is usual for JET Optimised Shear experiments.

The full characterisation and exploitation of this new domain of operation for JET is an immense task. Nevertheless, key areas for further experimental work include:

- The determination of the relative importance of the LH current drive and heating, perhaps by comparison with equivalent on- and off-axis ICRH preheat experiments.

- An investigation of the link between the ITB dynamics and the q-profile, magnetic shear, heating and applied torque profiles.
- The measurement of the power threshold for a range of target q-profile shapes..
- A study and further expansion of the range of q-profiles with which ITB can be produced and the prospects for optimising the current profile for the production of wider ITBs.
- An assessment of the processes leading to the enhancement of the core electron temperature during the LHCD prelude phase.
- An exploitation of the apparent low power threshold after an LHCD prelude at high toroidal magnetic field strength.

8.4 Shot List

Shot	Comment
47896	no LHCD reference
47897	1.7MW LHCD
47898	1.9MW LHCD
47899	2.1MW LHCD
47952	1.9MW LHCD
47955	1.9MW LHCD, LH phasing changed
47956	no LHCD reference
47958	1.9MW LHCD + 10MW of NBI power
49204-49209	**A series of LHCD preheat pulses where the current ramp rate and ramp duration was reduced to avoid MHD.** **There was some variation of theat, but large ELMs were encountered during main heating in the current flat top.**
49204	Current ramp rate scan 1
49205	Current ramp rate scan 1
49206	Current ramp rate scan 1
49207	Delayed main heating
49208	ICRH preheat scan 1 (LHCD & ICRH preheat)
49209	ICRH preheat scan 1 (ICRH preheat only)
49373-49384	**LHCD preheat pulses with further tuning of the current ramp rate and duration.** **The start time of the LHCD was varied.** **ITBs were achieved during the main heating pulse.**
49374	LHCD start time scan
49375	LHCD start time scan
49376	LHCD start time scan
49377	Current ramp rate scan

Shot	Comment
49378	Current ramp rate scan
49379	Current ramp rate scan
49380	Current ramp rate scan
49381	ICRH preheat scan 2 (LHCD preheat only) - also current ramp rate scan
49382	ICRH preheat scan 2 (LHCD & ICRH preheat)
49383	Altered LHCD phasing (cf. 49381)
49384	ICRH preheat scan 2 (ICRH preheat only)
49629-49643	**Attempt to improve LHCD coupling by modifying the plasma shape.** **No significant progress in ITB production.**
49629	lower LHCD power
49630	Heating timing scan - effect of plasma shape on LHCD coupling
49633	LHCD & ICRH preheat
49636	effect of plasma shape on LHCD coupling
49637	effect of plasma shape on LHCD coupling (also reduced current ramp rate)
49641	effect of plasma shape and current ramp
49643	effect of plasma shape and current ramp
49644	effect of plasma shape and current ramp
49645	effect of plasma shape and current ramp
49644-49651	**Main heating timing scan which includes one pulse from the previous shift.**
49647	Heating timing scan
49651	Heating timing scan
49652	no LHCD reference
49679-49683	**Completion of the timing scan.** **Attempted a threshold power scan, but the minimum required power was not reached.**
49680	Heating timing scan - also threshold power scan
49682	Threshold power scan
49683	Threshold power scan

Acknowledgements

It is a pleasure to acknowledge the contribution of B Stratton of the Princeton Plasma Physics Laboratory in the determination of the q-profile using MSE data.

References

[8.1] C D Challis, et al., 26th EPS Conf on Contr Fusion and Plasma Physics, Maastricht 1999, ECA Vol 23J (1999) 69.

[8.2] F M Levington, et al., Phys Rev Lett **75** (1995) 4417.

[8.3] E J Strait, et al., Phys Rev Lett **75** (1995) 4421.

[8.4] T Fujita, et al., Fusion Energy 1996 (Proc 16th Int Conf Montreal, 1996), Vol 1, IAEA, Vienna (1997) 227.

[8.5] L L Lao, et al., Nucl Fusion **25** (1985) 1611.

[8.6] D P O’Brien, et al., Nucl Fusion **32** (1992) 1351.

[8.7] Y Kusama, et al., Nucl Fusion **38** (1998) 1215.

9. EFFECT OF MHD ON ITB TRIGGERING

E. Joffrin[1], B. Alper[2], C.D. Challis[2], T.C. Hender[2], D. Howell[2], G.T.A. Huysmans[1], K.D. Zastrow[2]

JET Joint Undertaking, Abingdon, Oxon, OX14 3EA, UK.

[1] Association Euratom-CEA, CEA Cadarache, F-13108, St. Paul lez Durance, France

[2] Euratom/UKAEA Fusion Association, Culham Science Centre, Abingdon, Oxon.

9.1 Overview

Studies of the underlying process to form internal transport barriers (ITB) have remained an important part of the Optimised Shear experiments [9.1] on JET during 1999. Analyses have shown links between integer q surfaces and ITBs [9.2]. A power timing scan experiment has revealed that the q=2, and also the q=3, surfaces appear to play a major role in the formation of the barrier. In addition, the sensitivity to the integer q-surfaces seems to decrease as the input power is increased above the power threshold for ITB production. Signs of the role of magnetic rational surfaces has also been observed on other devices, such as JT60-U [9.3] or TFTR [9.4]. This experimental evidence suggests that a trigger mechanism might be responsible for the onset of ITBs.

This section presents a new candidate mechanism explaining the triggering of ITBs in JET, which is consistent with the experimental evidence on the power threshold and on the role of integer q-surfaces. In particular, the coupling between edge magneto-hydro-dynamic (MHD) activity and internal integer q-surfaces is analysed both experimentally and by a computational model. There is a good correlation between the occurrence of n=1 MHD related to integer edge-q values and the formation of the ITB, suggesting the MHD is causal in forming the ITB. Simulations show that for q-profiles with low central shear, and q=2 in this low shear region, that edge current driven modes can couple toroidally to drive m=2, n=1 islands. It can be speculated that these q=2 islands locally affect the flow shear, thus triggering the ITB, but this remains a subject for future study.

9.2 Results

Role of rational q surfaces in the ITB formation

The heating timing scan experiment [9.2] (2.6T with 10.5MW of neutral beam heating and 5MW of ion resonance heating) has revealed the link between integer q-surfaces and ITB formation. In this experiment, the time of the main heating is scanned during the current rise (0.4MA/s). High performance ITBs are only encountered when the target q_o is close to 2 (Fig.9.1 and 9.2a). In this case, the foot of the barrier is located at 3.35-3.4m (Fig.9.2b).

With later heating and therefore at lower target q_o, weaker ITBs are formed at a wider radius (typically 3.5m) consistent with the location of the q=2 surface. Also, early heating can produce very wide ITBs (foot at R~3.65m) indicating a possible link with the q=3 surface. This is indeed confirmed statistically when comparing the ITB foot point location determined on temperature profile with the position of the q=3 surface determined by the EFIT equilibrium code. The q=3 surface lies systematically outside the ITB foot point. This is very similar to the observations in JT-60U [9.3] for weak positive shear plasma.

It is also important to note that with the optimum timing either prompt ITBs or flattening are observed on the electron temperature profile. This flattening is associated with the presence of a core q=2 island growing possibly in the low shear region in the plasma centre, confirming that q_o is close to 2.

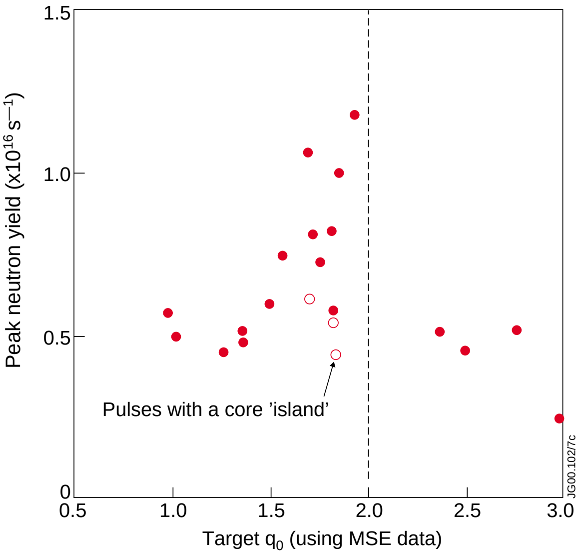

Fig.9.1: Peak fusion yield obtained against q_o when scanning the heating time.

In addition to revealing the role played by integer rational q, the heating timing scan is also a very useful tool to study the ITB triggering itself.

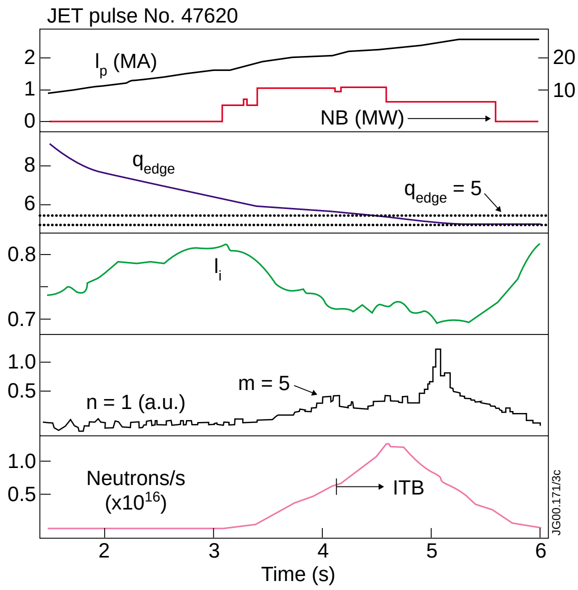

Fig.9.2: (a) example of a timing scan pulse at the optimum timing showing the correlation between the barrier onset and the edge MHD. 4.5MW of ICRH power is also applied in the main heating phase.

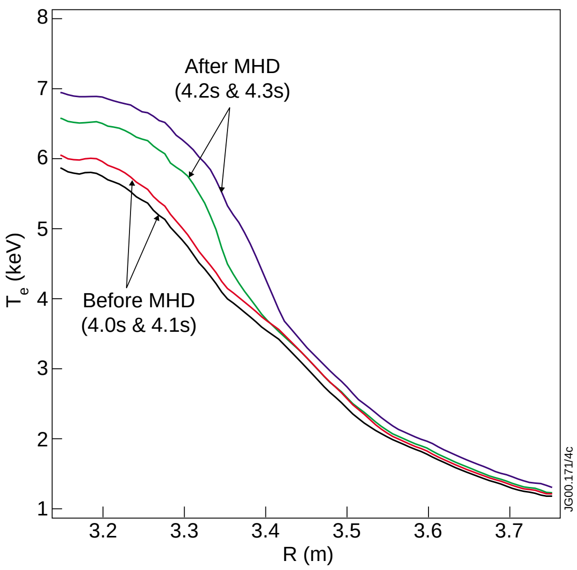

Fig.9.2: (b) Te profiles at the ITB formation during the edge external n=1 m=5 mode.

When the additional heating is applied during the current ramp-up, the internal inductance starts to drop (Fig.9.2a), indicating the accumulation of edge current due to the increase of electron temperature and the decrease of plasma resistivity. As q_{edge} approaches integer values such as 5, the edge current destabilises an external n=1 m= q_{edge} MHD mode. This can been seen on Fig.9.2a showing the n=1 component when q_{edge} crosses q=5 for li close to 0.7. It appears that the ITB is triggered simultaneously (at 4.1s) as illustrated by the increase of the neutron rate and by the temperature profile shown in Fig.9.2b. Here, ITBs are characterised in location and onset time using the electron temperature measurements from the ECE heterodyne radiometer. The ITB onset time can be determined within ±100ms from the ‘break’ of the slope of Te profiles. Thanks to the spatial resolution of this diagnostic, the ITB foot point location can be determined to within 6cm.

Using this procedure for the determination of the ITB onset time, the whole heating timing scan data set has been analysed to verify the role played by the external rational surfaces. It can be seen on Fig.9.3 that the ITB onset time does not follow regularly the heating time. In fact, it appears that there is a clustering of the ITB formation time when rational edge q surfaces penetrates into the plasma (particularly at, q=5 and 6). Therefore, the edge MHD mode , associated with an integer q_{edge}, seems to be the cause of the triggering of the barrier near the q=2 surface.

To confirm the correlation between the edge MHD mode and the onset time of the ITB, a database of more than 40 discharges has been built up with different current ramp-up rate (from 0.37MA/s to 0.45MA/s) and different field (2.6T and 3.4T). The MHD onset time has been taken at its start (4s in the case shown on Fig.9.2a). The ITB onset time is seen to be well correlated, and generally slightly after the edge MHD (Fig.9.4), indicating the causal role played by the external MHD mode in the ITB triggering.

The above experimental analysis strongly suggest the presence of a link between the triggering of the ITB and the MHD on the outermost integer q surface driven by the accumulation of edge current in the current ramp-up. Since the ITB is also believed to be linked with integer internal rational q surfaces, toroidal coupling to a q=2 tearing mode is the prime candidate to explain the possible linkage between these surfaces.

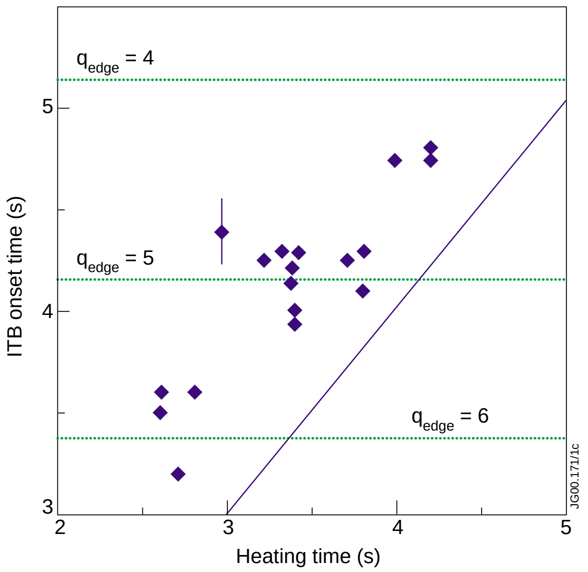

Fig.9.3: relation between the ITB onset time and the time of the main heating.

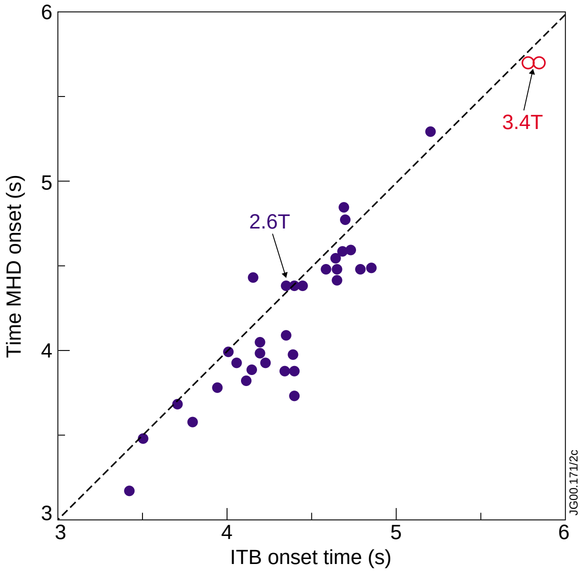

Fig.9.4: Correlation between the n=1 edge MHD onset time and the ITB onset for various current ramp-up rate (0.37 to 0.45 MA/s) and toroidal field.

Coupling between edge (q=5) and internal (q=2) surfaces and their effect on rotation

Stability of coupled tearing modes depends essentially on the plasma shape (aspect ratio, elongation, triangularity), pressure peaking inside the considered surface (i.e. q=2 here), and magnetic shear through the island size [9.5]. Coupling between n=1 rational surfaces has been computed with the CASTOR code using typical equilibrium from the JET discharge 47667 with the optimum heating time (i.e. target q_o is close to 2). The edge current has been modified to reproduce the edge current accumulation in the current ramp-up and to stimulate the destabilisation of edge mode on q=5. The central shear has also been varied to check its effect on the q=2 island and on its coupling with the q=5 perturbation.

The code calculations demonstrate that coupling can occur between the external mode on q=5 and the q=2 suface. Figure 9.5 shows the increase of the growth rate of the n=1 mode when q_{edge} approaches 5. The width of the resulting island on q=2 is comparable to the edge-q kink mode distortion. The ratio of the island width to edge kink distortion depends on the local shear on the q=2 surface, becoming larger when the q=2 surface is in a low shear region. This is consistent with the experimental observation that the optimum heating timing can produce either an m=2 n=1 mode or a strong internal barrier as observed experimentally in Fig 9.1.

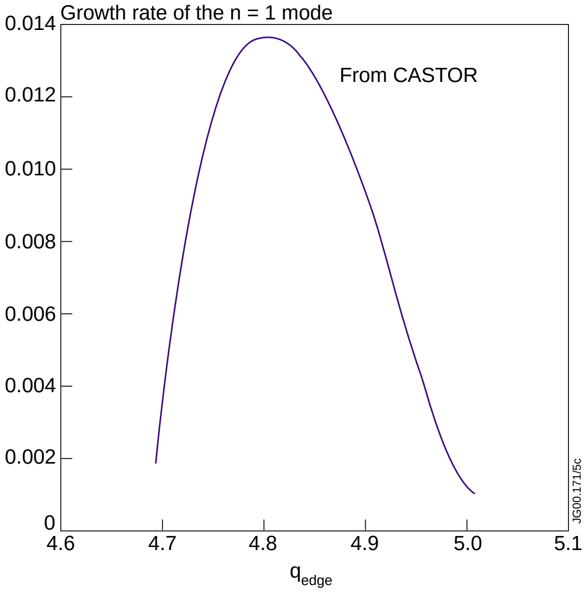

Fig.9.5: Evolution of the growth rate of the n=1 mode when q_{edge} approaches 5 as computed with the CASTOR code.

Both resistive and ideal calculations also confirm the strong effect of the pressure peaking on coupling. This pressure dependence is consistent with the observation that a minimum heating power is required (power threshold) [9.1]. Furthermore, ICRH phasing experiments [9.6] have shown that central peaked power deposition profiles are more likely to produce an ITB than broad ones. Similar conclusions have also been drawn from experiments balancing off- and on-axis neutral beam injection [9.7].

Experimentally, signs of mode coupling have been noticed on the fast acquisition data of magnetics. In some cases the toroidal and poloidal structure of the external n=1 mode is strongly modified when the barrier forms suggesting that coupling takes place at this time. Simultaneously, an m=2 n=1 perturbation has also been detected close to the foot the barrier with electron temperature fluctuations from an ECE heterodyne radiometer indicating the possible presence of an m=2 island at the foot of the barrier.

When this coupling takes place and once the amplitude of the external mode is sufficiently high, one or more coupled surfaces inside the plasma can suddenly ‘lock’ with this external mode (i.e. their natural frequencies are brought into coincidence with the outermost surface). Once locked, it is predicted [9.5] that the modes could locally modify the gradients of the bulk toroidal rotation. Such modification are opposed by the action of perpendicular plasma viscosity and the profile relaxes to steady state on a viscous diffusion time-scale which is of the order of a few tens of milliseconds in the case of the discharges analysed in this paper. The resulting modification of the bulk rotation can increase locally the ExB shearing rate which, in turn, stabilises the turbulence and triggers the ITB.

9.3 Summary and future directions

The Optimised Shear experiments conducted on JET during 1999 have identified the link between internal integer q surfaces (q=2 or q=3) and ITB formation. From the present analysis, it also appears that the MHD taking place on edge q surfaces, during the current ramp-up, is playing a key role in the ITB triggering. Code computations with CASTOR show that coupling between internal and edge surfaces is possible and consistent with the experimental observations. Once locked, the coupled modes could lead to local changes of the toroidal rotation gradient and to the stabilisation of the turbulence by the increase of rotational shear. Ultimately, this mechanism opens the prospect to control ITBs by exciting an m=2 n=1 perturbation with saddle coils or by modifying the plasma shaping parameters or heating deposition profile conditions. Further experiments are planned both avoiding integer edge-q values to see how this affects the ITB power threshold and also using the JET internal saddle coils to deliberatly drive m=2, n=1 islands to see how this alters the power threshold.

9.4 Shot list

The shots used to produce Fig 9.4 are given in Table 9.1.

Table 9.1: Shots used to establish causal link between edge MHD and ITB triggering in Fig 9.4.

Shot	q_{edge} (at ITB time)	ITB time (s)	MHD time(s)
49624	4.85	4.9	4.6
49616	5.1	4.6	4.6
49613	4.85	5.05	4.5
49421	5.35	4.25	4.4
49412	5.3	4.35	4.4
49403	5.2	4.4	4.4
49392	5.7	4.2	4.45
49018	5.72	4.1	4.4
48988	5.05	4.25	4.5
48974	4.96	4.45	4.1
48907	4.5	4.7	4.78
48907	5.15	3.85	3.8
49654	5.2	4.45	4.4
49340	4.5	5.2	5.3

Shot	q_{edge} (at ITB time)	ITB time (s)	MHD time(s)
49362	5.01	4.7	4.45
49342	4.99	4.75	4.5
49443	5.01	4.7	4.5
49614	4.8	4.8	4.55
47620	5.02	4.15	3.9
47621	5.05	4.25	3.85
47630	4.84	4.4	3.75
47647	5.2	4.0	3.95
47648	4.99	4.2	3.95
47650	4.9	4.3	3.9
47652	5.15	4	3.95
47653	4.95	4.3	4
47660	5.23	3.95	4
47685	4.9	4.3	4
47688	4.93	4.3	3.9
47689	5.06	4.1	4
47640	5.75	3.5	3.5
47643	5.73	3.6	3.6
47645	6.1	3.2	3.2
47646	5.76	3.6	3.7
47611	4.32	4.75	4.05
47614	5	4.25	4.0
47618	4.37	4.8	4.8
47619	4.4	4.75	4.85
47606	4.17	4.25	4.0

References

[9.1] C. Gormezano, et al., Plasma Phys. Control. Fusion, Vol 41, B367 (1999).

[9.2] C. Challis, et al., 26th EPS Conf. On Contr. Fusion and Plasma Physics, Maastricht, Vol. 23J (1999), p 69-73.

[9.3] T. Fujita et al. 16th IAEA Fusion Energy Conference, Montréal, Canada, 7-11 October 1996, IAEA-CN-64/A1-4.

[9.4] M. Bell, et al., Plasma Physics and Controlled Fusion, Vol 41, A719, (1999).

[9.5] R. Fitzpatrick, et al., Nuclear Fusion, Vol 33, No 10, (1993).

[9.6] L. Eriksson, et al, 26th EPS Conf. On Contr. Fusion and Plasma Physics, Maastricht, Vol. 23J (1999), p 1013-1016.

[9.7] F.X. Söldner, et al., 26th EPS Conf. On Contr. Fusion and Plasma Physics, Maastricht, Vol. 23J (1999), p 185-188.

10. ANALYSIS OF NBI AND ICRH HEATING IN OPTIMISED SHEAR DISCHARGES WITH ITBS.

Y.Baranov[1], C.Challis[1], A.Gondhalekar[1] and D.McDonald[1]

JET Joint Undertaking, Abingdon, Oxon, OX14 3EA, UK
[1] EURATOM/UKAEA Fusion Association, Culham Science Centre, Abingdon, Oxon, UK

10.1 Overview

The formation and sustainment of Internal Transport Barriers (ITBs) in Optimised Shear (OS) discharges depends on many parameters such as plasma heating efficiency, deposition profile, plasma pressure gradient, toroidal rotation velocity, magnetic shear and q profile. The dependencies of these parameters on NBI and ICRH power have been analysed statistically using the JET database. Direct comparison of NBI and ICRH heating has been done in a dedicated experiment and results are presented in this report. The power deposition profiles and plasma thermal diffusivities were modelled using the TRANSP [10.1,2] and PION [10.3] codes. Results of the modelling are also shown.

A dedicated experiment for the comparison of ICRH and NBI heating has been carried out with a limited number of pulses and relatively small variation of the plasma conditions. The heating power waveform has been carefully tuned to produce ITBs. The experiment showed that the power threshold for the ITB formation is very close in discharges with NBI only and combined ICRH and NBI heating. The main plasma parameters are very similar in discharges of both types provided that the total heating power is the same.

A statistical analysis shows that both NBI and ICRH heating can be very efficient in ITB formation and sustainment. It should be noted that the maximum available ICRH power on JET is roughly two times smaller than NBI power. R_{NT} is proportional to W_{dia}**1.9 in OS discharges with ITB with the correlation coefficient (square of the Pearson product moment) R=0.93. There is no pronounced dependency in the ITB threshold power (P_{ap}), and the highest accessible R_{NT} and W_{dia}, on the P_{RF}/P_{NB} power ratio. Nevertheless, there are trends that depend on the ratio P_{RF}/P_{NB}. In particular, the averaged R_{NT}/W_{dia}**1.9 decreases in the discharges with higher P_{RF}. The increment in W_{dia} is smaller on average in discharges with highest P_{RF}. Partially this effect is associated with a pronounced decrease in the pedestal density. The toroidal rotation V_{tor} is a function of P_{NB} with only a weak dependence on P_{RF} .

Further experiments directed at the efficient utilisation of the combined ICRH and NBI heating are required. It is necessary to increase the range of the ratio of P_{RF}/P_{NB} to gain further understanding of the role of the different heating methods. This ratio did not significantly exceed 0.4 in the reported experiments.

10.2 Results

1) Direct comparison of NBI and RF heating in OS discharges.

The power waveform has been tuned to produce an ITB in OS discharge with NBI heating only (pulse # 49362). An ITB has been observed in a discharge with approximately the same total power waveform when combined NBI and RF heating was applied (pulse #49654). The evolution of the main plasma parameters is shown in Fig.10.1.

Two more shots are shown in Fig.10.1 with slightly lower total heating power. NBI heating only was used in pulse #49443. Combined RF and NB heating was applied in pulse #49655. Neither of them produced evident ITBs. It is clear from comparison of these four pulses that the power P_{ap} required for ITB formation is close to the total heating power in pulses # 49362 and 49654. There is no visible difference in P_{ap} in discharges with NB only and NB plus RF heating. The comparison of discharges with ITBs shows that the diamagnetic energy W_{dia} is initially slightly higher and neutron yield R_{NT} is lower in the pulse with combined heating. The density profiles measured by the Thomson scattering diagnostic are compared in Fig.10.2 for discharges with ITBs (#49362, 49654) and without ITBs (#49443, 49655) before and after ITB formation.

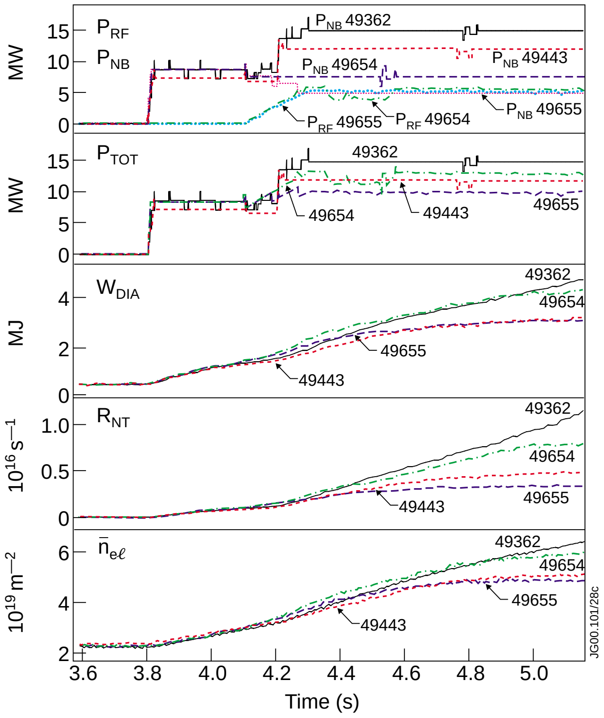

Fig.10.1: Evolution of P_{Rf}, P_{NB}, $P_{tot}= P_{Rf}+ P_{NB}$, W_{dia}, R_{NT} and line integrated density $\overline{n_{el}}$ in OS pulses ## 49362, 49443, 49654, 49655.

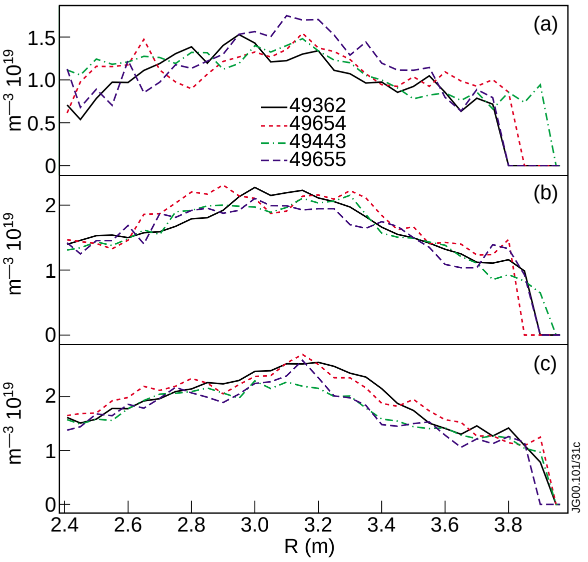

Fig.10.2: Plasma density profiles measured using the Thomson scattering diagnostic in OS pulses ## 49362, 49443, 49654, 49655 before ITB formation at a)t=4.1s b)t=4.6s and after ITB formation c)t=4.9s.

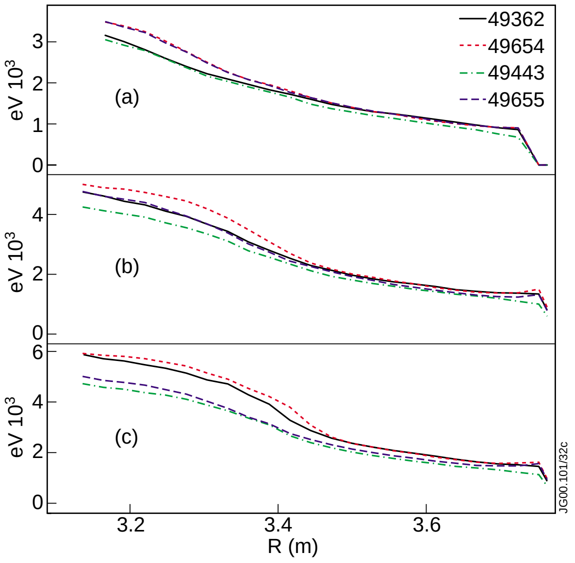

Fig.10.3: Electron temperature profiles measured using heterodyne radiometer in OS pulses ## 49362, 49443, 49654, 49655 before ITB formation at a)t=4.2s b)t=4.5s and after ITB formation c)t=4.8s. 49362-black line, 49654-red line, 49443-green line, 49655-blue line.

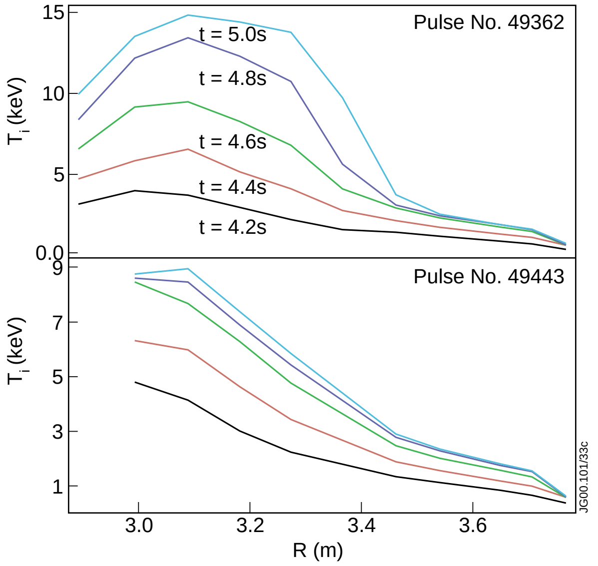

Fig.10.4: Ion temperature profiles measured using charge exchange spectroscopy in OS pulses # 49362, 49443.

The electron temperature profiles measured by heterodyne radiometer are shown for the same pulses in Fig.10.3. Both figs.10.2 and 10.3 show that T_e and n_e profiles steepen after ITB formation in the plasma core. The ion temperature (T_i) profiles are shown in Fig.10.4 for discharge with NB only heating (T_i measurements failed in a discharge with ITB and combined heating). T_i profile steepenning is typical of discharges with an ion ITB.

Observed differences in W_{dia} and R_{NT} for shots with ITBs (#49362, 49654) can be explained by the different electron and ion heating. Figure 10.5 shows the total heating power, P_e and P_i, transferred to electron and thermal ion components respectively.

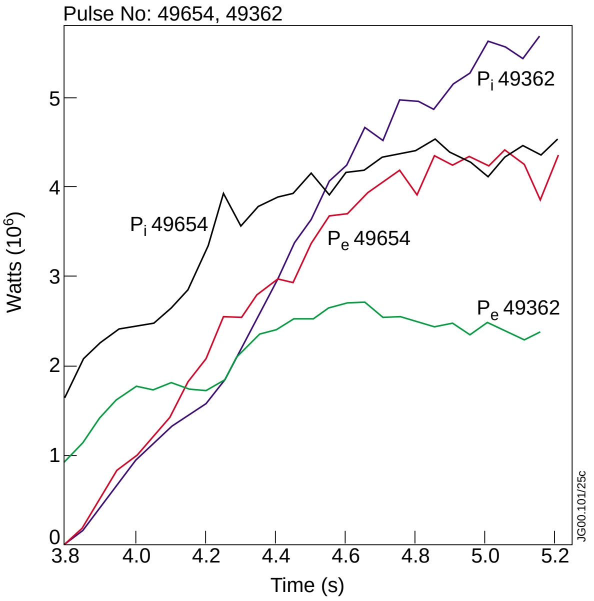

Fig.10.5: Total electron and ion heating power P_e, and P_i, in OS pulses with ITBs # 49362, 49654.

These powers were calculated using TRANSP. It should be noted that T_i from pulse #49362 was used in simulation of discharge #49654. P_e and P_i converge in the discharge with combined NB plus RF heating (#49654). P_e and P_i diverge, on the other hand, in discharge with NBI only heating. Profiles of the electron and ion heating powers are compared in fig.10.6 for discharges with ITBs and with the different heating schemes. The heating is more peaked in discharges with combined heating. Figure 10.7 shows different channels for the RF power absorption for

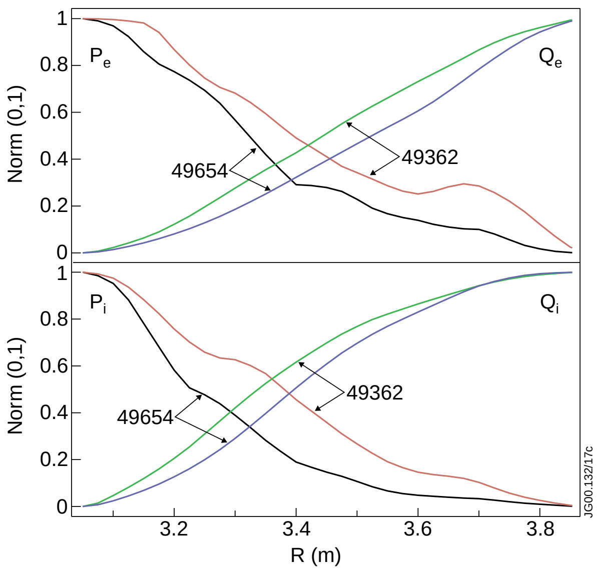

Fig.10.6: Normalised profiles of electron p_e and ion p_i heating power densities in pulses with combined (#49654) and NB only (#49362) heating. $Q_{e,i}=\int p_{e.i}dV$.

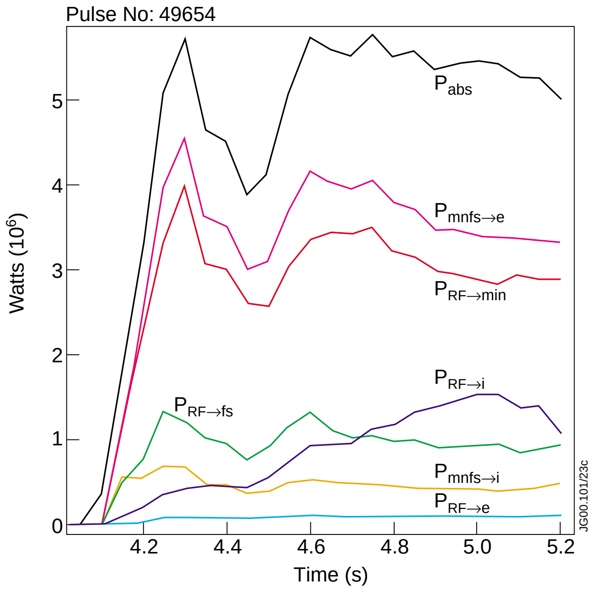

Fig.10.7: RF power absorption and heating channels. P_{abs}-total absorbed RF power, $P_{RF\longrightarrow fs}$ power absorbed by fast deuterium tail, $P_{RF\longrightarrow mn}$-power absorbed by fast hydrogen minority, $P_{Rf\longrightarrow i}$ –power absorbed by thermal ions, $P_{Rf\longrightarrow e}$ –power absorbed by electrons, $P_{mnfs\longrightarrow e}$,-power transferred from fast ions to electrons, $P_{mnfs\longrightarrow i}$-power transferred from fast particles to thermal ions. Pulse #49654 .

pulse #49654. Only a small proportion of the RF power is absorbed by the thermal ions ($P_{Rf\longrightarrow i}$) and electrons ($P_{Rf\longrightarrow e}$). A greater part is transferred to the hydrogen minority ($P_{RF\longrightarrow mn}$) and to the fast deuterium tail ($P_{RF\longrightarrow fs}$) produced by NBI. These powers are subsequently transferred mainly to the electron component ($P_{mnfs\longrightarrow e}$) due to the frictional slowing down of the fast ions (hydrogen and deuterium). A small part ($P_{mnfs\longrightarrow i}$) heats the thermal ion component.

Figure 10.8 shows the perpendicular distribution function for the fast deuterium ions as measured by a neutral particle analysis diagnostic in the pulse with combined NB and RF heating (#49654). Similar measurements have been made for a number of OS pulses. These measurements show that the fast ion tail has characteristic perpendicular temperature around 0.5MeV. The slowing down time for such ions is close to or above 1s for conditions typical of OS discharges in the early phase of the ITB development.

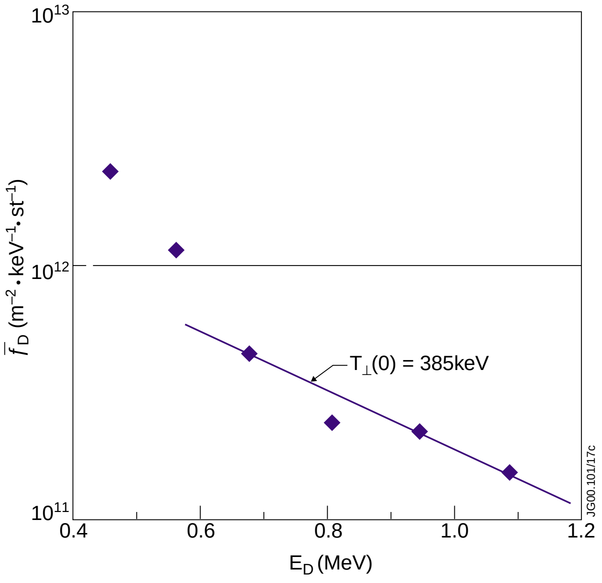

Fig.10.8: Distribution function of the fast deuterium tail measured in the perpendicular to the magnetic field direction using neutral particle analyser. Pulse #49654.

The predominant absorption of RF power by the fast ions can be responsible for several important effects:

- Firstly, fast ions with large perpendicular and comparatively small parallel energy may have wide banana orbits and poor confinement.
- Secondly, the hydrogen minority absorbs the RF power but does not participate in fusion reactions, which decreases the neutron yield.
- Thirdly, the RF power absorbed by the fast particles is transferred mainly to the electron plasma component, which has, in general, poorer confinement than the thermal ion component [10.4]

It should be noted also that W_{dia} should be higher in discharges with combined heating than in discharges with NB only heating, assuming that the total plasma energy W_p is the same. This follows from the fact that $W_p=W_{TH}+W_{fst\perp}+W_{fst//}$ and $W_{dia}= W_{TH}+3/2W_{fst\perp}$, where W_{TH}, $W_{fst\perp}$,$W_{fst//}$ are the thermal plasma energy, perpendicular and parallel fast ion energy respectively. The combined RF and NBI heating causes anisotropy in the fast ion distribution function with $W_{fst\perp}>2W_{fst//}$ [10.4].

2) Statistical analysis

The main goal of the analysis was to compare the plasma fuelling, heating and neutron yield efficiencies for different heating schemes and to deduce the general trends in a wide range of conditions characteristic of OS discharges. Two important time points in the evolution of each discharge have been chosen for the analysis. They correspond to the time of ITB formation t_1 and the maximum of the neutron flux (R_{NT}) t_2, respectively. Only pulses with measured T_i, T_e and n_e and without noble gas puffing have been selected for the analysis. The database comprises 106 pulses.

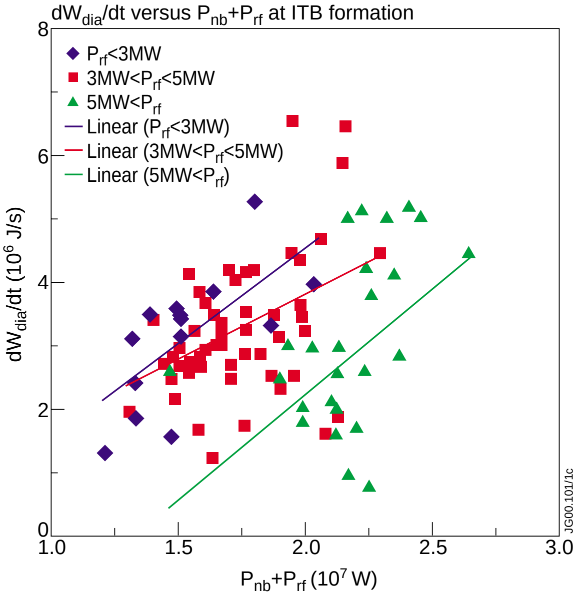

Fig.10.9: dW_{dia}/dt versus $P_{RF}+P_{NB}$ in OS discharges at ITB formation time t_1.The linear trend line is shown as an indication of the centre mass of the cloud of points.

Figure 10.9 shows the dependence of the rate of the diamagnetic energy increment dW_{dia}/dt on the total heating power $P_{RF}+P_{NB}$ at the time of ITB formation t_1.

The RF and NB power are averaged over Δt_{RF} =1s and Δt_{NB}= 0.2s, preceding t_1. The time interval Δt_{RF} and Δt_{NB} are determined by the approximate slowing down times for the fast ions produced by RF and NB power, respectively. Figures 10.10 and 10.11 show the dependence of dW_{i-TH}/dt and dW_e/dt on the heating power at t_1, where W_{i-TH} and W_e are the thermal ion and

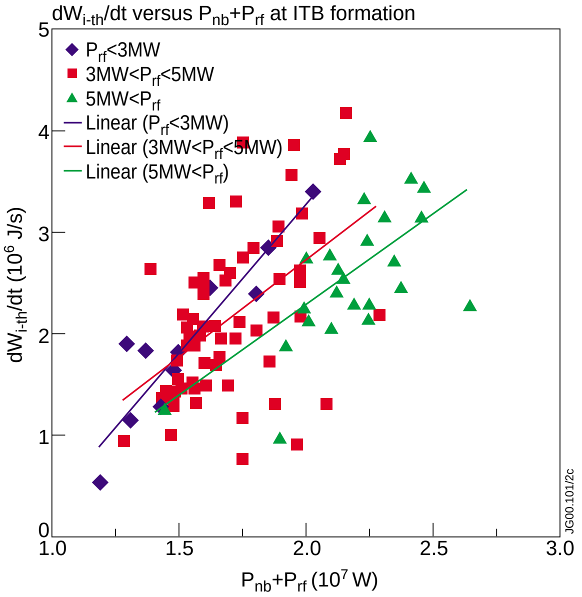

Fig.10.10: dW$_{I-TH}$ /dt versus P$_{RF}$+P$_{NB}$ in OS discharges at ITB formation time t$_1$. The linear trend line is shown as an indication of the centre mass of the cloud of points.

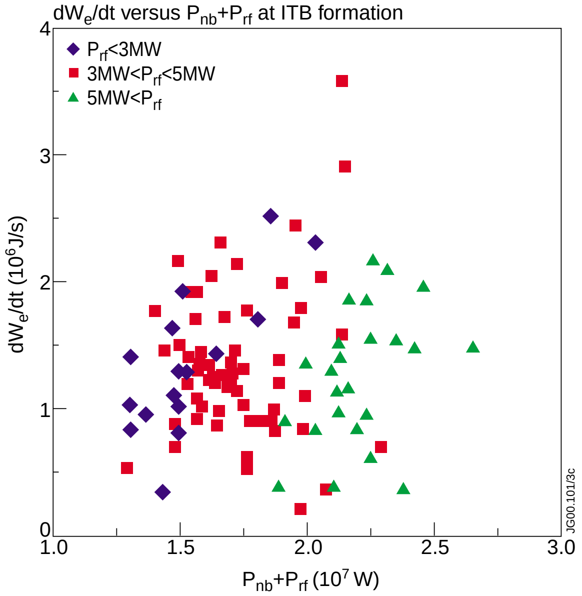

Fig.10.11: dW$_e$ /dt versus P$_{RF}$+P$_{NB}$ in OS discharges at ITB formation time t$_1$.

electron energy, respectively. It is obvious that the plasma heating (for all plasma components) does not simply depend on the total heating power. It varies depending on the ratio P$_{RF}$/P$_{NB}$.

The rate of the plasma fuelling dN$_e$/dt= $\int_{r/a<0.6} (dn_e / dt)dV$ inside r/a<0.6 at the time of ITB formation is shown in fig.10.12 for discharges with different NB power; as expected at a given input power the rate of fuelling increases with the beam power fraction. The rate of the line integrated density change at the time of ITB formation is shown in Figs.10.13 and 10.14 as the

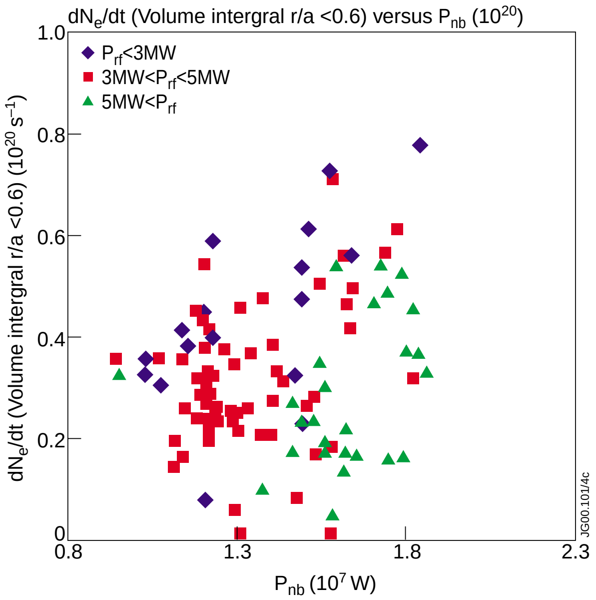

Fig.10.12: dN$_e$ /dt versus P$_{NB}$ in OS discharges at ITB formation time t$_1$.

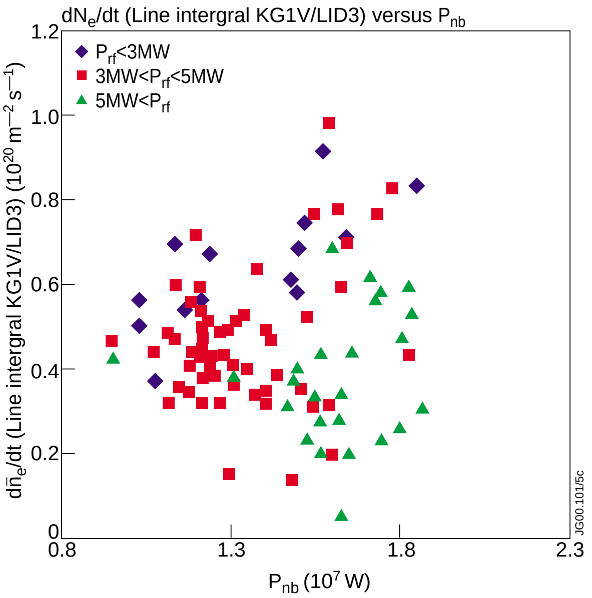

Fig.10.13: d($\overline{n_{el\,1}}$) /dt versus P$_{NB}$ in OS discharges at ITB formation time t$_1$. $\overline{n_{el\,1}}$is the line integrated density measured by interferometer along vertical chord at R=3.02m.

function of NBI power for vertical lines of sight at R=3.02m and 3.74m, respectively. There is a strong decrease in the peripheral density (R≥3.74m) as the ITB forms and this increases for pulses with the highest RF power, as can be seen from Fig.10.14. This effect is demonstrated in Fig.10.15 for pulse #45416. The vertical line indicates the time of ITB formation. A strong decline in the edge line integrated density (KG1V/LID4) shows the decrease in the peripheral density.

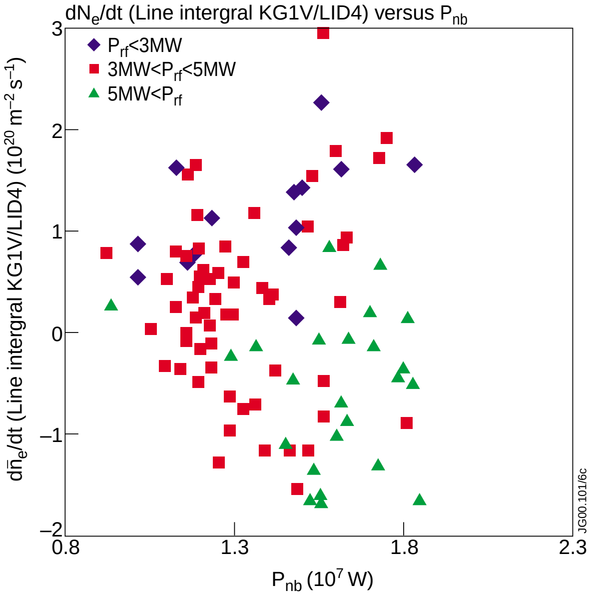

Fig.10.14: d($\overline{n_{el\,2}}$) /dt versus P_{NB} in OS discharges at ITB formation time t_1. $\overline{n_{el2}}$ is the line integrated density measured by interferometer along vertical chord at R=3.74m.

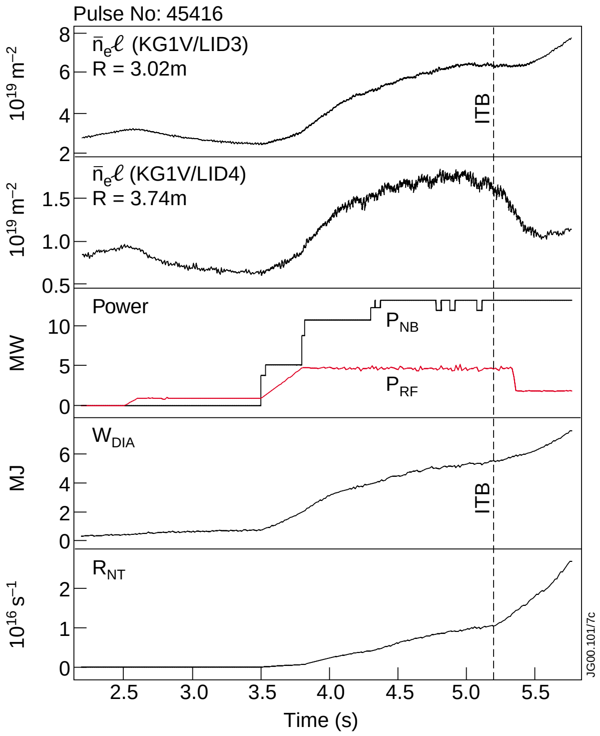

Fig.10.15: Variation of the main plasma parameters. Pulse#45416.

Figure 10.16 shows the total heating power as the function of the ratio P_{RF}/P_{NB} in OS discharges at $t_{1.}$ The upper boundary for $P_{tot}=P_{RF}+P_{NB}$ is determined by operational limit (maximum available power, choice of the power waveform). The lower boundary indicates the ITB power access limit P_{ap}. It should be noted that P_{ap} does not depend, practically, on the ratio of P_{RF}/P_{NB} at B_o=2.5T. For the higher magnetic field, it is impossible to make a conclusion concerning the dependence of P_{ap} on P_{RF}/P_{NB} as the database covers too narrow range of P_{RF}/P_{NB}.

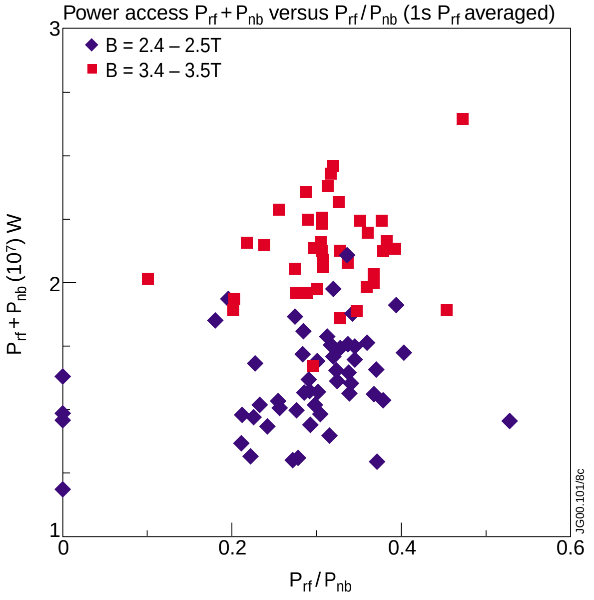

Fig.10.16: P_{RF}+P_{NB} versus P_{RF}/P_{NB} at ITB formation time t_1 in OS discharges. P_{RF} is averaged over 1s.

The velocity of the toroidal rotation V_{tor} at the location of the ion ITB is shown in Figs.10.17 and 10.18 as a function of $P_{RF}+P_{NB}$ and P_{NB}, respectively. These figures show V_{tor} at the time of ITB formation t_1. The location of ITB is defined as the location of the max(dP_i /dR)), where P_i is the thermal ion pressure and R is the major radius. V_{tor} is insensitive to the total heating power, depending as expected dominantly on beam power.

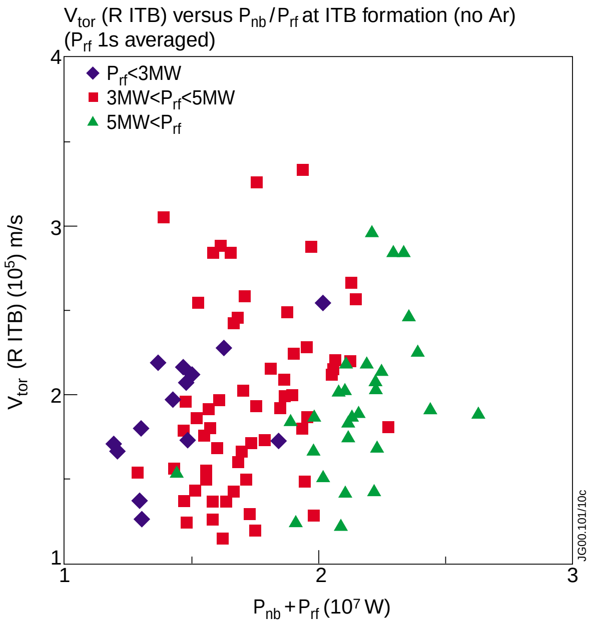

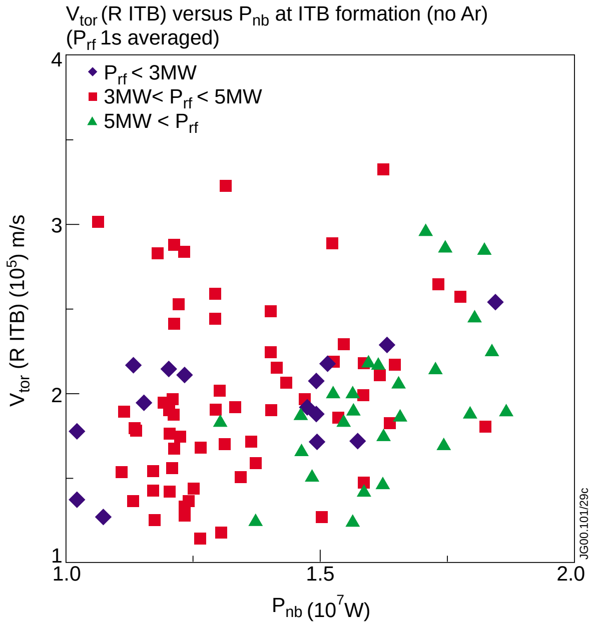

Fig.10.17: V_{tor} as a function of $P_{RF}+P_{NB}$ at ITB formation time t_1 in OS discharges.

Fig.10.18: V_{tor} as a function of P_{NB} at ITB formation time t_1 in OS discharges.

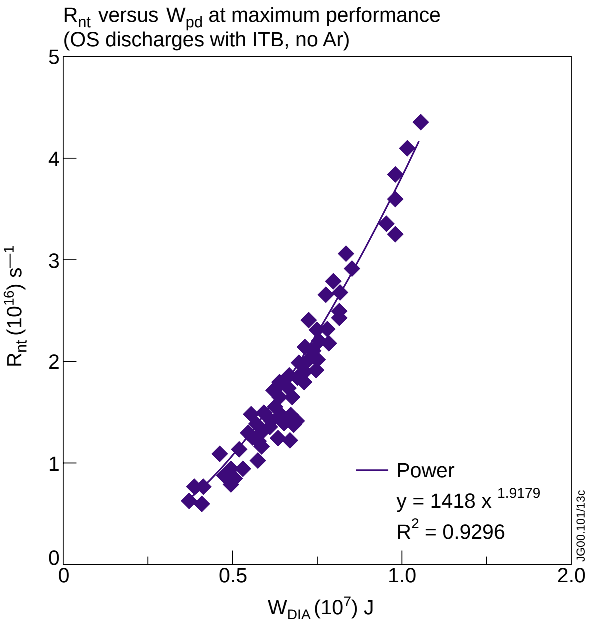

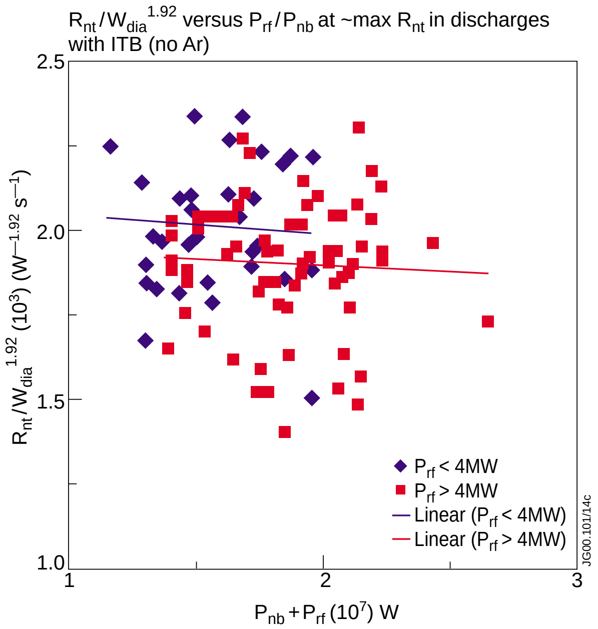

Fig.10.19: Dependence of R_{NT} on W_{dia} in OS discharges at maximum R_{NT} time t_2.

*Fig.10.20: R_{NT} / W_{dia}**1.92 versus $P_{RF}+P_{NB}$ in OS discharges at maximum R_{NT} time t_2.*

The dependence of the neutron yield R_{NT} on the plasma diamagnetic energy W_{dia} is shown in Fig.10.19 at the time t_2, when R_{NT} reaches its maximum value. Statistical analysis shows that R_{NT} is proportional to W_{dia}**1.92 with the correlation coefficient (square of the Pearson product moment) R=0.93. Figure 10.20, shows that the ratio R_{NT}/Wdia**1.92 is slightly higher for dominantly beam heated discharges. Figure 10.21 shows the dependence of R_{NT}/Wdia**1.92 on the ratio W_{fast}/W_{TH} at t_2 (time of peak neutron flux), where W_{TH} and W_{fast} are the thermal plasma energy and diamagnetic energy of the fast particles $W_{fast}=W_{dia}-W_{TH}$, respectively.

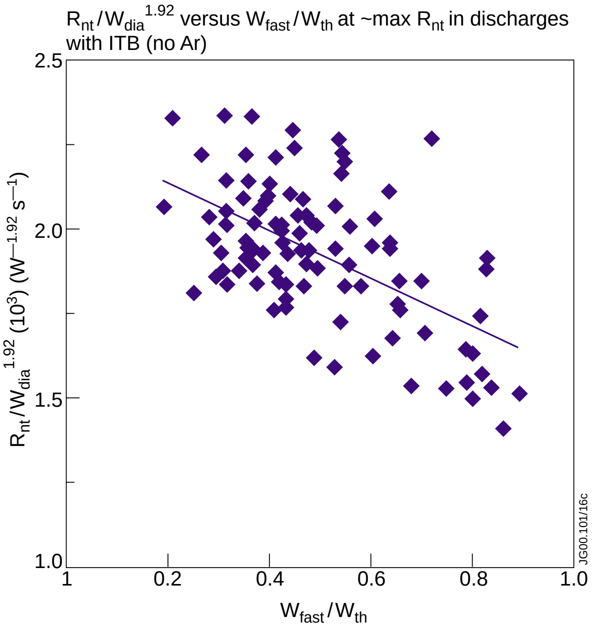

*Fig.10.21: R_{NT} / W_{dia}**1.92 versus W_{fast} /W_{TH} in OS discharges at maximum R_{NT} time t_2.*

W_{dia} , $W_{i\text{-}TH}$ and W_e are shown versus P_{tot} at t_2 in Figs.10.22, 10.23 and 10.24, respectively. Little difference in stored energy is observed for different power fractions.

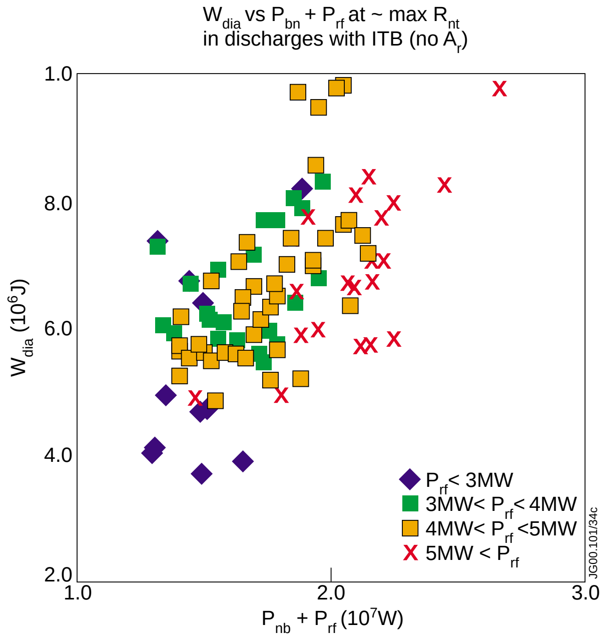

Fig.10.22: W_{dia} versus P_{RF} +P_{NB} in OS discharges at maximum R_{NT} time t_2.

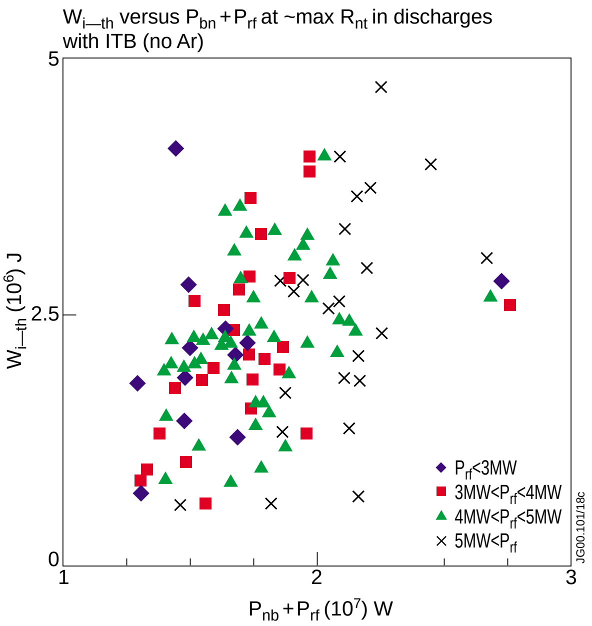

Fig.10.23: $W_{i\text{-}TH}$ versus P_{RF} +P_{NB} in OS discharges at maximum R_{NT} time t_2.

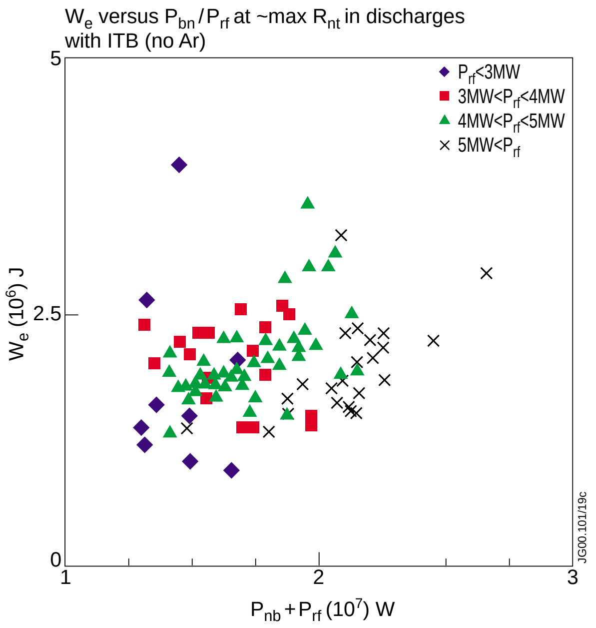

Fig.10.24: W_e versus P_{RF} +P_{NB} in OS discharges at maximum R_{NT} time t_2.

10.3 Summary

An experiment dedicated to the direct comparison of RF and NBI heating schemes has been performed at a fixed magnetic field B=2.6T and maximum plasma current I_p=2.5MA. The total heating power P_{NB}+P_{RF} was limited to 15MW in the experiment and P_{RF} did not exceed 5.5MW.

The evolution of the neutron yield and the diamagnetic energy are similar in discharges with different heating schemes, provided that the power waveforms are identical. The electron ITB was observed in NBI only and NBI plus RF heating discharges with very similar power waveforms. The ion ITB was observed in the experiment in discharges with NBI only heating. The ion temperature measurements failed in the series of pulses with combined NBI plus RF heating. Nevertheless, the neutron yield evolution indicates that the ion ITB has been also obtained in the equivalent discharges with a combined heating. The plasma density peaking was observed in discharges with NBI only and NBI plus RF heating with ITBs. It has been found that the ITB formation power threshold is very similar in discharges with different heating schemes.

There are subtle differences between discharges with ITB produced by NBI only and with combined heating. The diamagnetic energy and the electron temperature are slightly higher and the neutron yield is slightly lower in the combined heating case compared with NBI only heating, provided that the total power is the same. A simulation of the plasma heating and the heat transport using the TRANSP and PION codes provides the following explanation for the differences.

Modelling of RF heating shows that significant proportion (60%-70%) of the RF power is absorbed by the hydrogen minority tail. The heating increases predominantly the perpendicular velocity (with respect to the magnetic field). The hydrogen minority does not participate in fusion reaction and does not contribute to the fusion yield. The fast deuterium tail produced by NBI absorbs about 15-20% of the RF power. The fast deuterium population increases the plasma reactivity. The ion distribution function of the fast ions (both, hydrogen and deuterium) is anisotropic with the perpendicular component dominant. The diamagnetic energy is larger in discharges with the higher anisotropy. The characteristic tail temperature is of the order of 0.5MeV. This is confirmed by a direct measurement of the fast deuterium distribution function in discharges with RF heating. The typical slowing down time for the fast ions is of the order of 1s. The energy from the fast ions is transferred mainly to the electron component due to frictional slowing down.

The results of the statistical analysis should be treated with a great caution. Trends and tendencies shown in figures10.9-10.24 are often unclear. There is a large scattering of points in each graph. These facts indicate that there are hidden parameters in each dependency. Bearing this in mind the most general conclusions can be formulated.

At the time of ITB formation:

- $d(W_{dia})/dt$, $d(W_{i\text{-}TH})/dt$ and $d(W_e)/dt$ do not increase simply as a function of P_{tot}. They are also functions of P_{RF}/P_{NB}.
- As the ITB forms there is a clear reduction in edge density and this reduction increases with RF power. This could be due to improved particle confinement as the RF power fraction increases, though it appears the confinement degrades with increased RF power fraction.
- There is no significant increase in ITB access power with increase of P_{RF}/P_{NB} at B= 2.5T. (There is also no indication of a dependence at B=3.4T).
- $V_{tor}(R_{ITB})$ does not increase simply with P_{tot}, it is mainly a function of P_{NB}.

At the time of maximum performance (max R_{NT}):

- R_{NT} is proportional to W_{dia}**1.9 in OS discharges with ITB with the correlation coefficient (square of the Pearson product moment) R=0.93.
- The averaged R_{NT}/W_{dia}**1.9 decreases as W_{fast}/W_{TH} increased. This effect can be explained by significant absorption of RF power by fast hydrogen minority.

  There may be a reduction in W_{dia} reached in discharges with the highest $P_{RF} \geq 5$MW. Possible explanation: fast ion tail produced by RF heats mostly electrons, which are not confined as well as the thermal ions. This is supported by the dependence of W_e on P_{tot} and P_{RF}.

Further experiments dedicated to the direct comparison of different heating schemes are required. It is necessary to increase the ratio of P_{RF}/P_{NB}. ITBs have been produced in the dedicated experiment in regimes, when P_{tot} was close to that of P_{ap}. ITBs were relatively weak. An increase of P_{tot} should improve the quality of the ITBs. It is crucial to produce ITBs in regimes with the combined RF and NBI heating at higher plasma density and the ion temperature. This would decrease the heating of the fast particles in general and the hydrogen minority in particular. As a consequence, the electron and the thermal ion heating could be relatively smaller and greater, respectively. Only a limited number of pulses have been done so far to verify the importance of the power deposition profile.

10.4 Shot lists

The experiment on a direct comparison of NBI and RF heating in OS discharges includes 27 pulses. It has been performed at B=2.6T and I_p=2.5MA. The list of shots is shown in table 1 with short comments.

Table 10.1: Shots used for analysis of NBI versus RF heating

Pulse	Comments
49192	NBI only, rough timing scan and power waveform adjustment
49193	NBI only, rough timing scan and power waveform adjustment
49195	NBI only, rough timing scan and power waveform adjustment
49196	NBI only, rough timing scan and power waveform adjustment
49197	NBI only, rough timing scan and power waveform adjustment, strong ITB, disruption
49199	NBI only, rough timing scan and power waveform adjustment
49200	NBI only, rough timing scan and power waveform adjustment
49203	NBI only, rough timing scan and power waveform adjustment
49340	NBI only, rough timing scan and power waveform adjustment, ITB at 44.3s
49342	NBI only, rough timing scan and power waveform adjustment, ITB at 44.3s
49344	NBI only, rough timing scan and power waveform adjustment
49345	NBI only, rough timing scan and power waveform adjustment, weak ITB at 44.4s
49346	NBI only, rough timing scan and power waveform adjustment
49359	NBI only, rough timing scan and power waveform adjustment, ITB at 44.5s
49362	NBI only, rough timing scan and power waveform adjustment, ITB at 44.4s, disruption
49365	repeat 49362, weak ITB
49366	NBI only, like #49197, power scan
49367	NBI only, like #49197, power scan, weak ITB
49368	NBI only, like #49197, power scan
49369	ICRH plus NBI waveform adjustment
49370	ICRH plus NBI waveform adjustment
49443	NBI only, like #49197, power scan, below power threshold
49444	NBI only, like #49197, power scan, below power threshold
49445	NBI only, like #49197, power scan, below power threshold
49447	ICRH plus NBI, waveform adjustment, like 49197, below power threshold
49652	ICRH plus NBI, waveform adjustment, like 49197, below power threshold
49654	ICRH plus NBI, waveform adjustment, like 49197, electron ITB, no Ti measurements
49655	ICRH plus NBI, waveform adjustment, like 49197, no ITB, no Ti measurements

Table 10.2 shows the list of pulses include in the database for a statistical analysis.

Table 10.2: List of 105 shots used for statistical analysis in this chapter

SHOT	TF (T)	Ip(MA)	P_{tot}(W)	W_{dia}(J)	H_{97}	P_{RF}/P_{NBI}	P_{NBI}(W)	P_{RF}(W)	R_{nt}
45380	2.58	2.48	2.56E+07	5.09E+06	1.29	2.75E-01	1.47E+07	4.06E+06	1.08E+16
45383	2.58	2.44	1.89E+07	5.08E+06	1.81	3.16E-01	1.36E+07	4.29E+06	1.01E+16
45388	2.42	2.11	1.72E+07	4.16E+06	1.85	2.33E-01	1.23E+07	2.86E+06	6.09E+15
45389	2.42	2.15	1.40E+07	3.64E+06	1.76	2.23E-01	1.07E+07	2.39E+06	4.76E+15
45400	2.52	2.14	1.49E+07	3.84E+06	1.84	2.74E-01	1.02E+07	2.79E+06	4.76E+15
45403	2.51	2.13	1.51E+07	3.72E+06	1.70	2.83E-01	1.02E+07	2.88E+06	4.54E+15
45404	2.57	2.41	1.65E+07	4.65E+06	1.90	3.80E-01	1.11E+07	4.22E+06	7.85E+15
45414	2.52	2.16	1.48E+07	3.90E+06	1.79	3.73E-01	9.37E+06	3.50E+06	4.41E+15
45416	2.57	2.53	1.92E+07	5.48E+06	1.85	3.62E-01	1.29E+07	4.66E+06	1.09E+16
45421	2.52	2.16	1.65E+07	4.31E+06	1.90	3.07E-01	1.13E+07	3.47E+06	6.61E+15
45426	2.52	2.26	1.78E+07	4.57E+06	1.92	3.71E-01	1.14E+07	4.21E+06	8.35E+15
45542	2.43	2.16	1.76E+07	4.23E+06	1.94	2.14E-01	1.22E+07	2.60E+06	7.23E+15
45546	2.43	2.12	1.66E+07	3.82E+06	1.74	2.10E-01	1.13E+07	2.38E+06	4.52E+15
45547	2.43	2.17	1.60E+07	4.58E+06	2.00	2.44E-01	1.15E+07	2.80E+06	7.22E+15
45550	2.48	2.16	1.69E+07	4.39E+06	1.90	2.96E-01	1.11E+07	3.28E+06	7.34E+15
45555	2.47	2.18	1.76E+07	4.27E+06	1.76	3.00E-01	1.17E+07	3.52E+06	6.86E+15
45558	2.48	2.17	1.78E+07	4.41E+06	1.81	3.42E-01	1.17E+07	3.99E+06	8.04E+15
45564	2.47	2.18	1.67E+07	4.28E+06	1.79	3.06E-01	1.13E+07	3.45E+06	7.07E+15
45565	2.47	2.19	1.62E+07	4.18E+06	1.78	2.88E-01	1.22E+07	3.50E+06	7.29E+15
45575	2.47	2.30	1.86E+07	4.73E+06	1.85	3.30E-01	1.31E+07	4.34E+06	9.27E+15
45582	2.47	2.26	1.77E+07	4.82E+06	1.95	3.28E-01	1.21E+07	3.95E+06	9.08E+15
45585	2.47	2.14	1.62E+07	4.10E+06	1.77	2.59E-01	1.19E+07	3.08E+06	6.56E+15
45586	2.47	2.21	1.71E+07	4.51E+06	1.86	3.06E-01	1.20E+07	3.68E+06	8.32E+15
45587	2.47	2.27	1.77E+07	4.82E+06	1.93	3.25E-01	1.25E+07	4.07E+06	9.61E+15
45592	2.47	2.25	1.75E+07	4.56E+06	1.84	3.31E-01	1.21E+07	4.00E+06	8.34E+15
45593	2.47	2.29	1.79E+07	4.85E+06	1.82	3.49E-01	1.26E+07	4.38E+06	9.66E+15
45622	3.45	2.72	2.31E+07	4.57E+06	1.46	1.99E-01	1.58E+07	3.15E+06	5.49E+15
45623	3.45	2.72	2.13E+07	5.90E+06	1.73	2.75E-01	1.61E+07	4.44E+06	1.24E+16
45627	3.45	2.87	1.80E+07	6.47E+06	1.90	3.66E-01	1.46E+07	5.34E+06	1.67E+16
45628	3.45	2.86	1.79E+07	6.19E+06	1.84	3.51E-01	1.40E+07	4.93E+06	1.48E+16
45632	3.45	2.89	2.29E+07	6.67E+06	1.75	3.57E-01	1.65E+07	5.88E+06	1.77E+16
45633	3.45	2.93	2.12E+07	6.90E+06	1.79	3.63E-01	1.61E+07	5.85E+06	1.79E+16
45635	3.45	2.69	2.42E+07	5.88E+06	1.70	2.36E-01	1.73E+07	4.10E+06	1.17E+16
45643	3.45	2.84	2.24E+07	5.57E+06	1.58	2.79E-01	1.54E+07	4.29E+06	9.02E+15
45644	3.45	2.90	2.30E+07	7.15E+06	1.83	3.10E-01	1.72E+07	5.33E+06	1.88E+16
45666	2.48	2.56	1.34E+07	6.21E+06	2.22	2.93E-01	1.26E+07	3.69E+06	1.43E+16
45670	2.47	2.25	1.83E+07	4.81E+06	1.84	3.02E-01	1.30E+07	3.94E+06	8.24E+15
45672	2.48	2.14	1.63E+07	4.00E+06	1.74	2.29E-01	1.20E+07	2.73E+06	4.91E+15
45673	2.47	2.17	1.69E+07	4.51E+06	1.92	2.76E-01	1.17E+07	3.24E+06	6.80E+15
45817	2.47	2.18	1.78E+07	4.40E+06	1.82	2.93E-01	1.21E+07	3.55E+06	7.05E+15
45831	2.81	2.46	1.91E+07	4.83E+06	1.81	3.63E-01	1.17E+07	4.25E+06	1.00E+16
45839	2.49	2.15	1.76E+07	4.53E+06	1.93	2.99E-01	1.20E+07	3.59E+06	7.25E+15

SHOT	TF (T)	Ip(MA)	P_{tot}(W)	W_{dia}(J)	H_{97}	P_{RF}/P_{NBI}	P_{NBI}(W)	P_{RF}(W)	R_{nt}
45842	2.50	2.19	2.00E+07	4.87E+06	1.90	3.20E-01	1.33E+07	4.26E+06	9.24E+15
45860	2.47	2.22	2.23E+07	5.34E+06	2.09	1.94E-01	1.63E+07	3.17E+06	1.04E+16
45867	2.48	2.26	2.01E+07	5.44E+06	2.07	3.44E-01	1.40E+07	4.83E+06	1.14E+16
45876	2.47	2.33	1.79E+07	5.89E+06	2.33	3.40E-01	1.31E+07	4.45E+06	1.29E+16
45877	2.51	2.28	1.92E+07	5.74E+06	2.24	3.39E-01	1.21E+07	4.10E+06	1.20E+16
45882	2.39	2.27	1.88E+07	5.85E+06	2.33	3.24E-01	1.29E+07	4.19E+06	1.10E+16
45885	2.48	2.18	1.84E+07	4.64E+06	2.04	2.58E-01	1.21E+07	3.11E+06	7.66E+15
45886	2.47	2.27	1.80E+07	5.53E+06	2.15	3.47E-01	1.18E+07	4.10E+06	1.04E+16
45887	2.47	2.18	1.90E+07	4.65E+06	1.95	2.57E-01	1.22E+07	3.13E+06	6.59E+15
45906	2.48	2.13	1.57E+07	4.41E+06	2.02	3.17E-01	1.06E+07	3.38E+06	7.20E+15
45907	2.41	2.18	1.78E+07	4.79E+06	2.12	3.06E-01	1.20E+07	3.67E+06	8.39E+15
46048	3.45	2.13	1.64E+07	3.98E+06	1.61	2.99E-01	1.29E+07	3.86E+06	4.99E+15
46049	3.45	2.17	2.18E+07	4.85E+06	1.69	3.01E-01	1.52E+07	4.57E+06	7.45E+15
46050	3.45	2.35	2.27E+07	5.72E+06	1.87	3.80E-01	1.62E+07	6.13E+06	1.22E+16
46052	3.45	2.37	2.06E+07	5.81E+06	1.76	2.90E-01	1.74E+07	5.04E+06	1.34E+16
46087	2.48	2.22	1.74E+07	5.07E+06	2.12	2.94E-01	1.23E+07	3.62E+06	1.09E+16
46091	2.47	2.31	1.78E+07	5.77E+06	2.26	3.48E-01	1.30E+07	4.51E+06	1.36E+16
46092	2.48	2.26	1.89E+07	5.29E+06	2.12	3.41E-01	1.23E+07	4.20E+06	1.12E+16
46095	2.47	2.27	1.78E+07	5.14E+06	2.10	3.27E-01	1.24E+07	4.06E+06	1.18E+16
46099	2.48	2.27	2.05E+07	5.25E+06	1.91	2.86E-01	1.41E+07	4.04E+06	1.14E+16
46101	2.48	2.43	1.84E+07	6.06E+06	2.26	3.23E-01	1.50E+07	4.84E+06	1.57E+16
46119	2.47	2.26	1.85E+07	4.87E+06	2.06	2.29E-01	1.37E+07	3.13E+06	9.44E+15
46384	3.44	3.29	2.90E+07	8.84E+06	1.84	4.76E-01	1.79E+07	8.54E+06	2.58E+16
46510	3.45	2.71	2.40E+07	5.92E+06	1.76	2.15E-01	1.77E+07	3.81E+06	1.09E+16
46616	3.46	2.80	2.21E+07	6.80E+06	1.81	3.31E-01	1.59E+07	5.26E+06	1.70E+16
46621	3.46	2.75	1.93E+07	6.66E+06	1.90	2.99E-01	1.64E+07	4.89E+06	1.68E+16
46623	3.45	2.90	1.78E+07	6.41E+06	1.71	3.14E-01	1.58E+07	4.94E+06	1.47E+16
46627	3.45	3.09	1.79E+07	7.24E+06	1.83	3.10E-01	1.62E+07	5.03E+06	1.99E+16
46636	3.45	2.78	2.05E+07	5.50E+06	1.66	1.03E-01	1.84E+07	1.89E+06	1.19E+16
46637	3.45	3.01	1.90E+07	6.86E+06	1.88	2.90E-01	1.53E+07	4.44E+06	1.79E+16
46642	3.45	3.03	1.85E+07	7.55E+06	2.03	3.38E-01	1.56E+07	5.29E+06	2.11E+16
46649	3.45	3.10	2.50E+07	8.47E+06	2.08	3.17E-01	1.83E+07	5.82E+06	2.75E+16
46654	3.45	3.03	2.48E+07	7.41E+06	1.81	2.89E-01	1.82E+07	5.26E+06	1.79E+16
46660	3.45	2.89	2.04E+07	6.59E+06	1.91	2.01E-01	1.62E+07	3.27E+06	1.66E+16
46663	3.45	2.96	2.41E+07	6.98E+06	1.80	2.56E-01	1.82E+07	4.66E+06	1.72E+16
46664	3.45	3.02	2.37E+07	6.86E+06	1.81	3.06E-01	1.65E+07	5.07E+06	1.60E+16
46669	3.45	3.10	1.75E+07	7.36E+06	1.94	3.79E-01	1.54E+07	5.83E+06	1.87E+16
46676	3.45	2.95	2.54E+07	7.15E+06	1.83	3.29E-01	1.74E+07	5.72E+06	1.78E+16
46697	3.45	3.13	1.78E+07	7.44E+06	1.65	3.95E-01	1.52E+07	6.00E+06	2.06E+16
46699	3.45	3.13	1.83E+07	7.12E+06	1.90	3.83E-01	1.56E+07	5.97E+06	1.83E+16
46716	3.45	3.02	2.48E+07	7.29E+06	1.70	3.16E-01	1.80E+07	5.68E+06	1.79E+16
46717	3.45	3.13	1.70E+07	6.33E+06	1.74	3.64E-01	1.46E+07	5.32E+06	1.34E+16
46722	3.45	3.16	2.40E+07	7.34E+06	1.76	3.07E-01	1.70E+07	5.23E+06	1.87E+16
46727	3.45	3.01	1.69E+07	6.38E+06	1.89	3.32E-01	1.40E+07	4.64E+06	1.46E+16
46890	3.45	3.04	1.98E+07	6.00E+06	1.59	4.55E-01	1.30E+07	5.92E+06	9.96E+15

SHOT	TF (T)	Ip(MA)	P_{tot}(W)	W_{dia}(J)	H_{97}	P_{RF}/P_{NBI}	P_{NBI}(W)	P_{RF}(W)	R_{nt}
46946	3.45	2.95	2.25E+07	6.57E+06	1.74	3.68E-01	1.48E+07	5.45E+06	1.30E+16
47040	2.98	2.48	2.05E+07	4.85E+06	1.75	1.88E-01	1.51E+07	2.83E+06	7.45E+15
47061	2.99	2.68	2.01E+07	6.12E+06	1.95	2.98E-01	1.43E+07	4.25E+06	1.40E+16
47332	3.36	3.43	1.97E+07	6.63E+06	1.61	2.39E-01	1.58E+07	3.78E+06	1.29E+16
47432	3.46	3.13	2.60E+07	7.81E+06	1.90	3.19E-01	1.86E+07	5.95E+06	2.25E+16
48907	2.57	2.11	1.96E+07	4.80E+06	1.87	1.81E-01	1.57E+07	2.84E+06	8.31E+15
48912	2.57	2.30	1.83E+07	5.25E+06	2.06	3.70E-01	1.21E+07	4.48E+06	1.10E+16
48965	2.57	2.57	2.12E+07	6.28E+06	1.74	3.37E-01	1.58E+07	5.32E+06	1.32E+16
48969	2.58	2.53	1.93E+07	6.07E+06	1.87	3.42E-01	1.56E+07	5.35E+06	1.14E+16
48971	2.58	2.34	1.96E+07	5.48E+06	2.04	3.98E-01	1.37E+07	5.44E+06	9.98E+15
48988	2.57	2.19	2.08E+07	5.06E+06	1.52	2.87E-01	1.34E+07	3.84E+06	1.11E+16
48993	2.57	2.09	1.56E+07	4.00E+06	1.81	5.34E-01	9.46E+06	5.06E+06	5.68E+15
48994	2.57	2.17	1.77E+07	4.90E+06	2.14	4.05E-01	1.23E+07	4.98E+06	9.82E+15
49196	2.57	2.11	1.74E+07	3.54E+06	1.60	0.00E+00	1.63E+07	0.00E+00	5.90E+15
49197	2.57	2.08	1.40E+07	3.02E+06	1.47	0.00E+00	1.49E+07	0.00E+00	4.59E+15
49200	2.57	2.30	1.65E+07	3.80E+06	1.55	0.00E+00	1.49E+07	0.00E+00	6.27E+15
49359	2.57	2.13	1.50E+07	3.43E+06	1.52	0.00E+00	1.47E+07	0.00E+00	5.68E+15
49362	2.58	2.11	1.56E+07	3.29E+06	1.53	0.00E+00	1.49E+07	0.00E+00	5.43E+15
49367	2.57	2.15	1.29E+07	2.95E+06	1.42	0.00E+00	1.20E+07	0.00E+00	4.42E+15

References

[10.1] Goldston, R.J., et al, J.Comput.Phys. 43 (1981) 61, Goldston, R.J., in Basic Processes of Toroidal Fusion Plasmas 1986 (Proc. Course and Workshop, Varenna, 1985) Vol. 1, CEC Brussels (1986) 165.

[10.2] Budny, R.V., et al., Nucl.Fusion 32 (1992) 429.

[10.3] L.-G.Ericsson, et al., Nucl.Fusison 33 (1993) 1037.

[10.4] Y.Baranov, et al., Nucl.Fusion 39 (1999) 1463

11. ACCESS POWER STUDIES

V. Parail[1], B. Alper[1], Y. Baranov[1], C.Challis[1], G. Cottrell[1], C. Gormezano[2], C. Gowers, [1] N. Hawkes[1], T. C Hender[1], P.J Lomas[1], J. Mailloux[1], M.F Stamp[1], K-D. Zastrow[1].

JET Joint Undertaking, Abingdon, Oxon, OX14 3EA, UK
[1] EURATOM/UKAEA Fusion Association, Culham Science Centre, Abingdon, Oxon, OX14 3DB, UK
[2] ENEA/EURATOM Association, P.O. Box 65, I-00044, Frascati (Rome), Italy.

11.1 Overview.

The JET Optimised Shear (OS) regime exhibits, amongst other conditions, a heating power threshold for the formation of a good quality Internal Transport Barrier (ITB). Some results of the power threshold dependence on toroidal magnetic field have been reported previously [11.1].

An extensive database of more than 250 OS plasmas with different power level, heating scheme and current profile control has been formed and used to determine the conditions for ITB formation. The results of the database analysis will be presented which confirm an important role of access power and other key plasma parameters. Some conclusion could also be drawn on how power threshold depends on the heating scheme (NBI and ICRH) and plasma fuelling (provided mainly by NBI).

JET experiments have also shown that although access power is an important parameter, which controls the production of the ITB, it is not unique. Magnetic configuration, particularly q-profile and magnetic shear, are also important for the ITB formation. This subject will be discussed in details in Section 8 (ITBs Produced with LHCD Preheating).

11.2 Access Power Database.

Experiments, carried out during 1999 experimental campaign, resulted in the creation of a large database (with about 250 shots), which includes ITB scenarios with the heating power restricted to a relatively narrow range around the previously reported power threshold for ITB formation [11.1]. The database covers discharges within a wide range of toroidal magnetic field from B_T=1.8 T to B_T=4 T with a particularly good statistics around B_T=2.6 T. However, to make the analysis tractable the number of pulses in the database has had to be limited by not including pulses with power well above the threshold (this notably occurs for 2.6T pulses).

The shot-list is summarised in Table 1, which also includes some relevant plasma parameters and comments. First of all, some explanation is required concerning the procedure which has been used to identify if ITB was presented in the shot (see the column ITB (Y/N)). Our conclusion was based not on automated procedure of any kind but rather on some subjective expert opinion. To put it simply, we watched the time evolution of some characteristic plasma parameters, like electron and/or ion temperature profile (measured by heterodyne radiometer KK3 and CX spectroscopy).

We conclude, that the ITB has been formed, if the distance between two neighbouring T_e or T_i signals rises faster that usually, so that a region with strong temperature gradient develops. It is worth mentioning however, that this method is quite sensitive and allows us to determine the formation of even weak ITB, which does not lead to a significant improvement in plasma performance. In this sense, situation with the ITB threshold is similar to that of L-H transition- weak L-H transition leads to type III ELMs (and poor performance). Further increase in heating power transforms type III into type I ELM with subsequent increase in performance.

We also try to associate the ITB formation with the evolution of some other global characteristics. This includes:

- Energy confinement time rise (expressed in term of enhancement over ITER-97 scaling low) above certain level (it should be noted however, that this level is not universal, but rather dependant on plasma current);
- We also tried to construct some other global characteristics, which might be used as an indicator of the ITB emergence. One possibility would be to use a ratio of the neutron yield (TIN/RNT) over square of the plasma energy content (MG3/WPD). We call this parameter the discharge “quality”: $Q \equiv \dfrac{R_{NT}(neut/\sec)}{300 \cdot \left[W_{PD}(J)\right]^2}$.

Generally, $Q>1$indicates that discharge either got an ITB or develops an ELM-free H-mode. Again, this parameter is not universal since it depends on the composition of the heating power (NBI produces more neutrons than ICRH).

Some preliminary results of the database analysis are shown on the Figs.11.1-11.4.

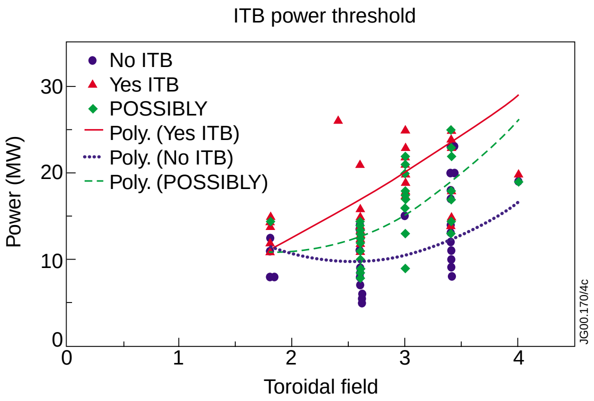

Fig.11.1: Correlation between access power, necessary for the ITB formation, and toroidal magnetic field (red triangles- discharges with ITB, blue diamonds- discharges without ITB)

First of all, one can see from the Fig.11.1, that there is a clear correlation between access power, which is necessary for the ITB formation, and the toroidal magnetic field. It is worth mentioning here, that due to the correlation between toroidal field and plasma current we can not draw any conclusion on the relative importance of poloidal or toroidal magnetic field.

Figure 11.2 shows the correlation between development of the ITB and the level of achieved enhancement in the energy confinement time. Again, we can claim that there is a correlation between these two parameters, although this correlation is not very clear in some cases (particularly for the best-documented series of discharges with 2.6 T toroidal field). We could also conclude that the discharges with the toroidal field within the range 2.6T<B_T<3.4T only have good enough statistics (although there is not enough pulses without ITB in 3T range). Discharges with B_T=1.8T and 4T have very poor statistics.

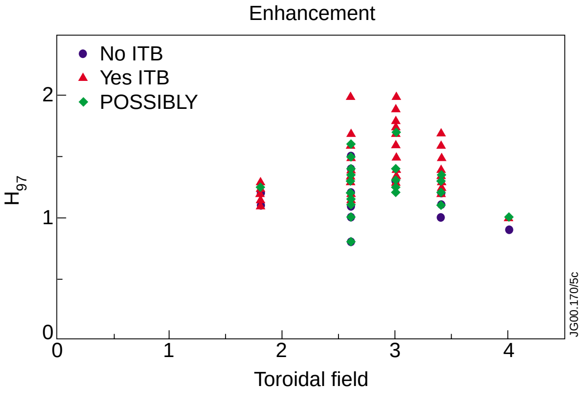

Fig.11.2: Correlation between improvement in plasma performance and ITB emergence (triangles- discharges with ITB, circles- without ITB).

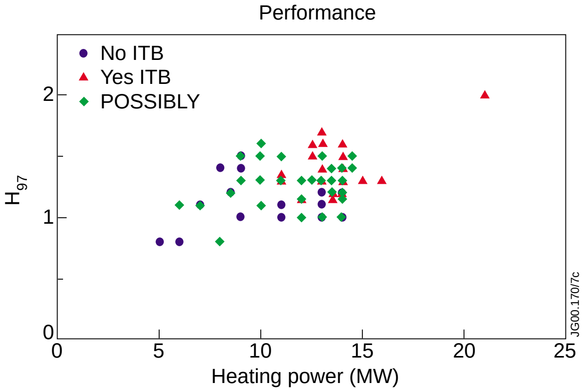

Fig.11.3: Correlation between plasma performance and heating power for discharges with 2.6T toroidal field.

This uncertainty with enhancement factor H97 is further emphasised in the Fig.11.3, where H97 is plotted for the series of B_T=2.6 T shots as a function of the heating power. We can conclude that although generally discharges with higher power have better performance, heating power is certainly not the unique parameter, which controls the ITB formation. Second conclusion is that in many cases (particularly in discharges with modest level of the heating power) the quality of the ITB is not very good. This results in the level of H97 comparable to that of the good quality ELMy H-mode. In the sense, two transport barriers – internal ITB and edge ETB compete with each other. Only one barrier usually survives if there is not enough power and this might be either of these two (or intermittently).

We also tried to find a correlation between ITB formation and previously defined plasma quality parameter Q. The idea to use parameter $Q \equiv \dfrac{R_{NT}(neut/\mathrm{sec})}{300 \cdot [W_{PD}(J)]^2}$ for plasma performance characterisation follows from the fact that beam-thermal reaction rate scales linearly with energy content and thermal-thermal reaction rate scales as square of the thermal energy content. We therefore might expect to maximise Q value in discharges with ITB, where thermal-thermal reaction contribution is emphasised. The result of our study is shown on Fig.11.4 and is quite disappointing- there is no correlation.

There are several reasons, which might explain such a result. The one, which we already used previously, is that plasma performance is comparable in weak ITB plasma and ELMy H-mode one. The second contributing factor is that Fig.11.4 is compiled from discharges with different heating schemes, ranging from pure NBI heating to pure ICRH heating. Obviously these two extremes produce very different level of beam-thermal reaction.

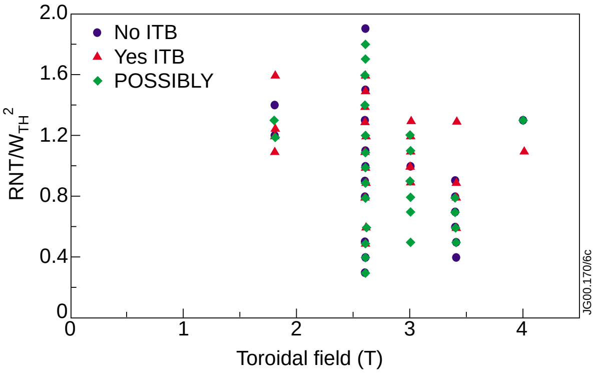

Fig.11.4: Plasma quality as a function of toroidal magnetic field in discharges with ITB (red triangles) and without ITB (blue circles).

It is possible to clarify the relative role of RF and NBI power in the ITB development by comparing plasma performance of a series of discharges with 2.6 T toroidal field. Figure 11.5 summarises this attempt and allows us to draw some conclusions (however very preliminary).

- There is quite a few examples where ITB has been produced with NBI heating only (indicated by the filled triangles at zero heating power in Fig.11.5);
- There is no examples of ITB formation by pure ICRH heating (with a caveat that ICRH power did not exceed $P_{RF} < 8$ MW in our experiments and "usual" level of NBI power capable to trigger an ITB was about $P_{NBI} > 10$ MW);
- Adding up of RF power apparently increases performance of discharges with ITB (possibly due to the centrally peaked ICRH power deposition).
- There is no clear correlation between relative proportion of the NBI power (the ratio P_{NBI}/P_{TOT}) and H97 (Fig.11.6);
- There is an apparent necessity to continue experiments aimed on clarification of the relative role of RF and NBI power in the ITB formation.

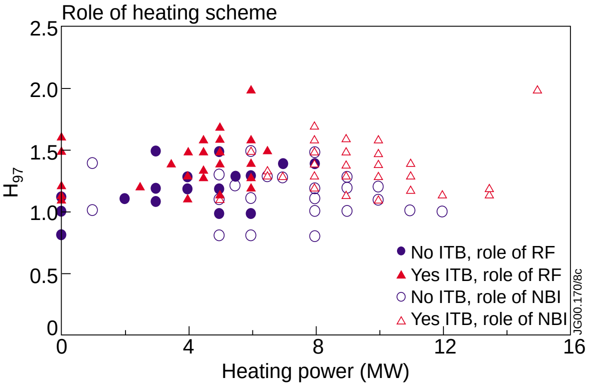

Fig.11.5: Plot showing separately the RF power (filled symbols) and NBI power (open symbols), and whether an ITB was formed (triangles) or not (circle).

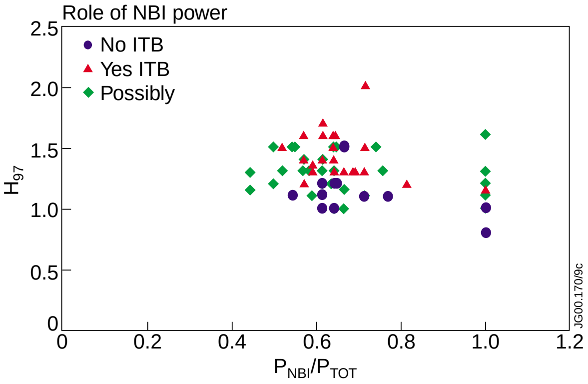

Fig.11.6: Relative role of NBI heating in ITB formation

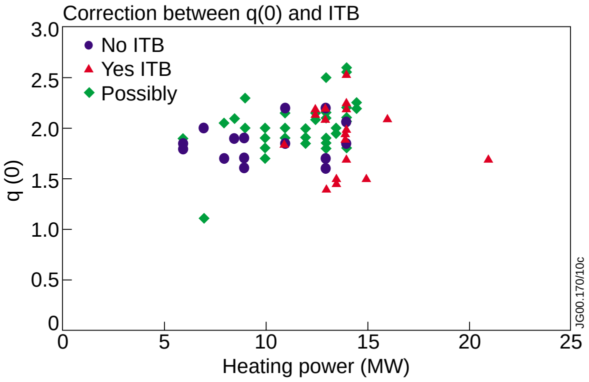

Fig.11.7: Correlation between q-profile and the ITB formation.

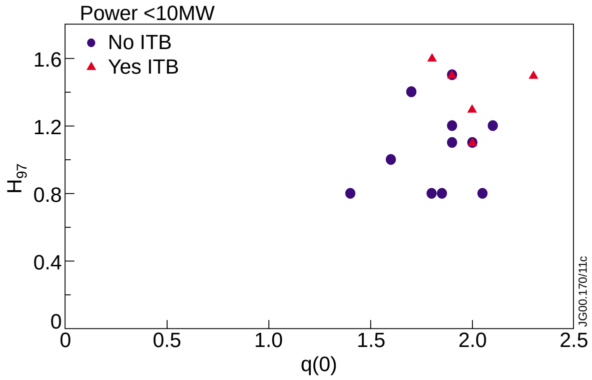

Fig.11.8: Role of q(0) for discharges with heating power less than 10 MW

Our next task was to find out if magnetic configuration plays an important role in the ITB formation. Since our database has not been specifically prepared for this task, the only one source of information about magnetic configuration, which we could use, is EFIT. This seriously undermines our efforts since EFIT, if not supported by either MSE or polarimetry, generates not very reliable q-profile, particularly near plasma centre. Figure 11.7 indeed shows no correlation between central q-value at the onset of plasma heating and an ITB emergence. Situation changes, however if we would discuss discharges with the limited heating power level of $P_h < 10$ MW. Figure 11.8 presents plasma performance as a function of q(0) value for a series of low power plasmas. Contrary to the previous plot (Fig.11.7) this figure shows some correlation – the higher is q(0), the higher is the probability to get an ITB while applying a limited power. Once again, this conclusion is tentative and should be cross-checked in the next campaign. It is worth reminding here that it was previously concluded by JET team [11.2] that it is easier to form the ITB being close to q=2 surface.

11.3 Summary and future directions

An extended database of Optimised Shear plasmas with the heating power within the range, where an emergence of the ITB is expected, has been created. A first attempt to find correlation between different plasma parameters and an ITB appearance is reported.

In particular, it was demonstrated that ITB requires certain access power, which scales roughly linearly with either toroidal or poloidal magnetic field. There is still no universal procedure, which allows determining automatically an emergence of the ITB. CEA and ENEA have recently reported some promising results using critical temperature gradient as a test for the ITB formation.

Good quality ITB could be determined by a large increase in the confinement time enhancement factor (H97>1.5). However, this method could not be applied in the situations of a week ITB, which gives H97 comparable to those of ELMy H-mode.

An attempt has been made to find out if method of additional heating (ICRH versus NBI in JET) plays any role in the ITB formation (this complements results, presented previously by Yu. Baranov in chapter 10). However preliminary, our data indicate that NBI power is capable on producing ITB on its own. ICRH, at least at its present level of P_{RF} <8-10 MW, needs some assistance from the NBI. More dedicated experiment should be done before arriving on any firm conclusion about the prospects for strong ITB formation at large radius with ICRH alone.

Some limited attempt to find a correlation between an ITB emergence and magnetic configuration has been done. Since EFIT constrained only by magnetics was the only available tool for such large database, we use q(0) at the onset of strong heating as a figure of merit parameter. Preliminary analysis shows that there might be a correlation between q(0) and the ITB- the larger is q(0), the higher is the probability for ITB to emerge. This correlation, however disappears in discharges with the power level, significantly higher than the power threshold. Once again, more dedicated experiments should be conducted in order to clarify this issue.

Table 1.

Pulse	Description	B_T (T)	P_{NBI}	P_{ICRH}	P_{MAX}	ITB(Y/N)	H_{97max}	RNT/WTH^2
46480	spring campaign	3.4	12	5	17	n	1	0.6
46481	spring campaign	3.4	13	7	20	n	1.2	0.7
46483	spring campaign	3.4	16	7	23	n	1.2	0.9
46828	ITB access power	2.6	1	7	8	n	1.4	0.4
46829	ITB access power	2.6	1	8	9	n	1.4	0.4
46836	ITB access power	2.6	1	8	9	n	1	0.3
46852	spring campaign	3.4	4	6	10	n	1.1	0.5
46853	spring campaign	3.4	6	6	12	n	1.2	0.5
46854	spring campaign	3.4	6	6	12	n	1.1	0.5
46855	spring campaign	3.4	4	5	9	n	1.1	0.5
46856	spring campaign	3.4	6	6	12	n	1.2	0.5
46859	spring campaign	3.4	3	6	9	n	1.1	0.4
46860	spring campaign	3.4	6	6	12	n	1.2	0.5
46861	spring campaign	3.4	6	6	12	n	1.2	0.5
46862	spring campaign	3.4	6	6	12	n	1.2	0.5
46863	spring campaign	3.4	6	6	12	n	1.2	0.5
46870	spring campaign	3.4	6	5	11	n	-	0.5
46872	spring campaign	3.4	6	5	11	n	1.1	0.5
46873	spring campaign	3.4	6	5	11	n	1.2	0.5
46875	spring campaign	3.4	6	5	11	n	1.2	0.5
46876	spring campaign	3.4	6	6	12	n	1.1	0.7
46877	spring campaign	3.4	4	6	10	n	1.2	0.5
46880	spring campaign	3.4	4	6	10	n	1.2	0.5
46881	spring campaign	3.4	4	4	8	n	1.1	0.5
46882	spring campaign	3.4	4	5	9	n	1.1	0.4
46883	spring campaign	3.4	4	5	9	n	1	0.4
46884	spring campaign	3.4	4	5	9	n	1.1	0.4
46885	spring campaign	3.4	4	5	9	n	1.1	0.4
46886	spring campaign	3.4	4	5	9	n	1.1	0.4
46955	spring campaign	3.4	4	5	9	n	1.1	0.4
46993	spring campaign	3.4	12	6	18	n?	-	0.8
46995	attempt at 4 T	4	14	5	19	n?	1	1.3
46996	attempt at 4 T	4	14	5	19	n	0.9	1.3
46997	attempt at 4 T	4	14	5	19	n	0.9	1.3
46999	spring campaign	3.4	10	4	14	n	1.1	0.9
47000	spring campaign	3.4	8	6	14	n	1.2	0.6
47040	ITB access power	3	10	5	15	n	1.3	1
47074	with Ar	3	12.5	5	17.5	n?	1.3	1
47077	with Ar	3	7	6	13	n?	1.2	0.7
47147	spring campaign	3.4	7	6	13	?	1.2	0.6
47161	spring campaign	3.4	12	6	18	n	1.2	0.8
47423	spring campaign	3.4	6	6	12	n	1.2	0.6
47612	rubbish	3.4						
47635	ITB access power	2.6	10	3	13	n	1.1	0.9

Pulse	Description	B_T (T)	P_{NBI}	P_{ICRH}	P_{MAX}	ITB(Y/N)	H_{97max}	RNT/WTH^2
47645	ITB access power	2.6	9	5	14	?	1.2	0.8
47665	ITB access power	2.6	8	5	13	n	-	0.9
47668	ITB access power	2.6	8	5	13	n?	-	1.1
47675	ITB access power	2.6	6.5	6	12.5	?	1.3	1.2
47680	ITB access power	2.6	6.5	6	12.5	?	1.3	1.3
47693	ITB access power	2.6	9	5	14	n	1.2	1.1
47712	ITB access power	2.6	9	5	14	n	-	1
47845	main heating timing scan	1.8	8.5	4	12.5	n	1.1	1.2
47852	RF power scan at fixed NBI power	1.8	8	-	8	n	-	1.4
47853	RF power scan at fixed NBI power	1.8	8	3	11	n	1.2	1.4
47947	ITB access power	2.6	6	5	11	n	1.1	0.8
48105	ITB access power	2.6	5	2	7	n		
48106	ITB access power	2.6	4	2	6	n		
48146	ITB access power	2.6	5	2	7	n		
48152	ITB access power	2.6	8	5	13	n	1.2	0.5
48154	ITB access power	2.6	8	5	13	n	1.1	0.5
48155	ITB access power	2.6	8	5	13	n	1.1	0.5
48156	ITB access power	2.6	8	5	13	n	1.1	0.5
48157	ITB access power	2.6	8	5	13	n	1.1	0.5
48158	ITB access power	2.6	8	5	13	n	1.1	0.5
48163	no KK3	2.6						
48165	no KK3	2.6	5	5	10	?	1.3	0.4
48171	no KK3	2.6						
48222	no KK3	2.6	5.5	3	8.5	?	1.2	0.3
48226	ELM free H-mode?	2.6	5.5	3	8.5	n	1.2	0.3
48228	ITB access power	2.6	8	5	13	n?	1.5	0.5
48636	disruption	2.6						
48947	RF only	2.6	-	5.5	5.5	n		
48979	ITB access power	2.6	10	4	14	?	1.2	0.8
49014	NBI only	2.6	11	-	11	n	1	1.5
49018	ITB access power	2.6	6	3	9	n	1.5	1
49256	NBI only	2.6	5	-	5	n	0.8	0.8
49330	NBI only	2.6	6	-	6	n	0.8	0.9
49341	ITB access power	2.6	6	5	11	?	1.1	0.5
49344	NBI only	2.6	6	-	6	n	0.8	1.9
49366	NBI only	2.6	8	-	8	n?	0.8	1.4
49367	NBI only	2.6	13.5	-	13.5	n	1.2	1.3
49370	NBI only	2.6	9	-	9	n	1	1.5
49398	ITB access power	2.6	9	5.5	13.5	n?	1.3	1.2
49425	ITB access power	2.6	6	4	10	?	1	1.7
49426	autumn campaign	3.4	12	5	17	n?	1.1	0.7
49428	with Ar	3.4	17	6	23	n?	1.2	0.6
49434	with Ar	3.4	16	6	22	?	1.2	0.8
49443	NBI only	2.6	12	-	12	n?	1	1.7

Pulse	Description	B_T (T)	P_{NBI}	P_{ICRH}	P_{MAX}	ITB(Y/N)	H_{97max}	RNT/WTH^2
49447	NBI only	2.6	10	-	10	n?	1.1	1.6
49452	ITB access power	2.6	7	5	12	n?	1.35	1.2
49454	rubbish	2.6						
49455	rubbish	2.6						
49657	with Ar	3.4	16	7	23	n	1.2	0.7
49658	with Ar	3.4	17	8	25	y	1.35	0.8
49659	with Ar	3.4	18	7	25	?	1.35	0.8
49664	with Ar	3.4	17	7	24	y	1.5	0.9
46488	spring campaign	3.4	18	5	23	y	1.7	1.3
46998	attempt at 4 T	4	14	6	20	y	1	1.1
47011	spring campaign	3.4	8	6	14	y	1.2	0.8
47033	ITB access power	2.6	15	6	21	y	2	1.4
47034	ITB access power	3	15	5	20	?	1.3	1
47039	ITB access power	3	15	5	20	y	1.7	1.3
47046	ITB access power	3	16	4	20	y	1.7	1.3
47047	with Ar	3	14	5	19	y	1.3	1
47048	with Ar	3	16	5	21	y	1.4	1.2
47049	with Ar	3	15	6	21	y?	1.4	1.2
47050	with Ar	3	16	6	22	y	1.5	1.2
47055	with Ar	3	16	6	22	y	1.6	1.3
47056	with Ar	3	16	6	22	y	1.4	1.1
47057	with Ar	3	15	6	21	y	1.5	1.1
47058	with Ar	3	16	6	22	y	1.6	1.2
47060	with Ar	3	14	6	20	y	1.7	1.2
47061	ITB access power	3	5	4	9	?	1.3	0.5
47066	ITB access power	3	14	5	19	y	1.5	1.3
47067	with Ar	3	12.5	5	17.5	y	1.4	1
47068	with Ar	3	14	5	19	y	1.9	1.2
47069	with Ar	3	13	5	18	y	1.4	1.1
47070	with Ar	3	14	5	19	y	1.35	1.2
47073	no KK3	3	14	5	19	y	1.7	1.3
47078	with Ar	3	10	6	16	y?	1.25	0.8
47081	with Ar	3	14	6	20	y	1.5	1.2
47082	with Ar	3	14	6	20	?	1.4	1
47083	with Ar	3	15	6	21	y	1.8	1
47084	with Ar	3	16	6	22	y	1.7	1.2
47087	with Ar	3	16	6	22	y	1.8	1.3
47091	with Ar	3	16	6	22	y	1.75	1.3
47093	with Ar	3	16	6	22	y	1.5	1.2
47094	with Ar	3	16	6	22	y	1.7	1.1
47095	with Ar	3	16	6	22	y?	1.7	1.1
47096	with Ar	3	16	6	22	y	1.7	1.1
47097	with Ar	3	16	7	23	y	1.8	1.2
47099	with Ar	3		7	21	y	1.4	0.9

Pulse	**Description**	**B_T (T)**	**P_{NBI}**	**P_{ICRH}**	**P_{MAX}**	**ITB(Y/N)**	**H_{97max}**	**RNT/WTH^2**
47100	with Ar	3	14	7	21	y	1.5	1
47101	with Ar	3	14	7	21	y	1.9	1
47102	with Ar	3	16	7	23	y	1.9	1
47103	with Ar	3	16	7	23	y	1.9	1.1
47104	with Ar	3	16	7	23	y	2	1.1
47109	with Ar	3	16	7 to 0	17	?	1.4	0.9
47110	with Ar	3	14	7	21	y	1.4	1
47111	with Ar	3	16	7	23	y	1.6	1.1
47112	with Ar	3	16	7	23	y	1.6	1.1
47114	with Ar	3	16	7	23	y	1.8	1.1
47115	with Ar	3	15	7	22	y	1.7	1.1
47116	with Ar	3	16	7	23	y	1.6	1.1
47123	with Ar	3	16	7	23	y	1.75	1.1
47125	with Ar	3	14	4	18	y?		1.2
47130	with Ar	3	14	6	20	y		1.1
47167	spring campaign	3.4	7	6	13	n	-	0.7
47168	with Ar	3	16	7	23	y	1.7	1.1
47169	with Ar	3	14	7	21	y	1.5	1.1
47170	with Ar	3	15	7	22	y		1.1
47177	with Ar	3	16	8	24	y	1.9	1
47178	with Ar	3	17	7	24	y	1.6	1.2
47179	with Ar	3	15	8	23	y	1.7	1
47184	with Ar	3	17	7	24	y	1.7	1.1
47185	with Ar	3	18	8	26	y	1.7	1
47186	with Ar	3	18	8	26	y	1.8	1
47187	with Ar	3	13	7 to 9	22	y	2	0.9
47188	with Ar	3	17	7 to 9	26	y	2	1
47189	with Ar	3	16	9	25	y	1.9	1
47190	with Ar	3	15	9	24	y	2	1
47191	with Ar	3	17	7	24	y	1.7	1
47192	with Ar	3	17	7	24	y	1.6	1
47196	with Ar	3	17	7	24	y	1.7	1
47229	with Ar	3	17	7 to 9	26	y	1.6	1
47319	spring campaign	3.4	12	6	18	y	1.2	0.9
47365	spring campaign	3.4	9	6	15	y	1.25	0.6
47392	spring campaign	3.4	6	8.5	14.5	y?	1.3	0.5
47617	ITB access power	2.6	9	5	14	y	1.4	1.2
47618	ITB access power	2.6	9	5	14	y	1.3	1
47624	ITB access power	2.6	9	5	14	y	1.4	1
47627	no kk3	2.6	9	5	14	?	1.3	1.3
47630	ITB access power	2.6	9	5	14	?	1.3	1.3
47634	ITB access power	2.6	10	5	15	y	-	1.4
47647	ITB access power	2.6	11	5	16	y	-	1.5
47652	ITB access power	2.6	8	4.5	12.5	Y	1.5	1.4

Pulse	Description	B_T (T)	P_{NBI}	P_{ICRH}	P_{MAX}	ITB(Y/N)	H_{97max}	RNT/WTH^2
47662	ITB access power	2.6	8	4.5	12.5	y	1.6	1.5
47663	ITB access power	2.6	08-Jan	6.5	14.5	?	-	1.3
47664	ITB access power	2.6	8	5	13	y?	-	1.2
47669	ITB access power	2.6	8	6	14	y	1.6	1.5
47670	ITB access power	2.6	8	6	14	?	1.4	1.3
47671	ITB access power	2.6	11	3.5	14.5	?	1.4	1.3
47674	ITB access power	2.6	6.5	6	12.5	y	1.5	1.4
47714	ITB access power	2.6	10	4	14	y	1.5	1.2
47720	ITB access power	2.6	10	4	14	y	1.3	1.2
47840	ITB access power	2.6	9	5	14	y	1.6	1.3
47841	main heating timing scan	1.8	10	4	14	y	-	1.2
47842	main heating timing scan	1.8	11	3.5	14.5	?	1.25	1.2
47843	main heating timing scan	1.8	11	3.5	14.5	?	-	1.3
47844	late barrier	1.8	11	3.5	14.5	y	1.2	1.2
47846	late barrier	1.8	10	4	14	y	1.25	1.2
47847	late barrier	1.8	10	4	14	y	1.1	1.1
47848	main heating timing scan	1.8	11	1	15	y	1.3	1.25
47849	reduced RF power	1.8	11	-	11	y	1.25	1.6
47851	reduced RF power	1.8	11	-	11	y	1.25	1.6
47854	RF power scan at fixed NBI power	1.8	8	4	12	y	1.1	1.1
47857	RF power scan at fixed NBI power	1.8	8	6	14	y	1.15	1.2
47927	ITB access power	2.6	9	5	14	y	1.3	0.9
47930	ITB access power	2.6	9	5	14	y	1.3	1.1
47933	ITB access power	2.6	9	5	14	y	1.6	1.1
47934	ITB access power	2.6	8	5	13	y	1.7	1.3
47940	ITB access power	2.6	8	5	13	y	1.6	1.3
47948	very small barrier	2.6	8	6	14	y	1.2	1
47949	ITB access power	2.6	8	6	14	?	1.3	1
47960	very small barrier	2.6	8	6	14	y	1.4	1.1
47962	ITB access power	2.6	7	5	12	?	1.3	0.9
47963	short lived barrier (possibly)	2.6	6.5	4.5	11	?	1.3	0.9
47964	small barrier	2.6	6.5	4.5	11	y	1.35	1
48104	small barrier	2.6	6.5	4.5	11	y	1.3	0.8
48160	ITB access power	2.6	9	5	14	y?	1.15	0.5
48173	no KK£	2.6	11	2.5	13.5	y	1.2	0.6
48184	no KK3	2.6	8	5	13	y	1.4	0.5
48185	no KK3	2.6	8	5	13	y?	1.3	0.5
48198	no KK3	2.6	8	5	13	y?	1.3	0.5
48205	no KK3	2.6	7	5	12	y?	1.3	0.4
48218	no KK3	2.6	8	5	13	y?	1.3	0.6
48234	small, late barrier	2.6	9	5	14	y	1.3	0.6
48238	NBI step down	2.6	9	5	14	y	1.3	0.6
48951	ITB access power	2.6	9	4	13	y	1.3	1
49019	ITB access power	2.6	8	5	13	y	1.7	1.1

Pulse	Description	B_T (T)	P_{NBI}	P_{ICRH}	P_{MAX}	ITB(Y/N)	H_{97max}	RNT/WTH^2
49020	small ITB	2.6	10	3.5	13.5	y?	1.4	1.3
49022	ITB access power	2.6	5	5	10	?	1.5	0.8
49189	ITB access power	2.6	6	5	11	y?	1.5	1
49194	NBI only	2.6	8	-	8	?	1.5	
49203	NBI only	2.6	10	-	10	?	1.6	1.8
49255	NBI only	2.6	13.5	-	13.5	y	1.15	1.5
49368	NBI only	2.6	12	-	12	y	1.15	1.6
49402	pure RF preheat	2.6	4	5	9	y?	1.3	1
49411	pure RF preheat	2.6	4	5	9	?	1.3	1
49435	with Ar	3.4	17	8	25	y	1.3	0.8
49436	with Ar	3.4	16	7	23	y	1.6	0.8
49437	with Ar	3.4	17	8	25	y	1.7	0.8
49441	with Ar	3.4	14	8	22	y?	1.3	0.8
49442	with Ar	3.4	17	8	25	y	1.4	0.8
49444	NBI only	2.6	12	-	12	y?	1.15	1.6
49445	NBI only	2.6	10	-	10	y?	1.1	1.6

11.4 Acknowledgement

The authors are grateful to all members of Task Force C for providing the data and numerous useful discussions.

11.5 References

[11.1] The JET Team (presented by C. Gormezano), in Proceeding of 17th Fusion Energy Conference, Yokohama, 1998, IAEA, Vienna, 1999, vol.2, page 705;

[11.2] C. Challis et al, B. Alper, Yu. Baranov et al., 26 EPS Conf. On Contr. Fusion and Plasma Physics, Maastricht, 14-19 June 1999, ECA Vol. 23J (1999) 69-72.

12. TASK FORCE C ITER DATABASE ENTRIES

Y.Baranov[1], G Cottrell[1] and V Parail[1]

JET Joint Undertaking, Abingdon, Oxon, OX14 3DB, UK
[1] EURATOM/UKAEA Fusion Association, Culham Science Centre, Abingdon, UK

From data acquired during Task Force B/C experiments two types of ITER database entry have been made:-

- Into the global confinement database for the ITER confinement shape scan experiments
- Into the ITER profile database for a range of types of Optimised Shear discharges

12.1 Global confinement database entries

Inclusion of pulses in the confinement database requires the selection of stable pulses showing steady confinement, typically for at least two energy confinement times. The “good” time windows are then marked by physicists and data is then read in, through an automated procedure, before being validated by the physicists. From the ITER shaping confinement experiment 47 pulses have been included using this procedure. These are all ELMy H-mode discharges and provide valuable ITER relevant information, especially in terms of shaping and elongation. The pulses are listed in Table 12.1

Table 12.1: Pulses included into the ITER Global Confinement Database

49126	49128	49129	49130	49131	49133	49134	49136
49137	49138	49139	49140	49144	49145	49146	49147
49149	49151	49152	49153	49154	49156	49157	49159
49160	49161	49164	49165	49166	49167	49168	49169
49170	49172	49173	49180	49181	49182	49185	49186
49573	49581	49582	49583	49591	49592	49596	

12.2 Profile database entries

A range of different types of Optimised Shear discharges have been entered into the ITER profile database. These pulses are listed in Table 12.2 and described in the accompanying notes.

Table 12.2 Plasma parameters of pulses entered into the ITER Profile Database

Pulse	**$I_{P,max}$ (MA)**	**B_T (T)**	**Main heating (MW)**			**LHCD preheat?**	**Argon seeding?**
			$P_{NB, max}$	**$P_{RF, max}$**	**$P_{LH, max}$**		
47413	3.5	3.45	18.7	11.7	0	Only bd*	Yes
46695	2.7	2.5-2.7	15.7	5.9	0.7	No	Yes
49197	2.3	2.6	15.4	0	0	No	No
49651	2.2	2.6	12.5	4.8	0	Yes	No

** LHCD applied briefly at the time of the plasma initiation, but not during the whole current ramp-up phase.*

General remarks

The data used for the ITER Database entries is taken from simulations performed using the TRANSP code [12.1]. The electron density profiles are measured using the LIDAR Thomson scattering diagnostic, for which the spatial resolution (≈12cm) is typically unable to resolve the steep density gradients produced by transport barriers. The ion and electron temperature profiles have typically been measured using charge-exchange recombination spectroscopy and ECE emission measurements using a heterodyne radiometer, respectively. It should be noted that the modification of the NBI induced fast ion distribution by ICRH is not modelled in these simulations.

Pulse number 47413 (TRANSP id number 608S)

This pulse achieved high fusion performance for ≈1 second in roughly steady conditions. The ITB was fairly broad and weak, which avoided the pressure driven disruptive limit and allowed relatively high β_N to be maintained. The plasma exhibited small ELMs throughout the high power phase, which were controlled using argon seeding. The ion temperature profile used in the simulation has been determined using the standard multi-Gaussian fit technique that is known to lead to an overestimate when argon is present in the plasma (see section 13). In this situation the Z-effective profile cannot be determined accurately using charge-exchange recombination spectroscopy. The shape has been assumed and the magnitude normalised to the line averaged value measured using visible bremsstrahlung radiation. The initial q-profile was taken from an EFIT [12.2, 12.3] equilibrium reconstruction using magnetics data only at a time 2 seconds after the plasma initiation. After this time the current penetration was simulated assuming neo-classical plasma conductivity.

Pulse number 46695 (TRANSP id number 911P)

This pulse achieved high β_N with high power heating and reduced toroidal magnetic field strength. The magnetic field was increased in a slow ramp towards the end of the high power heating phase, which led to a shift in the radial coverage of the ECE measurements usually used for electron temperature determination. As a result the lower spatial resolution LIDAR Thomson scattering data was used in the simulation of this pulse. Again the ELM activity was controlled using argon seeding with the same effect on the ion temperature and Z-effective measurements as for the previous pulse. The initial q-profile was taken from an EFIT equilibrium reconstruction using magnetics data only at a time 2 seconds after the plasma initiation. After this time the current penetration was simulated assuming neo-classical plasma conductivity.

Pulse number 49197 (TRANSP id number 405Z)

This pulse used only NBI heating to form a ‘strong’ ITB. The fusion performance of the plasma continued to increase during the high power heating phase until it was terminated by a disruption, presumably due to a pressure driven MHD mode. In this case argon seeding was not used.

Nevertheless, the Z_{eff} profile was constructed as for the previous pulses. After comparison of the electron temperature measurements, from the LIDAR Thomson scattering and ECE heterodyne radiometer, it was decided to use the higher resolution ECE data increased everywhere by 250eV. The initial q-profile was taken from an EFIT equilibrium reconstruction using magnetics data only at a time 2 seconds after the plasma initiation. After this time the current penetration was simulated assuming neo-classical plasma conductivity.

Pulse number 49651 (final TRANSP id number ABØ6)

This pulse had an LHCD prelude to modify the target q-profile for main heating (see section 8). In order to provide a meaningful simulation the TRANSP run was started just before the main heating phase with a q-profile determined with EFIT constrained using motional Stark effect data. After this time the current penetration was simulated assuming neo-classical plasma conductivity.

References

[12.1] R J Goldston, et al., J Comput Phys **43** (1981) 61.

[12.2] L L Lao, et al., Nucl. Fusion **25** (1985) 1611.

[12.3] D P O’Brien, et al., Nucl. Fusion **32** (1992) 1351.

13. ION TEMPERATURE VALIDATION IN THE PRESENCE OF ARGON

K-D Zastrow[1], C Giroud[2]

JET Joint Undertaking, Abingdon, Oxon, OX14 3EA, UK
[1] UKAEA Fusion, Culham Science Centre, Abingdon, OX14 3DB, UK
[2] CEA Cadarache, DRFC/SIPP/CFM,F-13108 Saint Paul lez Durance Cedex, France

13.1 Overview

When Argon is introduced into optimised shear discharges for edge control, the spectra obtained from charge-exchange spectroscopy (CXS) become polluted by several features due to the emission of low ionisation stages of Argon in the plasma edge (see Fig.13.1). From the point of view of the experiment, radiation is used to cool the edge, and the spectral lines are a by-product of the desired result. From the point of view of ion temperature measurements on Carbon, the task becomes more difficult.

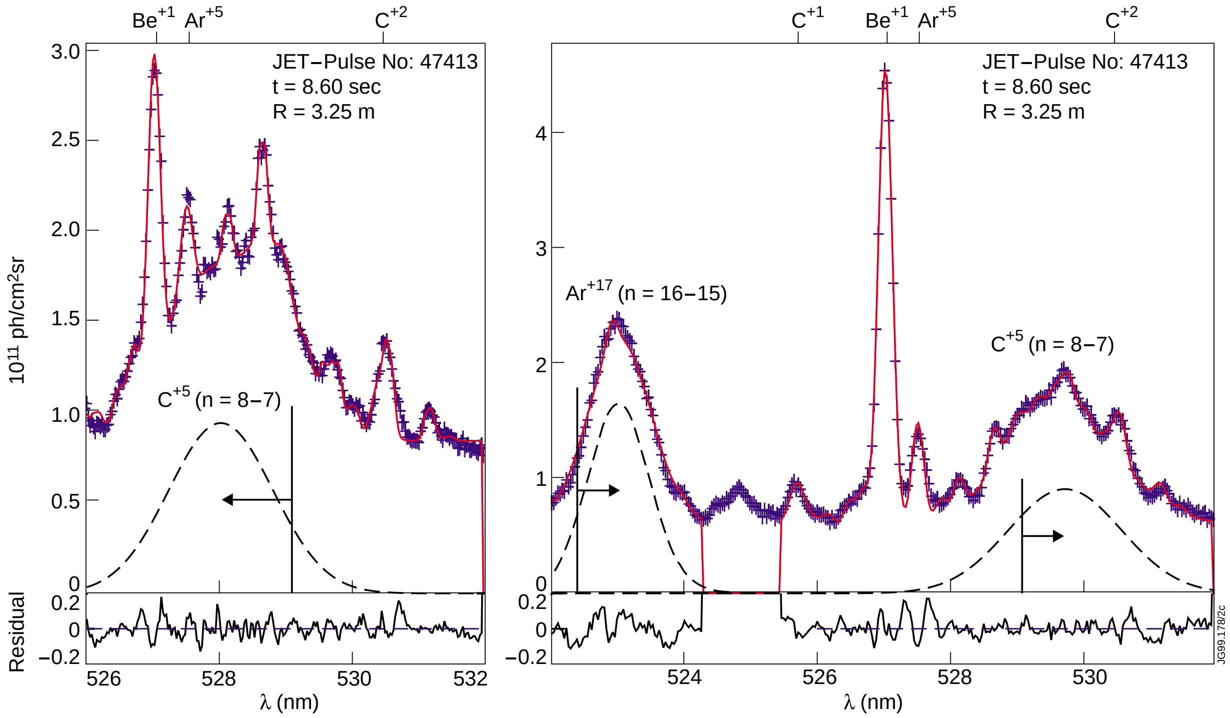

Fig.13.1: Charge exchange spectra with Argon edge emission superimposed (from [13.1]).

We have previously developed an analysis technique that attempts to represent the Argon spectra by several Gauss profiles, and thus infer temperature and rotation from the underlying Carbon features [13.1]. The results from this technique fail the data validation, which is done by comparing results from two instruments (KS5A with PPFs called CXSM and KS5B with PPFs called CXDM) obtained at the same major radius (see Fig.13.2). The difference between the instruments is the direction of the Doppler shift. This causes the Carbon feature to interfere with different spectral lines from Argon on both instruments. This leads to different systematic errors.

During the 1999 autumn campaign, we performed several experiments with notched neutral beam waveforms. During the notch, active charge-exchange features are missing from the spectra, and we can separately measure the passive background emission. The CX spectra taken after the neutral beam power is re-applied are then analysed after first subtracting the passive spectra from the total. In the ideal case, this leaves just the active component. In reality, the edge components vary with time, and what is actually achieved is an improvement in signal-to-noise ratio that persists for a few 100 msec. This technique assumes that the ITBs and ion temperature profile is not significantly affected by the notch.

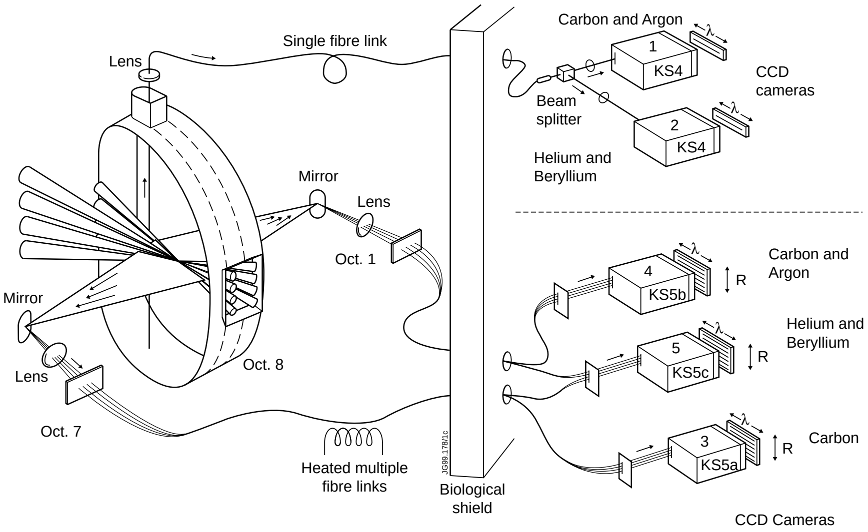

Fig.13.2: Layout of the CXS instruments on JET (from [13.1]).

Due to the viewing direction, the Carbon features appear with positive or negative Doppler shift in the two spectra. This leads to different systematic errors in the analysis for both instruments.

13.2 Results

The CXS instruments are aligned to Pini 6&7 of the Oct. 8 beams. The power supplies on Oct.8 are arranged in such a way that if Pini 6 is notched, so is Pini 5, and if Pini 7 is notched, so is Pini 8. Therefore, in each notch, half the power from Oct. 8 is removed from the plasma. To minise the impact, we chose a 100 msec notch time, and aligned it to ~1 msec accuracy to the data acquisition of the CXS systems. Two CXS spectra of 50 msec each are taken during the notch.

The best results were obtained in the one discharge where we applied more power from the Oct. 4 beams during the notch (See Figs.13.3 and 13.4). For most experiments, this is however not an option, and all other notch experiments were performed without power compensation.

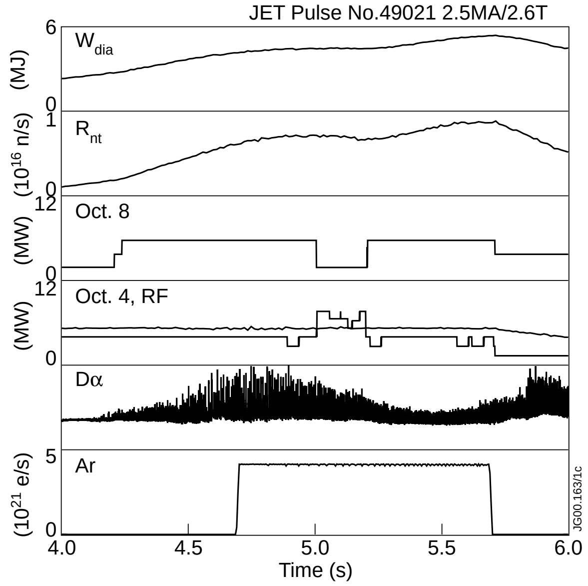

Fig.13.3: Time history of NBI waveform and its effect on the plasma for #49021. In this discharge, the Oct. 4 power was increased during the time of the notch to maintain constant total input power.

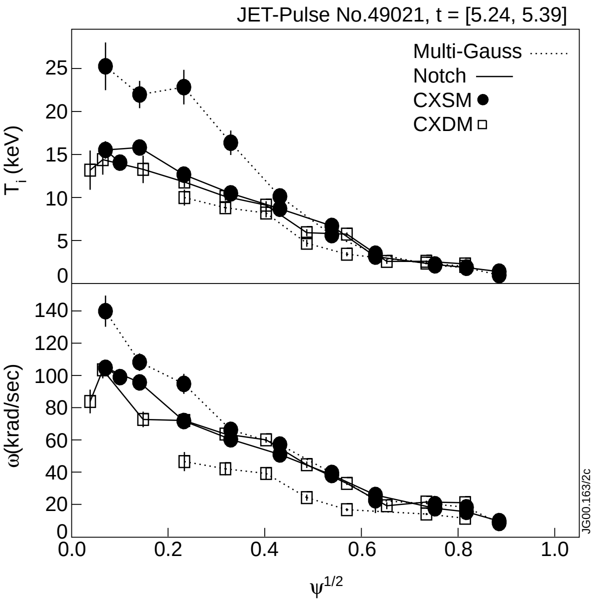

Fig.13.4: Ion temperature and toroidal rotation comparing the result from the Multi-Gauss fitting method with the notch method for #49021. The location of the transport barrier from CXSM (Multi-Gauss) is confirmed, but the central temperature is reduced significantly. The location of the transport barrier from CXDM (Multi-Gauss) is modified.

There is no general result that could be used to correct all ion temperature measurements. This applies both to the location of the transport barrier and the central temperature. It is worthwhile noting that all methods are in good agreement for edge temperature and rotation (10 cm inside the LCFS).

The remainder of this section summarises all the discharges where this technique has been successfully applied. In each case it is necessary to examine the plasma behaviour following the notch to insure that the background spectra taken are still representative. Generally, the results from the two instruments start to diverge again a few 100 msec after the notch. The radial profiles shown are the average temperature and rotation during the time window where the notch method is successful.

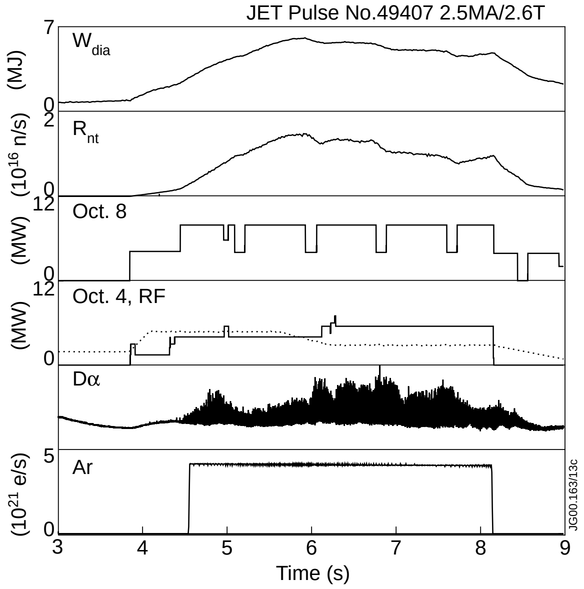

Fig.13.5: Time history of NBI waveform and its effect on the plasma for #49407. In this discharge we attempted to provide several measurements by multiple beam notches, without compensation of the total power from Oct. 4. The performance of the plasma suffers, and only the first two notches actually provide useful CXS data.

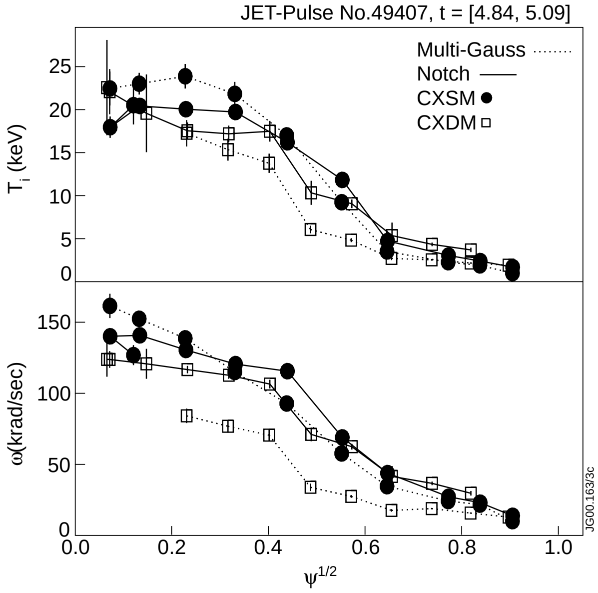

Fig.13.6: Ion temperature and toroidal rotation comparing the result from the Multi-Gauss fitting method with the notch method for the first notch in #49407. The location of the transport barrier and central temperature from CXSM (Multi-Gauss) is confirmed. The location of the transport barrier from CXDM (Multi-Gauss) is modified.

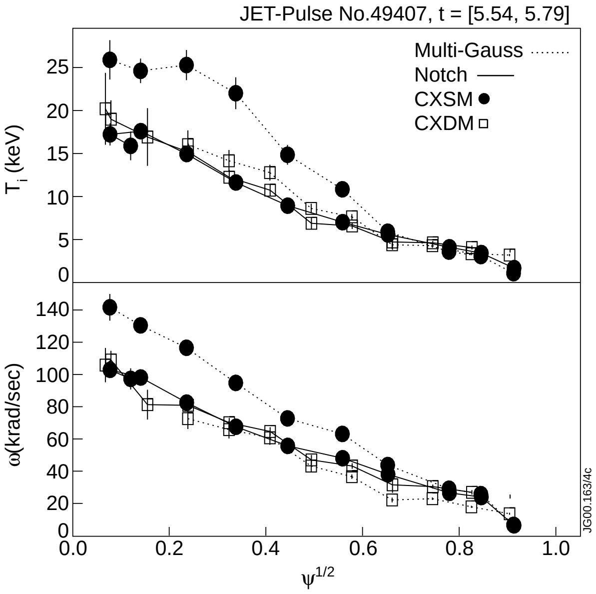

Fig.13.7: Results for the second notch in #49407. All profiles show only a weak transport barrier. The central temperature from CXSM (Multi-Gauss) is reduced significantly.

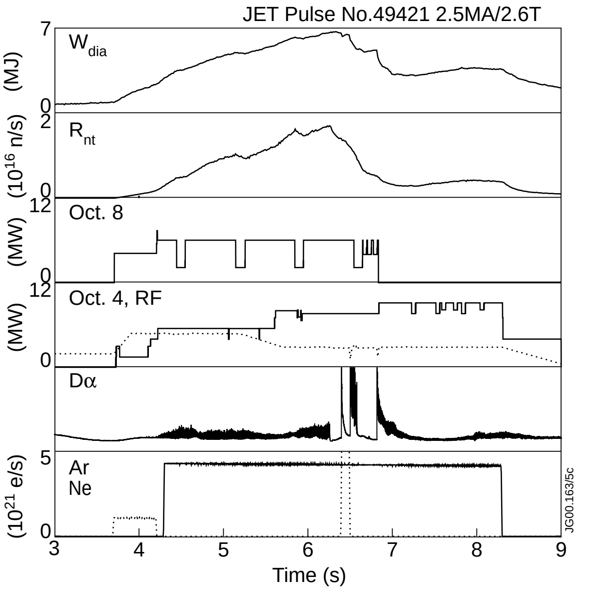

Fig.13.8: Time history of NBI waveform and its effect on the plasma for #49421. This discharge also has a Neon prefill and gas puff (unfortunately after the loss of the ITB) for impurity transport studies (see chapter 7). In this discharge, we attempted to provide several measurements by multiple beam notches, without compensation of the total power from Oct.4. All three notches before the ELM free period at t=6.2 have been analysed.

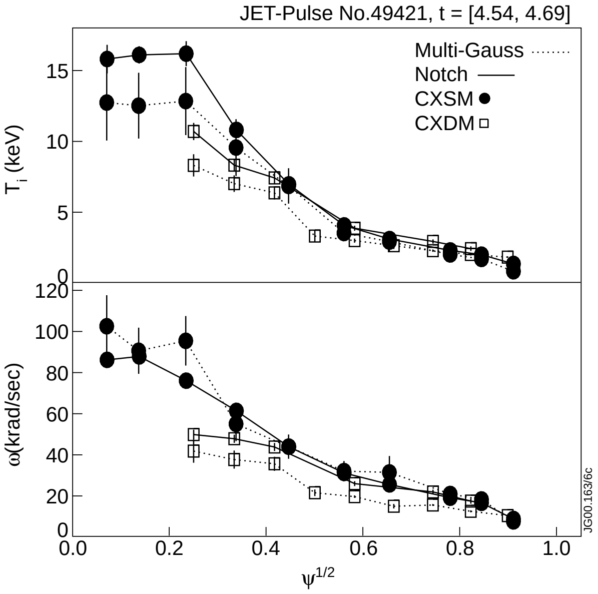

Fig.13.9: Ion temperature and toroidal rotation comparing the result from the Multi-Gauss fitting method with the notch method for the first notch in #49421. In this case, the Multi-Gauss method underestimates slightly the temperature for both instruments. All results are however very similar, probably because of the presence of Neon. This provides one more spectral line with the correct temperature information for the Multi-Gauss method, which means that the fit is better constrained.

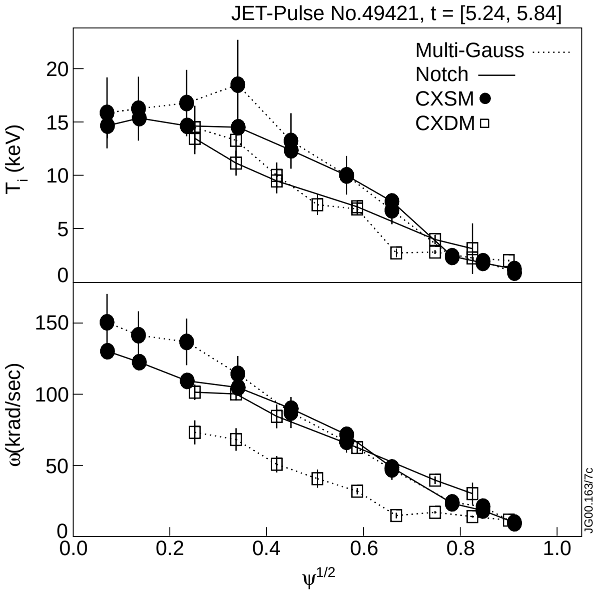

Fig.13.10: Results for the second notch in #49421. At this time, the Neon density is lower that during the first notch, and the benefit of the extra spectral line is no longer apparent.

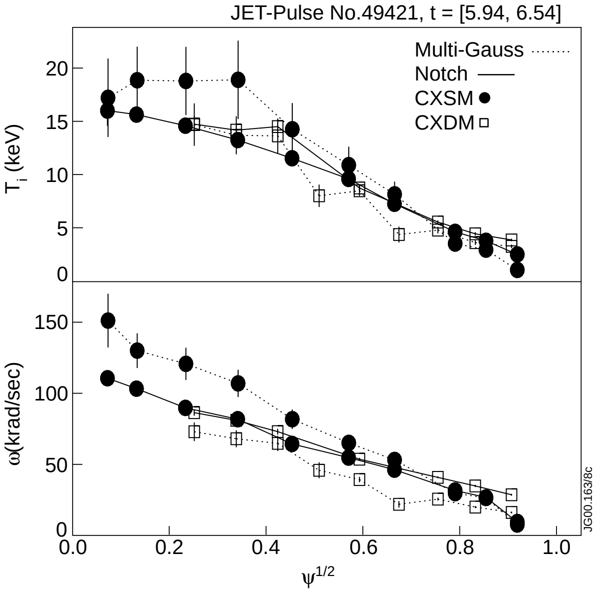

Fig.13.11: Results for the third notch in #49421.

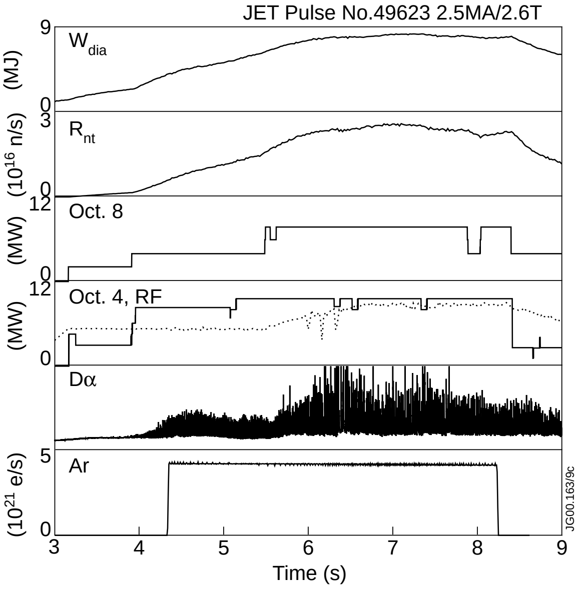

Fig.13.12: Time history of NBI waveform and its effect on the plasma for #49623. There is no compensation for total input power from Oct. 4.

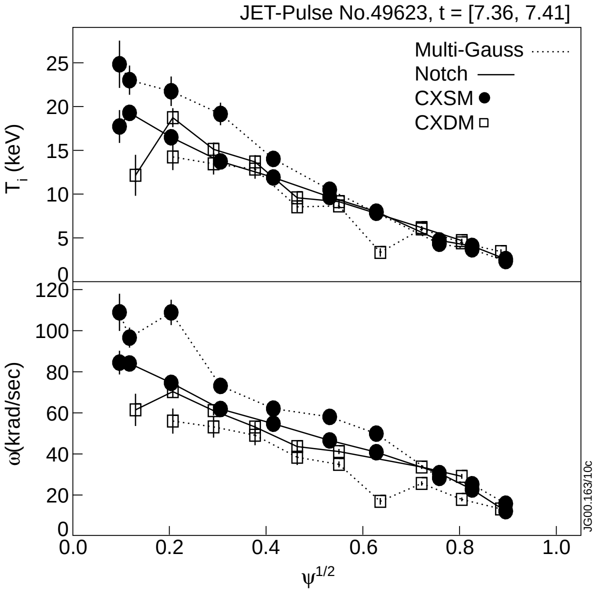

Fig.13.13: Ion temperature and toroidal rotation comparing the result from the Multi-Gauss fitting method with the notch method for #49623. No clear transport barrier is seen in any of the Ti results, though there is a clear transport barrier in the electron temperature with an outer footpoint at 3.68m extending into 3.48m (where it is probably limited by a tearing mode).

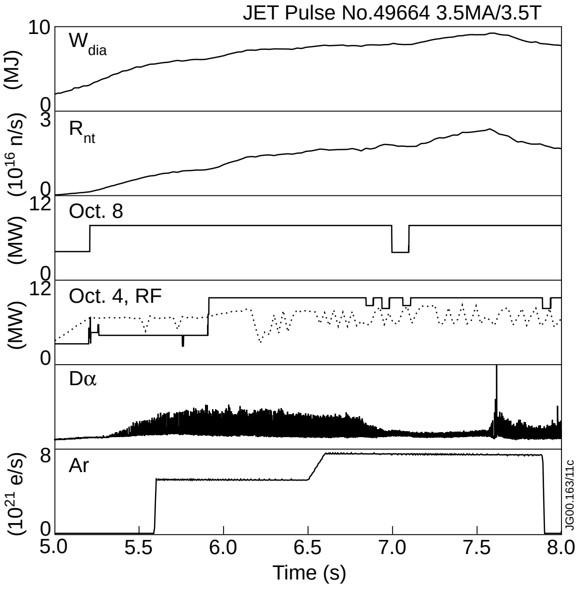

Fig.13.14: Time history of NBI waveform and its effect on the plasma for #49664. The effect of the edge control on performance begins to be noticeable first after the notch, and therefore the background spectra taken during the notch are not a good representation of what happens thereafter.

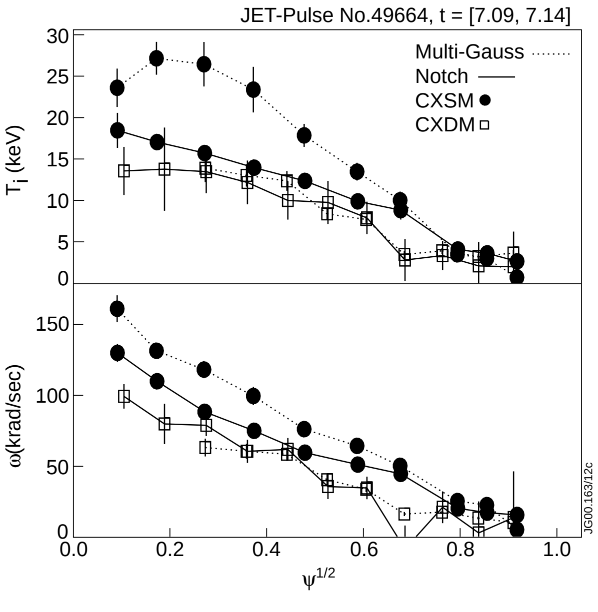

Fig.13.15: Ion temperature and toroidal rotation comparing the result from the Multi-Gauss fitting method with the notch method for #49664. The results of the notch method do not agree well either, both with respect to the location of the transport barrier and the actual central temperature.

13.3 Summary and future directions

For the time being, notched Oct. 8 neutral beam waveforms are the only technique by which we can obtain validated CXS data in the presence of Argon. It is somewhat disconcerting that the best results are obtained, if the Oct. 4 waveform compensates for the loss of power in Oct.8. This puts a severe restriction on the total available power, and is thus impractical.

We are proceeding to develop the analysis techniques based on descriptive analysis of the combined spectra. The NBI notch experiments described in this report, and any such experiments in the future, will provide a benchmark to validate this technique.

13.4 Shot List

Successful notch experiments have been performed for 49021, 40407 (two notches), 49421 (three notches), 49623 and 49664.

Acknowledgements

Getting the NBI set-up for notch experiments right is a difficult task for the neutral beam operators. We would like to thank T Jones, C Challis and D Young for their support during these experiments.

References

[13.1] K-D Zastrow *et al.* EPS 1999 Maastricht

14. MSE DATA CONSISTENCY AND RESULTS

N C Hawkes[1], B Stratton[2], B Alper[1], B Budny[2], C Challis[1], S Cortes[3], V Drozdov[1], K Guenther[1], T Hender[1], J Mailloux[1], R Prentice[1], D Testa[4], K-D Zastrow[1], W Zwingmann[5]

JET Joint Undertaking, Abingdon, Oxon, OX14 3EA, UK.
[1] Euratom/UKAEA Fusion Association, Culham Science Centre, Abingdon, OX14 3DB, UK
[2] Princeton Plasma Physics Laboratory, PO Box 451, Princeton, NJ 08543, USA
[3] Euratom/IST, Av. Rovisco Pais, Lisboa, Portugal
[4] Plasma Science and Fusion Center, Massachusetts Institute of Technology, Cambridge, USA
[5] Association Euratom-CEA, CEA-Cadarache, F-13108, St. Paul lez Durance, France

14.1 Overview

This section describes the results obtained from EFIT magnetic equilibrium reconstructions using magnetics and MSE data as constraints. The work involves the completion of the calibration of the diagnostic and consistency checks between MSE, polarimetry, magnetics, ECE and soft X-ray data, particularly in cases where local values of q are suggested by MHD observations. In the majority of cases there is good agreement between the q profiles obtained using MSE data and these other signatures, the exceptions are recorded in the report and suggest future avenues of work. The calibration has been successfully applied to the analysis of the 2.6 T timing scan data, to the high performance shot 47414 and shots from a wider range of Optimised Shear experiments. Inclusion of the radial electric field has been applied in a case with strong toroidal rotation with only a modest effect (<20%) on the derived q profile. While this appears to be a general result there are some instances where the plasma E_r can be significant. For one case the radial profile of E_r and the shearing rate from the MSE and charge exchange data have been derived, yielding a peak value of 5×10^5 s^{-1}. The scale length for the E_r shear is equal to or less than the 5 cm chord spacing of the MSE measurements.

14.2 Results

The calibration of the MSE diagnostic has two elements to it: the response of the instrument to different polarisation states of the input light and the definition of the zero angle of the input polarisation. The action of the optical elements in the instrument is described by a series of matrices (Mueller matricies) and the partially polarised input light by a four element Stokes vector. The response of the polarimeter itself can also be expressed as a matrix that operates on a Stokes vector to yield four voltage signals that comprise the polarimeter outputs. The calibration of the entire instrument response involves the evaluation of a number of parameters in the matrix coefficients, the optical train including the polarimeter can then be expressed as a single matrix. The interpretation of the polarimeter signals is then achieved by multiplying the output voltages by the inverse of this response matrix. The result of this analysis gives not only the angle of linear polarisation of the input light, but also the overall linear and circular polarised fractions.

This analysis is necessary since the Stark emission is observed to have a circular polarised component (due to the presence of crossed E and B fields) which must be distinguished. In principle, there should also be an advantage when the input light is only weakly polarised, as would occur at high plasma density (although this regime, only achieved with pellet injection, has not been studied in the present work). The instrument response was measured for all angles of linear polarised light in a laboratory set-up. The parameters in the response matrix were determined from a least squares fit to the measurements. With the instrument mounted on JET and operating at elevated temperature the parameters were modifed using features of the Stark emission spectrum.

As with all MSE diagnostics, the accuracy of the measurements is limited by the accuracy with which the zero angle of the instrument can be ascertained. Several techniques were investigated with the most reliable results obtained from firing a neutral injector into a gas-filled torus. These calibration shots were done during both the Spring and the Autumn campaigns of 1999. However, for the calibration shots of the Spring campaign the instrument was tuned for the sigma components of the Stark emission (to maximise intensity from the anticipated weak signals) while in the Autumn, since the signal strength was found to be adequate, shots were run with both sigma and pi tuning. Since pi tuning is used for the plasma measurements the calibration data taken in the Autumn are more directly applicable and, in fact, these measurements have been used without modification in the analysis of data from the Autumn campaign. The calibration data from the Spring campaign appear to need some modification in order to obtain a match between the q-profiles obtained and MHD signatures (2/1 modes at q=2 and sawteeth at q=1) encountered during the ITB timing scan. It is probable that the need for this modification arises from the use of sigma tuning in the calibration shots of the Spring and a change to the diagnostic response during work carried out in the intervening shutdown.

Shots Analysed

Over fifty shots have so far been analysed and these are listed in section 14.4 below. A public PPF has been established, EFTM (EFIT with MSE constraints), to allow for easier access to the analysed data. Most of the processed shots have been rewritten into this PPF, and in future the validated analysis results will be written to this location. The PPF is the standard EFIT one, but the EFIT runs include the MSE data as constraints. The PPF generally also contains Faraday rotation data (from the KG4 diagnostic) together with EFIT predictions for these measurements to allow comparisons to be made, although the EFIT analyses do not include these measurements as constraints.

The results of the timing scan analysis provide an interesting comparison with the results of the intershot and magnetics-only EFIT runs. The intershot EFIT runs are made with relatively rigid regularising constraints on the profiles of ff' and p' (where p is pressure and f the flux function related to poloidal current), yielding stable solutions in nearly all plasmas, but leading to a loss of accuracy in some conditions. When EFIT is run with the MSE measurements included the data provides strong constraints to the equilibrium without the need for further regularisation. This is illustrated in fig.14.1(b) where the intershot q_0 values are compared with those from the MSE constrained EFIT runs. In these discharges it is, in fact, possible to relax the regularising constraints even when using just magnetics data. When this is done (fig.14.1(a)), the q_0 values obtained are very close to those from the MSE constrained cases, except for the highest values of q_0 in the range 2.5-3.0. The variation in achieved neutron rate as a function of q_0 is discussed in section 8.

As discussed in the previous section, the calibration of the MSE measurements for the Spring campaign (when the timing scan data was taken) is based on beam into gas shots done later in the year. An apparent (small) change between these two campaigns requires that the diagnostic is calibrated separately for the Spring campaign. This has been done such that the q-profiles in the timing scan match observations of MHD features, in particular for a shot with core 2/1 MHD activity and for a shot which begins to sawtooth during the heating pulse.

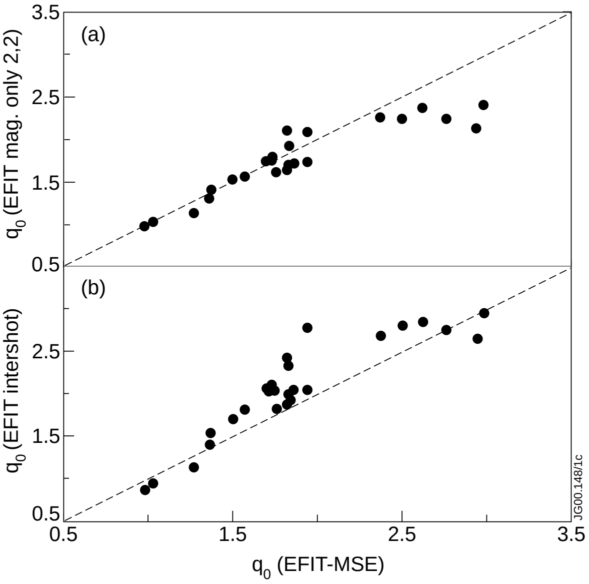

Fig.14.1: Results for q_0 obtained from EFIT constrained with MSE data compared to EFIT with magnetics only (second order polynomials for ff' and p') (a) and to EFIT 'intershot' (b), which has additional regularising constraints.

In general the equilibrium reconstructions examined in this work do not include pressure profile information in the constraints. Without this information the fitted pressure profile is rather sensitive to the accuracy of the MSE measurements. However, for two cases (47414 and 47620 the effect of including the TRANSP pressure profile as an extra constraint has been examined. With the pressure included the change to the equilibrium was small (~20%), confirming the validity of the MSE data. In general the pressure profile obtained from equilibrium reconstructions based on MSE data (without additional pressure profile constraints) is particularly sensitive to the location of the magnetic axis, which is determined by the zero-crossing of the MSE pitch angle profile.

Comparison Between MSE and Polarimetry

Where possible, the results of EFIT constrained by MSE data have been compared to other indicators of the equilibrium. MHD observations are the most direct indicators of features of the q-profile, and their radial location can often be determined with reference to ECE or soft X-ray measurements (see sections 2 and 4). The computed radial position of the plasma magnetic axis is sensitive to the MSE data and its position can be checked against ECE or soft X-ray measurements. In one case (below), the presence of energetic particle modes provides support for shear reversal, while the TAE spectrum yields information about the q-profile.

The results obtained from EFIT constrained by MSE measurements were compared with those from EFIT constrained by polarimetry for a specific test case (shot 49651, from a sequence of Optimised Shear LHCD pre-heated discharges). A summary of the results is shown in table 14.1, and corresponding q-profiles in fig.14.2. In this case there is good agreement between the two sets of q-profiles. The q-profiles do not change significantly depending on which diagnostics are include in the constraints; each set of measurements (MSE or polarimetry) constrains the reconstruction to give similar results. (There are no regularisation constraints in these tests.) Several other discharges have been analysed using either polarimetry or MSE measurements and the agreement seems to be a general result.

Table 14.1: Fitting errors (χ^2) against magnetics, MSE and polarimetry measurements with different polynomical orders for ff' and p', and different sets of constraints included in the equilibrium reconstructions (Shot 49651, 4.26s).

MAG+ MSE	MAG+ FAR	FF'	P'	χ^2_{MAG}	χ^2_{MSE}	χ^2_{FAR}	q_{min}	q_0
	✓	3	2	23		10.7	2.77	2.85
✓		3	2	25	12.1	12.6	2.75	2.95
✓	✓	3	2	26	12.3	12.0	2.79	2.99
	✓	4	3	22		9.1	2.45	3.45
✓		4	3	21	10.7	15.7	2.57	2.75
✓	✓	4	3	26	11.0	12.7	2.80	2.80

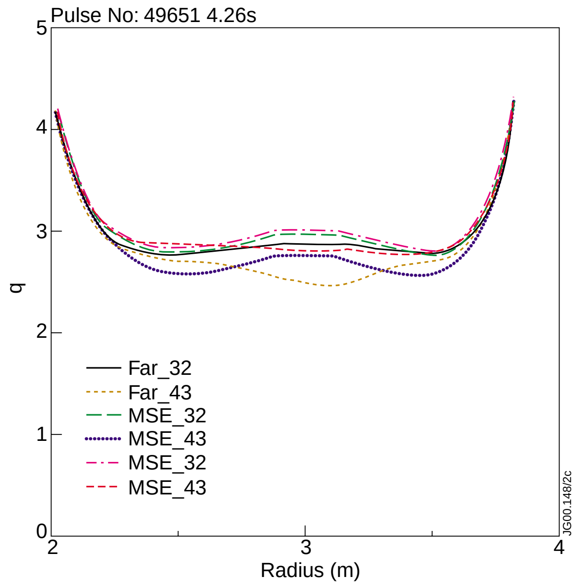

Fig.14.2: q-profiles obtained from EFIT when using different polynomical orders for ff' and p', and different sets of internal constraints (MSE or polarimetry, separately or combined).

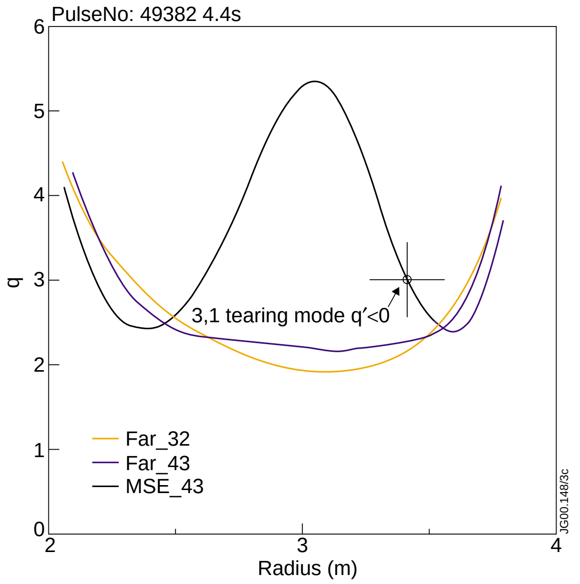

Fig.14.3: Different q-profiles are obtained from EFIT dependent on the internal constraints used. The MSE constraints yield a peaked q-profile with shear reversal while the polarimeter constraints give a monotonic q-profile (shot 49382, 4.4 s).

However, a particular discharge has been identified (49382, Optimised Shear with LH pre-heat) that shows large differences in the reconstructed q-profiles dependent on which diagnostic set is used in the constraints. The conficting q-profiles are shown in fig.14.3, where the MSE reconstructions indicate strong shear reversal in the plasma centre which is not seen in the polarimetry constrained equilibria.

Such strong shear reversal is atypical of JET, however, there is good evidence that such a q-profile is correct, at least in some important respects: An m/n=3/1 tearing mode has been identified, from correlation with ECE T_e profiles, this is located at R=3.35 m, while the phase of the correlation indicates that this is a region of reversed magnetic shear. The occurence of 'chirping' in the fast magnetics data (fig.14.4) is explained by the presence of energetic particle modes (EPMs) associated with reversed shear. This evidence is all consistent with the MSE data. Even taken on their own, the MHD observations would strongly constrain the admissable q-profiles. Analysis of the TAE spectrum is broadly consistent with the MSE data and these other observations but disagrees somewhat over the radius of the two q=3 surfaces.

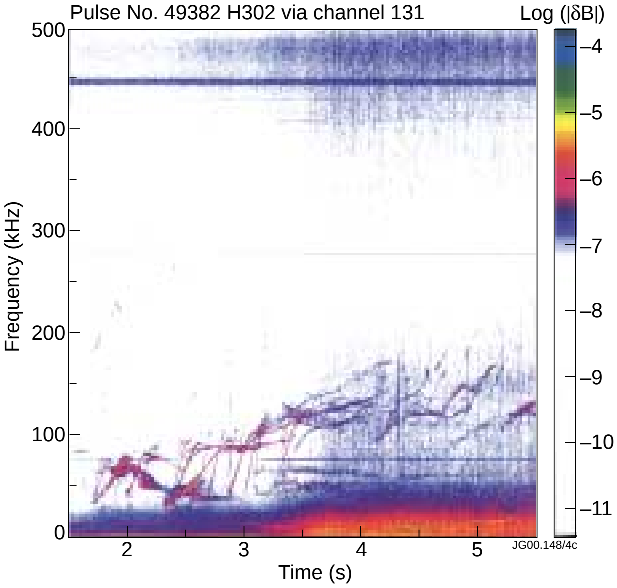

Fig.14.4: Spectrogram of magnetics fluctuation data. The presence of energetic particle modes that 'chirp' upwards in frequency is indicative of reversed magnetic shear. Assuming that these modes saturate at the TAE frequency, the inferred features of the q-profile are broadly consistent with the MSE results in figure 14.3.

In an attempt to find the reason for the difference between the MSE and the polarimetry results, in this case, a number of ideas have been explored but so far these do not offer an explanation: The density inversion used in the calculation of the polarimetry signals is consistent with LIDAR measurements and the equilibrium solution with the polarimetry constraints seems to be unique (ie the equilibrium obtained from MSE does not predict the correct polarimetry signals). While the reasons for this discrepency remain unresolved the results from future campaigns will be continuously monitored for similar occurences.

Plasma Electric Field Correction and Measurements

TRANSP calculations for shot 47414 (a high performance discharge without pini 7 from octant 4 which otherwise invalidates the MSE measurements) show that the plasma E_r, deduced from the radial force balance equation,

$$E_r = \frac{\nabla p}{neZ} - V_\vartheta B_\varphi + V_\varphi B_\vartheta,$$

is dominated by toroidal rotation, figure 14.5. For this discharge, the use of argon seeding and the failure of one spectrometer makes the charge exchange data on which the TRANSP calculation innacurate, however, this is unlikely to affect this general conclusion. There is no measurement of poloidal velocity on JET so this term in the force balance equation is obtained from a neoclassial calculation. (The contribution from this term is small (10-20%) compared to the toroidal velocity term so the accuracy of the calculated V_ϑ is not crucial to the E_r value.)

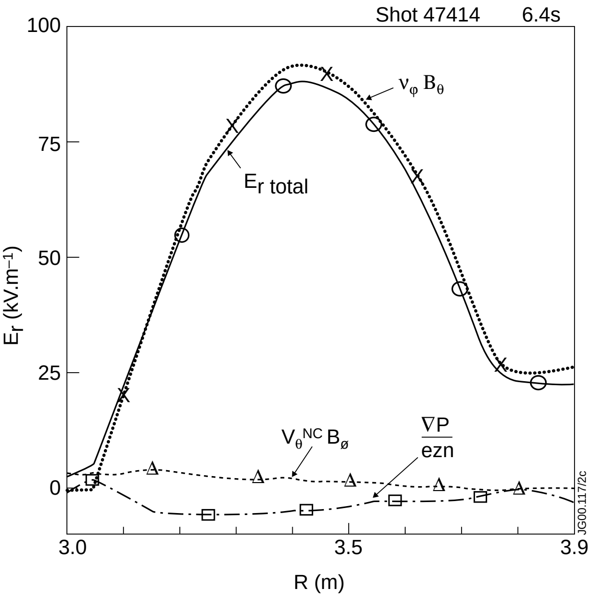

Fig.14.5: Components of plasma E_r as calculated using TRANSP with charge exchange data for T_i and V_φ. V_θ is assumed to be neoclassical. Toroidal rotation is seen to be the dominant term.

MSE measurements are affected by the plasma field [14.1] and can be calculated for a particular MSE geometry,

$$\Delta \tan\gamma_m = \frac{\cos\Omega}{v_b B_\varphi \sin\alpha} \Delta E_r .$$

When this effect is included in the analysis for this shot, the modification to the q-profile is modest (6% on axis and < 20% peak correction); the shots listed in section 14.4 are not corrected for the plasma E_r. Many of the q-profiles are evaluated at the start of the heating pulse when the injected torque is low and the plasma has not had sufficient time to reach a large rotation speed. In these cases the correction due to the plasma E_r is likely to be negligable.

There are, however, examples of shots where the radial electric field plays a significant role. Figure 14.6 shows the time evolution of MSE pitch angle measurements for a selection of radial channels for shot 47432. At 5.85 s, coincident with the barrier formation a change in gradient in the signal at 3.36 m is seen. This feature affects successive channels with increasing radius out to 3.55 m until the heating power is stepped down at 6.15 s, after which the feature (although less distinct) shrinks in radius. At times near the peak of the neutron rate a clear step is visible in the radial profile of MSE pitch angles, the appearance of the feature in the time plot is associated with the step crossing an individual channel.

The location and magnitude of the step in the pitch angles are an exact match to the step in the toroidal rotation profile measured with charge exchange, fig.14.7, both measurements corresponding to a change in E_r across the step, at 3.4 m, of 90 kV.m^{-1}.

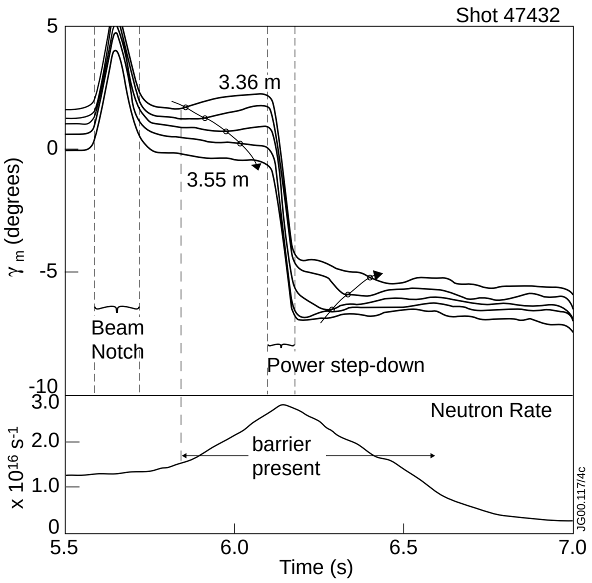

Fig.14.6: Time dependence of the MSE measured polarisation angles for a selection of channels showing the development of a perturbation in the angles that expands in radius as the transport barrier evolves, shot 47432. (The large transients at 5.6 s and 6.2 s are due to switching of different PINIs in the heating beams.)

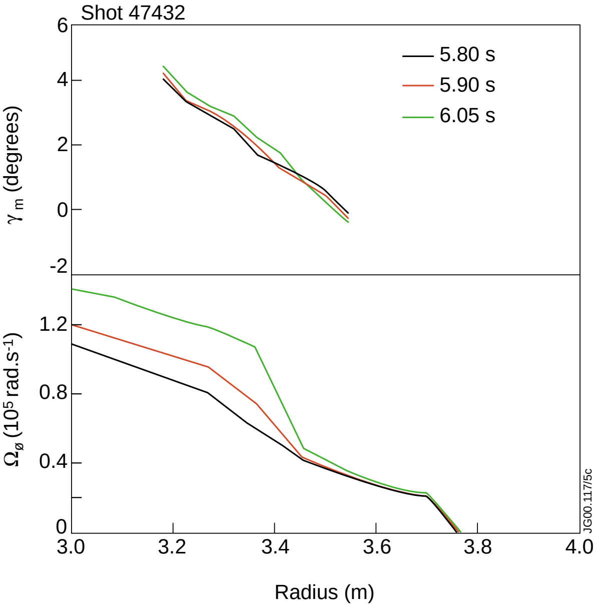

Fig.14.7: Radial profiles of MSE measured polarisation angles for three times during the discharge shown in fig.14.6. The step in the MSE angle profile coincides with the step in toroidal rotation measured with charge exchange. The magnitude of each step change is consistent with a change in radial electric field of 90 kV.m^{-1}

The effect of E_r on the MSE measurements cannot be directly compensated using the charge exchange data since the spatial grid of the charge exchange diagnostic is coarser than that of the MSE. The charge exchange measurements can, however, be used to compensate the MSE data for the plasma E_r wherever the radial profile is smoothly varying. This has been done (assuming that toroidal rotation is the only contributor to E_r) and then the results applied to EFIT, with channels near the step in E_r removed from the fit. The difference between the resulting zero-field predictions and the uncorrected MSE measurements (fig.14.8) yields the profile of plasma E_r. Away from the E_r step the profile is determined by the charge exchange data, near

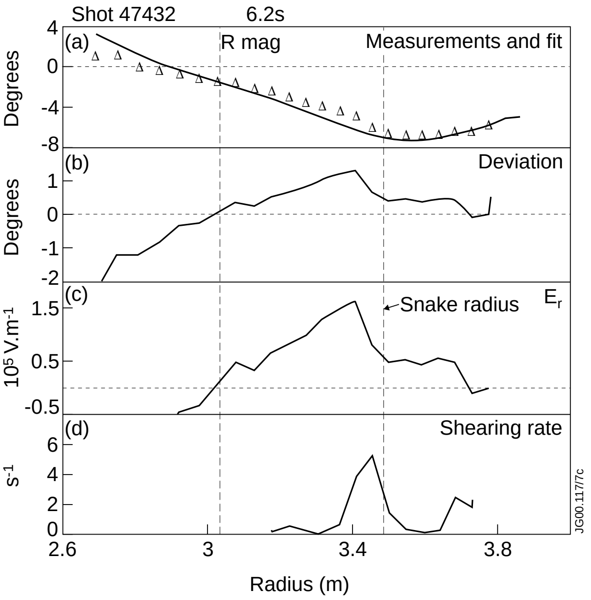

Fig.14.8: Calculations of the plasma E_r derived from MSE and charge exchange measurements. The coarser grid charge exchange data is first used to correct the MSE measurements, then the deviations from the resulting smooth profiles yield the details of the E_r profile near the step in the MSE angle at 3.5 m.

the step by the MSE data. This hybrid measurement gives a higher resolution measurement of the scale length for E_r and hence the $\mathbf{E}\times\mathbf{B}$shearing rate [14.2],

$$\omega_{\mathbf{E}\times\mathbf{B}} = \left| \frac{RB_\vartheta}{B} \frac{d}{dR} \left(\frac{E_r}{RB_\vartheta} \right) \right| .$$

While the measurements demonstrate that the scale length of velocity shear is smaller than the 10 cm chord separation of the charge exchange diagnostic, it is also possible that the scale length is smaller than the 5 cm chord spacing of the MSE measurements, since E_r changes within one channel width. Thus the shearing rates calculated are lower bounds for this parameter.

The discharge displayed a ‘snake’ instability at 6.3 s at 3.5 m. This location is just at the foot of the ion temperature barrier, and in the low E_r shear region at the foot of the E_r step. However, the q-profile calculated with MSE data shows q approaching 1.0 at the snake location, not q=2 as the mode numbers of the snake would indicate it should be. The reason for this discrepancy is not understood.

The data in fig.14.6 has been smoothed significantly in the time coordinate for the purposes of illustration, but examination of the unsmoothed data has yet to reveal evidence of a fast, large amplitude transient in E_r at the barrier formation, such as has been observed in TFTR [14.3].

14.3 Summary and future directions

The MSE diagnostic was built with the overriding aim of understanding the relationship between the q-profile and the occurrence of an internal transport barrier. Much has been learned so far from the MSE measurements but further measurements and analyses are necessary to elucidate this relationship. Recent measurements have been hampered by the clouding of the optics of the diagnostic, these have now been replaced and we anticipate better quality data in the future. The ultimate accuracy will be limited by the accuracy with which the zero point of the measurements can be obtained. So far, firing neutral beams into a gas filled torus has proved the best method of calibration this parameter. However, attempts have been made in the past to use other techniques, but the interpretation of the measurements has proved challenging. Advances in our understanding of the response of the diagnostic may mean that we are able to revisit these other techniques, with the prospect of obtaining more reliable measurements of the zero point.

The importance of the plasma radial electric field is twofold. In the first instance it is a nuisance parameter for the measurement of the q-profile with MSE data and must be measured in order to correctly interpret the pitch angle information. On the other hand, the role of E_r shear in turbulence stabilisation makes it a highly relevant parameter to measure in its own right. The two techniques most applicable to JET for the measurement of E_r are using the radial force balance for carbon where the components of the equation are measured using charge exchange spectroscopy (but there are severe difficulties with the measurement of poloidal velocity) and measurement using the MSE technique. The most sensitive way of obtaining Er from MSE measurements is to construct a new diagnostic viewing a new neutral heating beam that injects in the opposed toroidal sense to the existing beams.

The analysis of discharges, such as the one discussed in this report, where strong E_r shear develops is a clear area for further interesting study. The time evolution of E_r from the MSE and charge exchange measurements is of topical interest, in particular to compare the shearing rates obtained with the instability growth rates [14.4]. A critical comparison with discharges that develop a transport barrier without such strong E_r shear is indicated.

Finally, there are modifications required to the MSE diagnostic, neutral beam parameters and analysis techniques to try to improve the measurements, in particular the discrimination against, and interpretation of, signals from different PINIS in the injector.

14.4 Shot List

Table 14.2: List of shots analysed for magnetic equilibrium using EFIT with MSE constraints. A tick in the final column indicates that the data has been rewritten to the public PPF, EFTM. (Some shots have yet to be reprocessed, these are marked with a circle.) There are still some requests for analysis still outstanding.

Pulse	Description	Comment	EFTM
47432	Snake		✓
47606	Timing scan		✓
47609	Timing scan		✓
47611	Timing scan		✓
47614	Timing scan		✓
47615	Timing scan		✓
47620	Timing scan		✓
47621	Timing scan		✓
47622	Timing scan		✓
47630	Timing scan	See JETBST/EFIT ppf, seq 16	•
47636	Timing scan		✓
47637	Timing scan		✓
47638	Timing scan	See JETBST/EFIT ppf, seq 15	•
47639	Timing scan		✓
47640	Timing scan		✓
47643	Timing scan		✓
47644	Timing scan		✓
47645	Timing scan		✓
47646	Timing scan		✓
47648	Timing scan		✓
47649	Timing scan		✓
47650	Timing scan		✓
47651	Timing scan		✓
47653	Timing scan		✓
47660	Timing scan		✓

Pulse	Description	Comment	EFTM
47863	Timing scan		✓
47865	Timing scan		✓
47866	Timing scan		✓
47867	Timing scan		✓
47868	Timing scan	See JETBST/EFIT ppf, seq 11	•
47869	Timing scan		✓
49197	ICRH/NBI in ITBs		
49263	RI Mode	OK	✓
49264	RI Mode	OK	✓
49265	RI Mode	No Octant 4 pini 1; can not analyse	✗
49270	RI Mode	OK	✓
49272	RI Mode	OK	✓
49275	RI Mode	No Octant 4 pini 1; can not analyse	✗
49320	RI Mode	No good times due to large scatter in data	✗
49323	RI Mode	No good times due to large scatter in data	✗
49382	LHCD ITBs	Shear reversal, MHD, TAE confirmation. Disagreement with polarimetry	✓
49377	LHCD ITBs	Shear reversal with MHD confirmation of q-profile, as 49382.	✓
49384	LHCD ITBs		•
49630	LHCD ITBs		•
49647	LHCD ITBs		•
49651	LHCD ITBs	Flat q, agreement between MSE and polarimetry	✓
49654	ICRHNBI in ITBs	Cannot analyse: pini 1 voltage incompatible (shot 49644 used instead)	
49644	ICRH/NBI in ITBs	Comparison with 49651 (instead of 49654)	•
49680	LHCD ITBs		•
49682	LHCD ITBs		•
49683	LHCD ITBs		•
49783	High beta p		✓
49793	High beta p		✓
49794	High beta p		✓
49798	High beta p		✓
49291	NTMs		✓
49292	NTMs		✓
49293	NTMs		✓
49294	NTMs		✓

• *EFTM ppf still needs to be written for these shots*

Acknowledgements

The authors wish to acknowledge helpful discussions with D Mazon.

References

[14.1] M. C. Zarnstorff et al, Physics of Plasmas, **4** (1997) p1097

[14.2] D. R. Ernst et al, Physics of Plasmas, **7** (2000) p615

[14.3] R. Bell, et al, Plasma Physics and Controlled Fusion **40** (1998) p609

[14.4] F. Crisanti, European Physical Society, Conference on Plasma Physics, Budapest, 2000